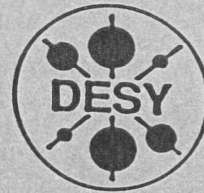


C
DEUTSCHES ELEKTRONEN-SYNCHROTRON



DESY-THESIS-1998-010

May 1998

hart auslegen

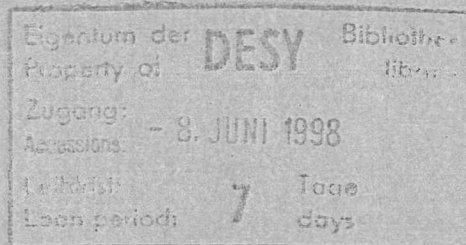


X1998-00861

Studying Characteristics of
Diffractive Deep Inelastic Scattering
with the ZEUS Leading Proton Spectrometer

by

J. T. Rahn



ISSN 1435-8085

NOTKESTRASSE 85 - 22603 HAMBURG

DESY behält sich alle Rechte für den Fall der Schutzrechtserteilung und für die wirtschaftliche Verwertung der in diesem Bericht enthaltenen Informationen vor.

DESY reserves all rights for commercial use of information included in this report, especially in case of filing application for or grant of patents.

To be sure that your reports and preprints are promptly included in the
HEP literature database
send them to (if possible by air mail):

DESY
Zentralbibliothek
Notkestraße 85
22603 Hamburg
Germany

DESY
Bibliothek
Platanenallee 6
15738 Zeuthen
Germany

UNIVERSITY of CALIFORNIA
SANTA CRUZ

**STUDYING CHARACTERISTICS OF DIFFRACTIVE
DEEP INELASTIC SCATTERING
WITH THE ZEUS LEADING PROTON SPECTROMETER**

A dissertation submitted in partial satisfaction of the
requirements for the degree of

DOCTOR OF PHILOSOPHY

in

PHYSICS

by

Jeffrey T. Rahn ✓

December 1997

The dissertation of Jeffrey T. Rahn is approved:

Professor Abraham Seiden, Chair

Professor Hartmut F.-W. Sadrozinski

Professor Howard E. Haber

Dean of Graduate Studies

Abstract

Studying Characteristics of Diffractive Deep Inelastic Scattering with the ZEUS Leading Proton Spectrometer

by

Jeffrey T. Rahn

The observation of diffraction in Deep Inelastic Scattering (DIS) at the HERA electron-proton collider generated considerable excitement. This reaction provides an opportunity to study at a parton level the mechanism responsible for diffractive and elastic reactions in hadronic collisions. The ZEUS experiment, equipped with a Leading Proton Spectrometer (LPS), is ideally suited to observe this reaction ($ep \rightarrow epX$) by detecting the proton p in addition to the electron e and photon fragment X . The reaction is approximately exponential in the momentum transfer squared t with an exponential slope $b = 6.6 \pm 0.6^{+1.2}_{-0.6}$ GeV². The inclusive cross section, expressed as $F_2^{D(4)}$, has been measured in the kinematic region $5 < Q^2 < 20$ GeV² and $x_F < 0.03$. An analysis of this structure function indicates that the soft Pomeron trajectory is most appropriate, although shrinkage has not yet been confirmed. The x_F dependence is observed to follow a power behavior $F_2^{D(4)} \propto x_F^a$ at $t = -0.16$ GeV², with a fitted to $1.08 \pm .06^{+0.08}_{-0.19}$. The inclusive event shape variables demonstrate a final state similar to the hadronic system produced in e^+e^- collisions at similar energy scales. These conclusions are discussed in the context of other analyses of the same reaction at HERA, with further discussion of the problems of background and event selection faced by measurements not based on the observation of the final proton.

Contents

List of Figures	vii
List of Tables	x
Dedication	xi
Acknowledgements	xii
1 Introduction	1
2 Theoretical Advances in Diffractive Deep Inelastic Scattering	3
2.1 Quantum Chromodynamics	3
2.1.1 Fragmentation	5
2.2 Deep inelastic scattering	6
2.2.1 Kinematic variables	6
2.2.2 Parton model	7
2.2.3 DGLAP evolution	9
2.3 Regge phenomenology	12
2.3.1 Application to diffractive dissociation	15
2.4 Diffractive DIS models	17
2.4.1 Kinematics	17
2.4.2 BFKL Pomeron: Nikolaev-Zakharov	18
2.4.3 Factorizable models	20
2.4.4 Partonic models of diffraction	21
2.5 Reggeon exchange in DIS: non-Pomeron exchange	21
2.6 Summary	22
3 HERA and ZEUS	23
3.1 HERA electron-proton collider	23
3.2 Overview of ZEUS detector	24
3.3 Central Tracking Detector	25
3.4 Uranium Calorimeter	25
3.5 Small Angle Rear Tracking Detector (SRTD)	27
3.6 Luminosity Monitor	28
3.7 ZEUS trigger system	28
3.8 Offline analysis	30

3.9	Systematic and statistical errors	30
4	LPS Hardware and Reconstruction	31
4.1	LPS detector	31
4.1.1	Silicon detectors and binary readout	31
4.1.2	Detector electronics	34
4.1.3	Mechanics for detector positioning	42
4.2	Operating conditions	43
4.2.1	Spectrometer components	43
4.2.2	Operation of Roman pots	43
4.2.3	Calibration and performance	46
4.3	Reconstruction software	47
4.3.1	Coordinate reconstruction	47
4.3.2	Pattern recognition	48
4.3.3	Track fitting	50
4.3.4	Track arbitration	51
4.3.5	Reconstruction software for alignment	52
4.4	Alignment	52
4.4.1	LPS configurations	52
4.4.2	Data samples	54
4.4.3	Alignment of isolated pots	54
4.4.4	Relative alignment of double-pot stations	55
4.4.5	Relative alignment of S4-S6 telescope	57
4.4.6	Location of S4-S6 telescope in ZEUS coordinate system	58
4.4.7	Location of S1-S2 telescope	60
4.4.8	Location of beam	61
4.4.9	Determination of beam apertures	66
4.5	Summary	66
5	Monte Carlo Simulation	71
5.1	ZEUS Monte Carlo system	72
5.2	LPS GEANT implementation	72
5.2.1	IHERA apertures	72
5.2.2	Magnetic field	73
5.2.3	Digitization	74
5.2.4	Beam simulation	74
5.2.5	LPS resolution with moving detectors	75
5.2.6	Accounting for changes in run conditions	75
5.3	Monte Carlo event generators	77
5.3.1	RAPGAP single diffractive DIS	78
5.3.2	NIKZAK single diffractive DIS	79
5.3.3	DIS ρ^0 diffractive	80
5.3.4	EPSOFT double diffractive DIS	80
5.3.5	π^0 Exchange	80
5.3.6	Beam halo simulation	80
5.4	Comparison of data with Monte Carlo	82

5.5	Simulating 1995 data	87
6	Kinematic Reconstruction	90
6.1	Identification of scattered electron	90
6.2	Calorimeter-track matching and noise suppression	90
6.3	Reconstruction of DIS kinematical variables	92
6.3.1	Jacquet-Blondel method	92
6.3.2	Electron method	93
6.3.3	Double-Angle method	93
6.3.4	Σ method	93
6.4	Reconstruction of diffractive variables	94
6.5	Event selection	96
7	General Properties of DIS Events with LPS Tracks	98
7.1	LPS selection of diffractive events	98
7.2	x_L distribution	98
7.3	$\Delta\phi$ distribution	99
7.4	t Distributions	101
7.4.1	t integrated over all variables	101
7.4.2	Systematic Checks	102
7.4.3	t in bins of physics variables	105
7.5	Non-diffractive M_X distribution	107
8	$F_2^{D(4)}$ Analysis	110
8.1	Unfolding	110
8.2	Bin choice	110
8.3	Results	111
8.4	Analysis of $F_2^{D(4)}$	115
8.4.1	Determination of α_P	115
8.5	Analyzing β dependence of $F_2^{D(4)}$	118
8.6	Analysis of Reggeon Contribution	120
9	Event Shapes	122
9.1	Observed distributions	124
9.2	Fragmentation Monte Carlo	127
9.3	Corrections	130
9.4	Discussion of ZEUS rapidity-gap results	136
9.5	Comparison with other experiments	137
10	Conclusions	139
	Bibliography	141

List of Figures

1.1	Elements of the standard model of particle physics	2
2.1	Feynman diagrams for $e^+e^- \rightarrow \mu^+\mu^-$	4
2.2	Example of fragmentation process	5
2.3	Definition of DIS variables	7
2.4	Demonstration of structure functions	8
2.5	Measurements of the proton structure function F_2	11
2.6	Regge approximation for hadronic interactions	13
2.7	The ρ Regge trajectory	14
2.8	Total photoproduction and elastic ρ^0 cross sections	15
2.9	Diagram of double dissociation	16
2.10	Feynman diagram of a diffractive event	17
2.11	Feynman Diagrams for Nikolaev-Zakharov approach to diffractive DIS	19
3.1	The ZEUS detector, yz view	25
3.2	The ZEUS detector, xy view	26
3.3	The ZEUS calorimeter	27
3.4	SRTD Geometry	28
3.5	ZEUS Trigger	29
4.1	LPS detector configuration	32
4.2	Conceptual diagram of silicon detector operation	33
4.3	Calibrating the binary readout system	34
4.4	Schematic of LPS front-end system	35
4.5	Simplified TEK-Z schematic	36
4.6	Determination of TEK-Z calibration capacitors	36
4.7	Yield for first set of TEK-Z chips tested	37
4.8	TEK-Z gain and noise values	37
4.9	DTSC simplified schematic	38
4.10	Layout of LPS hybrid	39
4.11	Demonstration of correlation of detector noise with detector capacitance	40
4.12	Schematic of LPS readout chain	41
4.13	Example of Roman pot insertion	42
4.14	Schematic diagram of HERA optics in the LPS region	45
4.15	Efficiency for LPS planes	47
4.16	Correlations used for pattern recognition	50

4.17	Resolution of 2-pot station alignment	56
4.18	Resolution of S4-S6 telescope relative alignment	58
4.19	Demonstration of quadrupole alignment procedure	59
4.20	Vertex distribution vs. x_L	61
4.21	Extrapolation of tracks to coordinates at S1	61
4.22	Average vertex as a function of the run number	63
4.23	Beam Tilt as a function of the run number	64
4.24	Plots of resolution variables from ρ^0 sample	65
4.25	Position of kinematic peak versus run number	65
4.26	Beam pipe aperture determination	67
4.27	x_L distribution for DIS events	70
5.1	Hand S4 in GEANT	73
5.2	Correcting run-to-run changes by applying weights	76
5.3	Weights applied to account for run-to-run changes	77
5.4	Generated quantities in RAPGAP	79
5.5	x_L distribution for events with $\eta_{\max} < 1.5$	80
5.6	x_L and t distribution for beam halo events	81
5.7	Comparison of DIS variables with simulation, 1994	84
5.8	Comparison of LPS variables with simulation, 1994	85
5.9	Comparison of physics variables with simulation, 1994	86
5.10	Comparison of detector variables with simulation, 1994+1995 data	88
5.11	Comparison of physics variables with simulation, 1994+1995 data	89
6.1	Correlation of tracking and calorimeter energies	91
6.2	Calorimeter noise suppressed by noise cuts	92
6.3	Resolution of reconstructed variables	95
7.1	Regions of the $x_L - \eta_{\max}$ plane	99
7.2	Fraction of events with a rapidity gap as a function of x_L	100
7.3	$\Delta\phi$ distribution for two sets of diffractive events	101
7.4	Inclusive $d\sigma/dt$ determination	102
7.5	Systematic checks on t distribution	103
7.6	Fits to t distribution in bins of physics variables	106
7.7	Fit to determine the non-diffractive $E + p_x$ distribution	109
8.1	Bin boundaries in x_T and β	111
8.2	Structure function results	112
8.3	x_T dependence of structure function as a function of β	116
8.4	Systematic checks on x_T slope	117
8.5	Plot of extrapolation $F_2^{D(4)}$ to $x_T = 0.001$	119
8.6	$F_2^{D(4)}$, fit with Reggeon contribution	121
9.1	Values of event shape parameters for simple particle distributions.	124
9.2	Boost to $\gamma^* - IP$ c.m. frame	125
9.3	Correlation of thrust with M_X	126
9.4	Test for correlations between thrust and other physics variables	128

9.5 Resolution of event shape variable reconstruction 129

9.6 Comparison of measured event shape variables with Monte Carlo models . . 131

9.7 Comparison of generated event shape variables 132

9.8 Systematic checks on event shape variables 135

9.9 Corrected thrust distributions, comparison with other ZEUS results 136

9.10 Corrected thrust distributions, comparison with e^+e^- data 138

10.1 Comparison of a measurements at different experiments 140

List of Tables

3.1 HERA design parameters and performance in 1994-95 24

4.1 Elements defining beamline in LPS area 44

4.2 Quality codes for LPS coordinates 48

4.3 Condition periods for 1994-1995 runs 53

4.4 Nominal parameters for geometry of LPS hands 55

4.5 Mechanical stability of S4-S6 57

4.6 Results of quadrupole fits 60

4.7 Covariance matrix for quadrupole fits 60

4.8 Resolution of LPS physics variables near $x_L = 1$, using ρ^0 sample 64

4.9 Steps to align planes within detector packets 68

4.10 Steps to locate pots 69

5.1 Test of agreement of data and Monte Carlo 82

7.1 $d\sigma/dt$ results 103

7.2 t in bins of physics variables 105

8.1 $F_2^{D(4)}$ Results 113

8.2 Methods of obtaining x_T dependence 117

8.3 β dependence of structure function 118

9.1 χ^2 comparison of event shape variables to models 130

9.2 Results of event shape variable analysis 134

List of Figures

Dedicated to my parents

Introduction

Chapter 1

Acknowledgements

Loving thanks go to the many family members and friends who have helped to guide my education and support my efforts in physics. In particular, my parents have done me a tremendous service by supporting my education and fostering my scientific curiosity. Completing this thesis would also have been impossible without the support of my wife Kelli. Additionally, the support of my brothers Chris, Mike, and Andy have been invaluable in encouraging my education. My education has also been supported by my grandparents Francis Rahn, Albert de Neufville, and Naomi Boyer, and I also appreciate the support from Otto and Hugo de Neufville.

While working at DESY, many wonderful people in the LPS group were supported my research, including Roberto Sacchi, Laura Iannotti, Amedeo Staiano, Michele Arneodo, Ada Solano, Tom Massam, and Marco Costa. Other people from DESY to whom I owe many thanks include Monika Grothe, Elisabetta Gallo, Gennady Briskin, Arnulf Quadt, Henri Kowalski, and Günther Wolf.

The University of California at Santa Cruz runs a phenomenal Particle Physics program, and this analysis would not have been possible without the computer code, education, and insight from Emanuela Barberis, Nicolo Cartiglia, Tim Dubbs, David C. Williams, Mark van Hook, Riko Wichmann, Abe Seiden, Hartmut Sadrozinski, Howard Haber and Michael Dine. While developing LPS hardware in the laboratory at SCIPP, it was my honor to work with a highly talented group of people, including Alex Grillo, Bill Lockman, Bill Rowe, Alec Webster, Max Wilder, Ned Spencer, Brad Hubbard, Georgia Hamel, Nora Rogers, and Arianne Frey. This is thesis version number 2.275, last updated October 18, 1997.

Chapter 1

Introduction

Modern high-energy physics attempts to determine the basic building blocks and interactions of matter. The current theory used to describe phenomena at high energies has been named the *standard model*. This model has had astounding success in describing a variety of features of high-energy reactions. At the core of the standard model are twelve fundamental particles, shown in figure 1.1. The standard model's success stems from the identification of the basic building blocks of matter as twelve *fermions* (the name fermion indicates that the particles carry half-integer spin), shown on the left side of this diagram. Forces in the model are also carried by particles, shown on the right side of this diagram, and called *bosons* because they carry integer spin. The twelve fermions are grouped into six *quarks* and six *leptons*, each of which has an antiparticle; the quarks are the top six particles shown in figure 1.1. The classical theory of electrodynamics has been *quantized* — written in terms of exchange of particles — to make Quantum Electrodynamics (QED), with the *photon* (or γ) responsible for carrying the electrical force. The weak force is carried by the W and Z bosons; the weak interaction can be observed in nuclear reactions such as β decay. The strong force is carried by *gluons* (g). Of the fermions shown in figure 1.1, all twelve interact with the weak force, the top nine interact electromagnetically, and the top two rows interact with the strong interaction. This thesis concentrates on the strong interaction between the light quarks (the up and down or u and d quarks).

It might be worthwhile to digress for a moment to define a high-energy reaction. Many physical processes, such as the sun or an atomic bomb detonation, certainly involve tremendous amounts of energy. However, the focus in high-energy physics is in placing a large amount of energy into a single particle. Macroscopically, this energy is fairly small, as each HIERA proton carries about 1 erg. Thus, the interactions between particles in high-energy physics are quite distinct from interactions within the sun, where particles carry at most a few MeV of energy. Reactions where the individual particles carry GeV energies ($\text{GeV} = 10^9 \text{ eV} = 1.6 \times 10^{-10} \text{ Joules} = .0016 \text{ erg}$) are actually quite rare, occurring in only a few conditions in the universe. These interactions would only be expected when temperatures exceed 10^{15} degrees. In fact, using temperature as an analogy for understanding high-energy physics interactions is fairly appropriate. A high-energy collision can be thought of as an investigation of processes found in very high temperature states.¹

¹Note that in high energy physics, no attempt is made to create a statistical ensemble, which normally is required when applying the concept of temperature

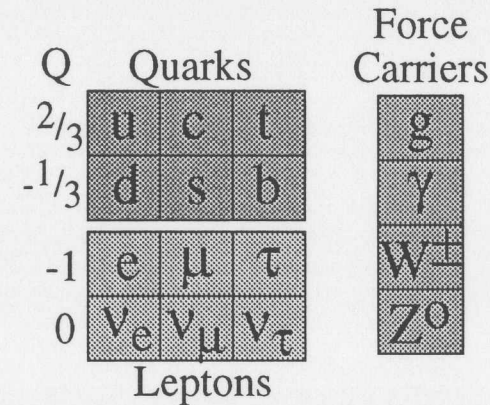


Figure 1.1: Fundamental particles of the standard model of particle physics.

Scattering experiments can trace their roots back to the α -particle experiments [1] which led to the hypothesis of the nuclear atom [2]. By observing the angular distribution at which α particles were scattered by matter, the existence of a dense central nucleus of the atom was proven. By the 1950s, the advantages of electrons instead of hadronic objects for probing matter were clear. The electromagnetic interaction could be predicted much more precisely than interactions involving hadronic objects, making electron-proton collisions a superior resource for study of the nucleus. Effectively, the electrons are used as a source of very high-energy (high-frequency) light, which allows analysis of small distance scales. In 1955, research at the High Energy Physics Laboratory at Stanford demonstrated that the proton was not pointlike, but instead had a "size" of approximately $0.7 \pm 0.2 \text{ fm}$ [3].

The next major advance in the study of the proton was the 1968 discovery of proton substructure, for which Jerome Friedman, Henry Kendall, and Richard Taylor were awarded the Nobel prize. The constituents of the proton were later identified as quarks [4].

This thesis reports on continuing effort in understanding the proton's structure and constituents by scattering electrons from these particles. In the second chapter, a discussion of the physics of deep inelastic scattering (DIS) will be presented, and the concept of diffractive scattering is introduced. The study is possible because of technical achievements of the HIERA collider and ZEUS detector, both described in chapter 3. Chapter 4 describes one component of ZEUS, the Leading Proton Spectrometer (LPS), which has been heavily used in this analysis. Chapter 5 describes the detailed simulation of ZEUS and the LPS, while event selection and reconstruction are described in chapter 6.

Physics analysis begins with general observations about the LPS data, including the longitudinal and transverse momentum distributions. Measurement of the cross section for diffraction is shown in chapter 8, followed by a discussion of the distribution of final state particles in chapter 9.

Chapter 2

Theoretical Advances in Diffractive Deep Inelastic Scattering

This chapter provides the motivation for the measurements made in this thesis. Quantum Chromodynamics provides the basic theoretical framework, and in particular the measurements of deep inelastic scattering have strongly supported this theory. However, diffraction has proven difficult to describe, but can be modeled using the phenomenological Regge theory. The models for diffractive DIS draw on a combination of Regge theory and DIS. In this chapter, these pieces are described, and an overview of the diffractive models are presented.

2.1 Quantum Chromodynamics

The interactions between hadrons has provided a rich set of experimental data, but these data have been difficult to interpret using one comprehensive theory. Examples of the hadronic properties which an ideal theory would describe include:

1. The masses of the proton and neutron
2. The stability, and decay channels of all isotopes of atoms
3. Masses of the observed meson and baryon resonances.
4. Interaction cross-sections between hadronic particles and both other hadrons and other constituents of the standard model
5. Final-state particle distributions in hadronic collisions

Because of the outstanding success of Quantum Electrodynamics (QED), the quantum field theory approach has been applied to other processes. Indeed, in weak and electroweak theories, the technique of quantizing a field theory led to advances in describing and understanding the physical phenomena. Moreover, QED is well approximated at low energies by nonrelativistic quantum mechanics, which in turn accurately predicts the ionization of the hydrogen atom (similar to objective 1, above) and ionization potentials for other atoms (similar to 3) along with a wide variety of other practical phenomena.

A quantized field theory has been developed to describe interactions involving hadrons, the *strong or hadronic* force [5, 6]. This theory, Quantum Chromodynamics (QCD), has successfully predicted many features of hadronic interactions. However, comparisons between data and theory have been difficult due to the nature of the strong interaction, at least as implemented in QCD. In order to understand this problem, a small amount of field theory is required.

Solutions to observable quantities in field theory are generally written as a series expansion of the number of particles involved in the interaction. For example, in the calculation of the cross section of $e^+e^- \rightarrow \mu^+\mu^-$, the first order term would involve the exchange of a single photon, as shown in figure 2.1. One of the higher-order terms would include one photon radiated from the final μ^+ . The contribution of diagrams with additional photons, however, is suppressed by a factor α_{em}^2 for each photon, where α_{em} indicates the strength with which the photons interact with the charged electrons and muons. The parameter α_{em} is not predicted but has been measured to be approximately 1/137 at low energies. Considering the interaction of the electron and muon as a series expansion, the contributions rapidly diminish. Only cases were 1 or a small number of photons need to be considered to obtain an accurate prediction, because α_{em} is so small.

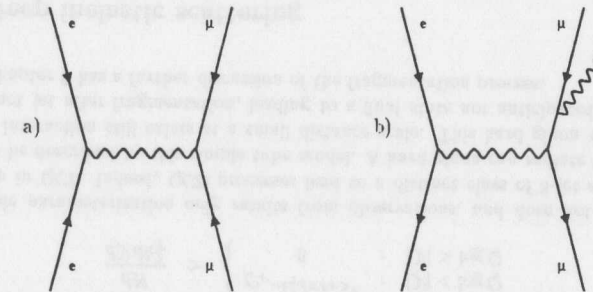


Figure 2.1: An example of $e^+e^- \rightarrow \mu^+\mu^-$: a) first order and b) one of the many second-order diagrams

The process for calculating observable rates in QCD is similar.¹ However, the strong interaction parameter α_S is much larger than QED's α_{em} — much larger than 1 at low energies. Each term in the series expansion exceeds the previous one and the expansion technique fails to give a meaningful answer.

Fortunately, QCD has a characteristic which has allowed some predictions to be made. The parameter α_S has energy dependence, decreasing as the energy of interaction increases. At an energy slightly below 1 GeV, $\alpha_S \simeq 1$, falling even lower at energies above $\simeq 1$ GeV. Thus, calculations of phenomena exclusively at high-energy can be performed with considerable accuracy. But even high-energy collisions of particles include some contributions of low-energy interactions (which cannot be calculated). Typically, the calculation of an observable quantity will include *soft* or *nonperturbative* parts and add an energy-

¹The non-abelian nature of QCD, or the ability of the gluon to interact with itself, leads to substantially more diagrams which must be calculated compared to QED.

dependent *hard* or *perturbative* QCD component. The evolution of the proton structure function, described in section 2.2.3, is a perfect example of this.

An additional difference between QED and QCD is that while QED has 2 charge states (+ and -), QCD has 3 distinct charge states. This characteristic led to the concept of *color*, with the three charges labeled red, green, and blue. A state with no charge in QED can be built by adding a positive and negative charge together. In QCD, three colors added together make a color-neutral state, white. Particles constructed from three quarks into a color-neutral state are called *baryons*. Additionally, anti-particles carry anti-color, so a colored particle plus an anti-particle can make a color-neutral state; particles built in this manner are called *mesons*.

2.1.1 Fragmentation

Large α_S values at low energies have been used to explain some characteristics of hadrons, especially *confinement* and *fragmentation* [7, 8]. Confinement refers to the fact that "free quarks" have never been observed - quarks always to come in pairs or sets of 3 [9]. For comparison, an electron and positron bound electromagnetically into positronium can be separated to an infinite distance with a few electron-volts of energy. There is no analogy for ionization with hadrons, however, because the strong interaction increases linearly with distance between the quarks, forcing quarks always to stay with an anti-quark or two other quarks of complimentary color, forming color-neutral states. These color neutral states can behave as independent particles since the strong interactions between color-neutral states vanishes at large distances.

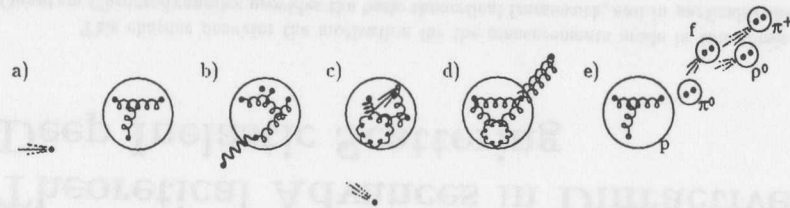


Figure 2.2: Example of fragmentation process in DIS.

Once the quark model began to gain acceptance, many scattering experiments involving hadrons intended to place enough energy into an individual quark that it would be able to escape the strong interactions with its neighbors and exist as a *free quark*. While that was never observed, the reaction which took place is the process of fragmentation, shown in figure 2.2. In this example, a high-energy (several GeV) electron approaches a proton (2.2a). One quark within the proton receives substantial momentum from the electron via the exchange of a photon (2.2b), and the electron and quark recoil from this exchange (2.2c). The electron, which carries no color charge, can exit without further interaction. For a short time, the quark also travels without interacting substantially with other particles in the proton. As the quark leaves the edge of the hadron, its energy is converted into a gluon field, slowing down the quark (2.2d). After sufficient energy is stored in the color string, the gluon field fluctuates into pairs of quarks, and these quarks combine

to make color-neutral objects, observed as free particles (2.2e). Essentially, the chain of gluons connecting the struck quark to the rest of the hadron condenses into a string of free hadrons: pions, ρ mesons, (for a list of known hadrons see [10]).

For the process $e^+e^- \rightarrow q\bar{q}$, the two quarks go through a nearly identical fragmentation process yielding a large number of final hadrons. Initially, the $q\bar{q}$ state exists as two quarks traveling in opposite directions. However, the gluon field forms between the two and breaks into $q\bar{q}$ pairs, fragmenting into hadrons.

The simplest model of fragmentation, the *tube* model [11, 12, 13, 14], uses two observed features of $e^+e^- \rightarrow q\bar{q}$ processes. First, the number of particles varies as the log of the invariant mass of the system. Second, the particles are distributed uniformly in rapidity space while transverse momentum (to the $q\bar{q}$ axis) appears to be exponentially suppressed:

$$\frac{dN}{dY dk_T^2} \simeq \begin{cases} C e^{-k_T^2 / \langle k_T^2 \rangle} & : |Y| < \log Q \\ 0 & : |Y| > \log Q \end{cases} \quad (2.1)$$

This simple parameterization only results from observations, and does not have a firm foundation in QCD. Indeed, QCD processes lead to a distinct class of 3-jet events, which would not be described by this simple tube model. A hard gluon can radiate from a quark while the interaction still exists at a small distance scale. This hard gluon would appear as a distinct jet after fragmentation, leading to a final state not anticipated by the tube model. Chapter 9 has a further discussion of the fragmentation process.

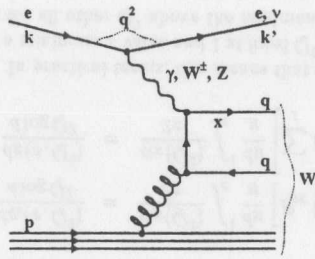
2.2 Deep inelastic scattering

Substantial progress has been made in understanding the physics of hadronic interactions by studying deep inelastic scattering (DIS). Using a lepton (electron, muon, or neutrino) as a source of photons, W^\pm or Z bosons, the quarks within the proton can be examined. One of the first breakthroughs in DIS was the discovery of substructure within the proton [15].

2.2.1 Kinematic variables

Consider the process $ep \rightarrow eX$. The 4-momentum of the particles is k for the initial and k' for the final electron, and p for the initial proton. s denotes the total center-of-mass energy. There are basically two degrees of freedom for the photon exchanged to the proton, which can be described by any two of the variables Q^2 , W , x or y , defined in figure 2.3. The invariant mass of the photon, Q^2 , sets the scale of the photon-quark interaction. The fraction of the electron's momentum carried by the exchanged photon is y . W refers to the invariant mass of the photon plus proton system, which sets the scale for the fragmentation process. x (or Bjorken- x) can be best described as the momentum fraction of the struck quark within the proton. Figure 2.3 includes the approximations valid for HERA, with masses of the particles set to 0 and x very small.

Since this process has 2 degrees of freedom at fixed s , a complete description can be obtained by measuring the differential cross section $\frac{d\sigma}{dx dQ^2}$. As the well-understood and easily calculable electroweak interaction is known to control this lepton-boson vertex, it is more convenient to isolate the photon, Z^0 or W contribution and calculate this cross section



$$\begin{aligned}
 s &= (k+p)^2 = 4E_e E_p \\
 Q^2 &= -q^2 = -(k-k')^2 \\
 W &= (k-k'+p)^2 \simeq ys \\
 x &= \frac{Q^2}{2p \cdot q} = \frac{Q^2}{sy} \\
 y &= \frac{p \cdot q}{p \cdot k}
 \end{aligned}$$

Figure 2.3: Variables used in DIS: The initial electron with 4-momentum k is incident on the proton with 4-momentum p . After exchange of a boson of momentum q , the final electron 4-momentum is k' .

in terms of the interaction of the lepton with another fermion. Thus, the cross section defines the *structure functions* F_2 , F_3 , and F_L . These structure functions are related to the differential cross section:

$$\begin{aligned}
 \frac{d\sigma(e^\pm p \rightarrow e^\pm X)}{dx dQ^2} &= \frac{4\pi\alpha_{em}^2}{xQ^4} \left[\left(1 - y + \frac{y^2}{2} \right) F_2(x, Q^2) - \frac{y^2}{2} F_L(x, Q^2) \right. \\
 &\quad \left. \mp \left(y - \frac{y^2}{2} \right) x F_3(x, Q^2) \right] \quad (2.2)
 \end{aligned}$$

The structure function has parity-conserving elements $F_2(x, Q^2)$ and $F_L(x, Q^2)$, along with the parity-violating $F_3(x, Q^2)$ which results from the weak interaction. Since the limited Q^2 reach of the measurements in this thesis preclude substantial weak contributions, F_3 will be ignored and only the photon exchange will be discussed here. Note that with weak effects ignored, the interaction is unchanged when positrons are substituted for electrons. For this reason, the term "electron" will be used to refer to either an electron or positron in this thesis.

The structure functions, as defined here, are only appropriate if gauge bosons interact with fermions within the proton. The constituents of the proton have been labeled "partons," with the fractionally-charged fermions identified as quarks bound by the neutrally-charged gluons. Since the gluons, where are bosons, do not carry any charge they do not interact electromagnetically or weakly, allowing the structure function to be written with only the consideration of lepton interactions with fermions. One of the key advantages of using leptons as a probe for proton structure is the ability to pick out only the charged constituents of the proton, in contrast with hadron-hadron collisions where quark-gluon, gluon-gluon, and quark-quark interactions all occur simultaneously. The parton model will describe how quarks, bound together by QCD, form the hadronic state of the proton.

2.2.2 Parton model

In the parton model, the proton (and other hadrons) consists of free spin-half quarks. At any given time there are a large number of quarks within the hadron, each

carrying a fraction of the total momentum x . The electromagnetic interaction between fermions has been studied for some time. The cross section for integral-charge fermions is:

$$\frac{d\sigma(\hat{s} = xs)}{dQ^2} = \frac{4\pi\alpha_{em}^2}{xQ^4} \left(1 - y + \frac{y^2}{2} \right) \quad (2.3)$$

The total electron-proton cross section is the sum over quark types i of this cross section, multiplied by the probability that quark type i (and charge e_i) is observed with momentum fraction x when probed with a photon of virtuality Q^2 :

$$\frac{d\sigma}{dx dQ^2} = \sum_i e_i^2 f_i(x, Q^2) \left(\frac{d\sigma_i(\hat{s} = xs)}{dQ^2} \right) \quad (2.4)$$

The only addition to the standard electromagnetic interaction between two fermions is the parton density $f_i(x, Q^2)$, which can be related to the structure function of equation 2.2:

$$F_2(x, Q^2) = \sum_i e_i^2 x f_i(x, Q^2); \quad F_L = 0 \quad (2.5)$$

The most basic version of the parton-model predicts that the longitudinal structure function is 0; and F_2 has no Q^2 dependence. In order to further explain the role of the structure function, four scenarios are described along with their corresponding structure functions.

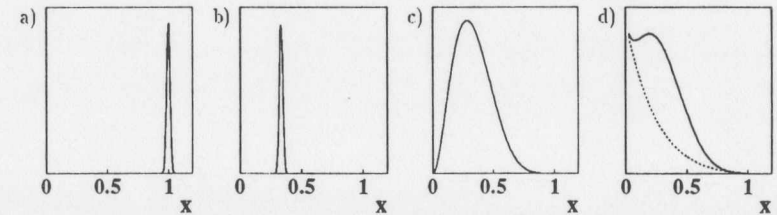


Figure 2.4: Possible structure functions for various simplistic proton models.

First, suppose that the proton were a pointlike fermion. Then the only possible x value would be 1, since every interaction would be with an object which carried all of the momentum of the proton. This would be observed as a parton density $f_i(x) \propto \delta(x-1)$ as shown in figure 2.4a.

Next, suppose that the proton consisted of 3 quarks, each of which carried exactly $\frac{1}{3}$ of the proton's momentum. Then the structure functions would be measured as $f_i(x) \propto \delta(x - \frac{1}{3})$ (figure 2.4b).

A more complex case arises when the quarks are in a bound state, as is the case within the proton. The relative motion of the quarks inside the proton smears the observed momentum fraction away from a δ function, into a broad distribution with an average value of $\frac{1}{3}$. These quarks are named *valence* quarks (figure 2.4c).

The quark-parton model is substantially improved with the addition of QCD effects. Since gluons can split into quarks, this provides a large supply of *sea* quarks at low- x . In

figure 2.4d, the sea contribution is shown with the dotted line, with the sum of valence plus sea quarks shown by the solid line. QCD effects can also cause F_L to be nonzero. Finally, QCD makes the structure functions dependent on Q^2 . This energy dependence can be predicted well with theory, as shown in the next section. As a consequence, the parton densities f_i in equation 2.5 are dependent on Q^2 ($f_i(x, Q^2)$).

Six quarks have been identified in the Standard Model (figure 1.1). Protons (neutrons) are considered bound states of 2 (1) *up* and 1 (2) *down* valence quarks. The *charm* and *top* quarks have the same charge ($+\frac{2}{3}$) as the up quark, but have larger masses of $\sim 1-1.5$ GeV and 180 GeV [16]. The *strange* and *bottom* quarks have the same charge as the down quark ($-\frac{1}{3}$) and have masses of 0.1-0.3 GeV and ~ 4 GeV, respectively. The strange, charm, bottom, and top quarks make up exotic meson and baryon states which can be created in the laboratory, but do not directly contribute to physics at lower energy scales, since they rapidly decay to the lower-mass up and down quark states.

2.2.3 DGLAP evolution

The Q^2 dependence of the structure functions provides one of the most stringent tests of QCD. Prediction of the structure functions themselves is impossible due to non-perturbative contributions. Their *evolution* in Q^2 , however, has a firm prediction because changes in the structure function as a function of Q^2 are predominantly the result of perturbative effects. Thus, from a measurement of $f_i(x, Q_0^2)$ over a range of x up to 1 allows prediction of $f_i(z, Q^2)$ at any $Q^2 > Q_0^2$ and $z > x$, using DGLAP evolution [17].

At larger Q^2 values, additional partons are expected due to "parton splitting," or radiation of partons from other partons. The parton *splitting function* has been defined to describe the rate at which partons are radiated from other partons. Four possible cases need to be considered: the probability of a quark splitting into a gluon $P_{qg}(z)$ or a quark $P_{qq}(z)$ ($P_{qq}(z) = P_{qq}(1-z)$); the probability of a gluon splitting into gluons, $P_{gg}(z)$, and the probability of a gluon splitting into quarks, $P_{gq}(z)$. All of these splitting functions can be solved using QCD as a function of the fraction of the momentum carried by the final parton z [18]. The evolution of the density functions, to leading order, is given by the equations:

$$\frac{dq_i(x, Q^2)}{d \log Q^2} = \frac{\alpha_S(Q^2)}{2\pi} \int_x^1 \frac{dy}{y} \left[P_{qq}\left(\frac{x}{y}\right) q_i(y, Q^2) + P_{qg}\left(\frac{x}{y}\right) g(y, Q^2) \right] \quad (2.6)$$

$$\frac{dg(x, Q^2)}{d \log Q^2} = \frac{\alpha_S(Q^2)}{2\pi} \int_x^1 \frac{dy}{y} \left[\sum_j P_{gq}\left(\frac{x}{y}\right) q_j(y, Q^2) + P_{gg}\left(\frac{x}{y}\right) g(y, Q^2) \right] \quad (2.7)$$

In practical terms, this means that once the structure function has been measured between a minimum x value and 1 at fixed Q^2 , DGLAP evolution would predict the structure function for all other Q^2 above the minimum x value.

The naive parton model does not predict any dependence of the parton density functions, or the structure function, on Q^2 . The failure of this approximation is known as "scaling violation" and can be seen clearly in HERA and fixed-target data [19, 20, 21] (figure 2.5). In this figure, the "soft" information could be considered the normalization of every line at different x values. The QCD prediction is only in the slope of these lines, and the agreement between the data and QCD evolution strongly supports QCD.

Since the parton densities are not predicted by the model, these can only be measured. Many parameterizations exist which describe the data well and include evolution effects [22, 23, 24].

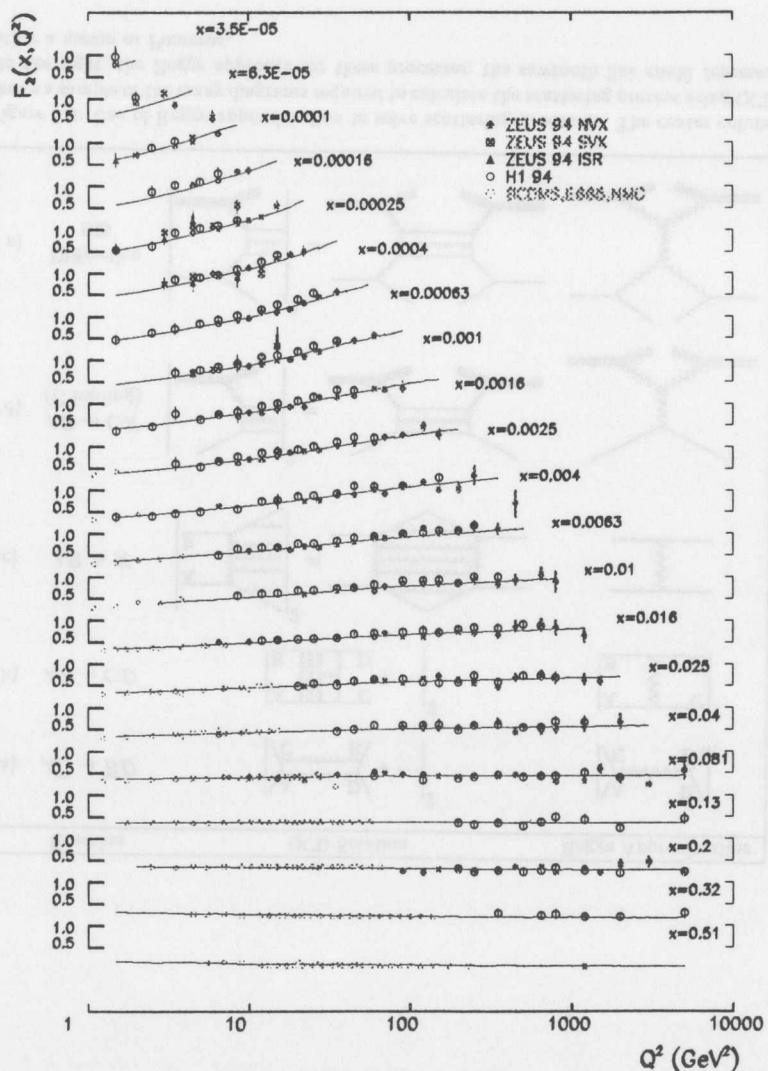


Figure 2.5: Measurements of the proton structure function F_2 as a function of Q^2 ; the line indicates a fit using DGLAP evolution.

2.3 Regge phenomenology

The previous sections have detailed some successes and shortcomings of QCD. The shortcomings — inability to make predictions involving “soft” effects — has led to a revival of Regge phenomenology. The original work of Regge [25] has been developed into a framework known as Regge theory [26]. The domain of Regge phenomenology includes predictions for the s (total energy squared) dependence of hadron-hadron scattering cross sections and predictions about leading particles in hadron-hadron collisions. However, Regge theory does not have any clear relation to QCD; the failure of QCD to describe soft processes makes phenomenological models such as Regge theory the only available option for describing many observations.

In order to understand how Regge theory is applied, consider the reaction in figure 2.6a, the process $A\bar{C} \rightarrow \bar{B}D$. For low center-of-mass energies \sqrt{s} ($\simeq 1$ GeV), this process is dominated by the production of resonances whose quantum numbers are appropriate for initial particles A and B . Such resonances have been carefully studied, and the masses, widths, and spin states measured [10]. A complete calculation of this reaction in QCD would sum Feynman diagrams such as that shown in the middle column of figure 2.6a. Of course, any attempt to perform the QCD calculation perturbatively would fail because of soft interactions involved in the reaction. Regge theory, on the other hand, would describe this reaction as mediated by resonances, for example the ρ resonance. In this case, the “coupling” between the initial particles and final particles, along with the propagator, are described as if the resonance were a fundamental particle in the field theory. One important attribute of these resonances, which is exploited in Regge theory, is their tendency to have linearly correlated spin J and mass squared. The ρ trajectory is shown in figure 2.7, with two on-shell particles. Other trajectories have more particles. The straight line correlation between $\alpha = J$ vs. $t = m^2$, is known as the Regge trajectory: $\alpha(t) = \alpha(0) + \alpha' \cdot t$. The presence of these resonances is equivalent to the series of poles in the scattering amplitude for the process $A\bar{C} \rightarrow \bar{B}D$ at integer values of the spin.

One success for Regge theory is the description of the crossed reaction $AB \rightarrow CD$, shown in figure 2.6b. In this case, the exchanged particle is no longer on-shell; the center-of-mass energy squared s , which described the mass of the exchanged object, is replaced by t (typically negative). The particle is off-shell and resonances cannot be observed. Aside from the change in kinematics, the actual Feynman diagrams which would describe this process are identical to s channel exchange. Regge theory can be applied for negative values of t as $s \rightarrow \infty$ to get the asymptotic behavior of the crossed channel process $AB \rightarrow CD$:

$$A(s, t) \stackrel{s \rightarrow \infty}{\sim} \beta(t) \cdot s^{\alpha(t)} \quad (2.8)$$

and the differential cross section

$$\frac{d\sigma}{dt} \propto \frac{1}{s^2} |A(s, t)|^2 \propto \beta^2(t) \cdot s^{2(\alpha(t)-1)} \quad (2.9)$$

where $\beta(t)$ depends on the type of the colliding particles. Figure 2.7 presents experimental data confirming this behavior of the scattering amplitude. The points in the $t < 0$ region correspond to $\alpha(t)$ extracted from the charge exchange reaction $\pi^- p \rightarrow \pi^0 n$. They align with the resonances belonging to the ρ trajectory — the intermediate states of the crossed channel process $\pi^- \pi^0 \rightarrow \bar{p}n$.

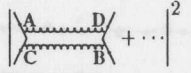
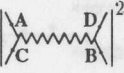
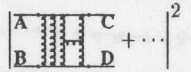
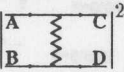
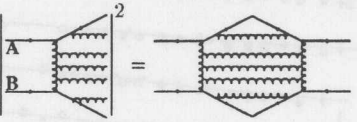
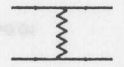
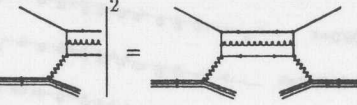
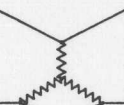
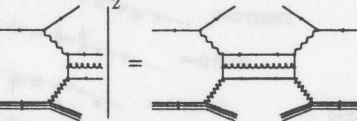
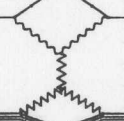
Reaction	QCD Solution	Regge Approximation
a) $A\bar{C} \rightarrow \bar{B}D$		
b) $AB \rightarrow CD$		
c) $AB \rightarrow X$		
d) $AB \rightarrow CX$ (C leading)		
e) Diffractive DIS		

Figure 2.6: Use of Regge approximation to solve scattering processes. The center column shows a sample of the many diagrams required to calculate the scattering process using QCD. On the right, the Regge approach for these processes; the sawtooth line could represent either a meson or Pomeron.

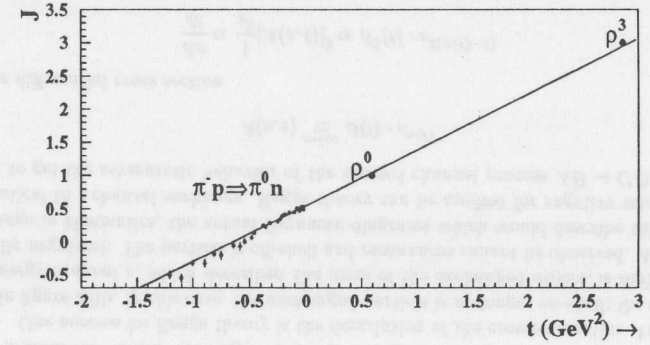


Figure 2.7: The ρ trajectory [27]. The points with $t < 0$ come from the analysis of the reaction $\pi^- p \rightarrow \pi^0 n$.

If applied to the case of elastic scattering where $A = C$ and $B = D$, the formalism predicts the following behavior of the cross section at small $|t|$ [26, 28], applying the tendency of for the momentum transfer squared to be exponentially distributed with slope b_{el} resulting from fits to measured distributions:

$$\frac{d\sigma_{el}^{AB}}{dt} \propto s^{2(\alpha(t)-1)} e^{b_{el}t} \quad (2.10)$$

The optical theorem states that the square of the imaginary part of the forward elastic scattering amplitude is proportional to the total cross section [27]. Thus, the Regge approximation can be expanded to calculate total hadronic cross sections as well, such as that shown in figure 2.6c. One way of describing the optical theorem is to draw a Feynman diagram for $AB \rightarrow X$ and draw the same diagram for the charge conjugate state, $\bar{X} \rightarrow \bar{A}\bar{B}$. By connecting the final and initial particles, the square of the $AB \rightarrow X$ diagram is obtained; these diagrams appear to be the same as those in figure 2.6b. Apparently, the diagram for the square of the total cross section looks much like the elastic diagram. Thus, the Regge calculation of the total cross section would be:

$$\sigma_{tot}^{AB} \propto s^{\alpha(0)-1} \quad (2.11)$$

In principle, the full calculation of a cross section should involve summing over all Regge trajectories that can be exchanged in the considered reaction. In practice, two trajectories are sufficient to describe the energy dependence of hadronic and photoproduction cross sections above the resonant region ($s \gg 3$ GeV). The Reggeon trajectory with intercept $\alpha_R(0) = 0.55$ [29] and slope $\alpha_R' \simeq 1$ GeV $^{-2}$, corresponding to meson exchange, describes the initial fall of the cross sections as the c.m. energy increases. The Pomeron trajectory was introduced to describe the leveling and slight growth of the cross sections at high energy, behavior first predicted by Pomernanchuk [30]. A fit to the hadronic data indicates a Pomeron intercept of $\alpha_P(0) = 1.08$ and slope $\alpha_P' \simeq 0.25$ GeV $^{-2}$ [29]. The Pomeron trajectory corresponds to exchange of vacuum quantum numbers, and should

dominate elastic and diffractive reactions. In the crossed channel the Pomeron trajectory should correspond to a series of hadronic resonances called glueballs. A candidate for such a state with spin $J = 2$ has been observed at mass $m \simeq 1900$ MeV [31]; the large Pomeron intercept should preclude any corresponding $J = 1$ glueballs. However, in the absence of confirmation of a particle-like trajectory, the name Pomeron will be retained in this thesis simply as a description for the phenomenon responsible for diffractive and elastic scattering.

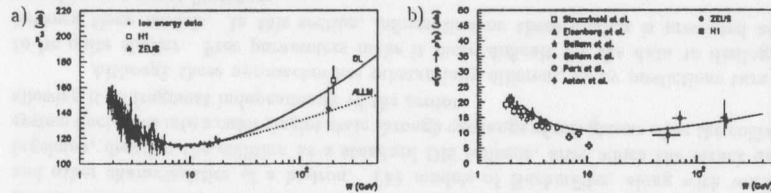


Figure 2.8: (a) The total photoproduction cross section [32, 33, 34] as a function of the c.m. energy W . The lines are the results of a Regge-type of parametrization with $\alpha_P(0) = 1.0808$ (solid) [29] and $\alpha_P(0) = 1.045$ (dotted) [35]. (b) Elastic ρ^0 photoproduction cross section [32, 33, 36, 37, 38] as a function of the c.m. energy W , with a Regge-inspired parameterization [39]

The same values of the Pomeron and the Reggeon intercepts successfully describe also the total cross sections in photoproduction ($\gamma p \rightarrow X$), as illustrated in figure 2.8a including H1 and ZEUS results [32, 33]. The ability of Regge theory to describe photon-hadron interactions may seem surprising but results from fluctuations of the photon into a $q\bar{q}$ state allowing hadron-like interactions. The photon is often described as having a structure function much like the proton. The ALLM parameterization [35] uses a slightly lower value of $\alpha_P(0) = 1.045$. In figure 2.8b, the cross sections for the elastic ρ^0 photoproduction are shown to be consistent with Regge expectations. The line shows the parameterization [39] of the form similar to the equation 2.10 using $\alpha_P(0) = 1.08$.

2.3.1 Application to diffractive dissociation

Experiments with $p\bar{p}$ colliders observed two classes of events in which the final state particles were not distributed according to equation 2.1. One class of events was elastic: $p\bar{p} \rightarrow p\bar{p}$ [40, 41]. Another class had a proton at large rapidity, then a gap in rapidity (or angle) in which no particles were present, $p\bar{p} \rightarrow pX$ [41, 42, 43, 44, 45, 46, 47]. Since (Müller's extension of) the optical theorem [48] was effective in relating the cross-section for this process with the total cross-section, these events were labeled *diffractive*. In analogy with optical diffraction, the proton is said to have diffracted around the black sphere of the \bar{p} , in the process breaking up the \bar{p} . Consequently, the protons travel at small angles and with most of their energy intact.

A similar class of events have been observed in DIS at H1 [49, 50]. These events are characterized by a proton carrying nearly the same momentum as the initial proton, and with little transverse momentum; at H1, these protons are lost in the beam pipe. Additionally, a gap in rapidity is observed between the beam pipe and the first hadronic

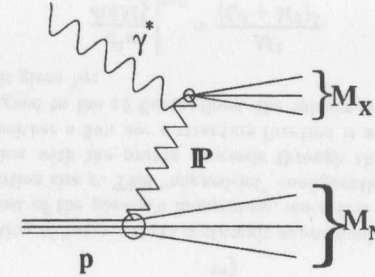


Figure 2.9: Feynman diagram describing a diffractive event in which the proton dissociates.

activity.

Regge theory predicts some features of the inclusive reactions of the type $AB \rightarrow CX$. Thanks to Müller's extension of the optical theorem [48], the high energy asymptotic behavior of the corresponding cross sections may be derived from the forward amplitude for an elastic three-body process $ABC \rightarrow ABC$. If particle C carries the same quantum number and a large fraction of the momentum of A , the reaction describes the diffractive single dissociation process. The behavior of the inclusive cross section may be then calculated in the triple Pomeron asymptotic limit of $M_X^2 \rightarrow \infty$ and $s/M_X^2 \rightarrow \infty$ [28]. The triple Pomeron description comes from figure 2.6d, where the Regge approximation involves a vertex formed by 3 Pomeron intercepts.

$$\frac{d^2\sigma}{dt dM_X^2} \sim \left(\frac{s}{M_X^2}\right)^{2\alpha_P(t)} e^{b_0 t}; \alpha_P(t) = \alpha_P(0) + \alpha'_P t \quad (2.12)$$

A large number of hadron-hadron experiments have confirmed that the above formula correctly describes the diffractive dissociation above the region of low mass resonances. Even at very large center-of-mass energies of $\sqrt{s} = 1.8$ TeV the value of the Pomeron intercept extracted from the M_X spectrum shape [42] is consistent with that obtained from the elastic and the total cross sections.

Diffractive double dissociation

A subset of the single diffractive process, double dissociation in deep inelastic scattering looks like a typical single diffractive reaction, except that the final state proton dissociates into a higher mass state M_N , figure 2.9. The data on this subject is very limited due to experimental difficulties with discriminating between double dissociation process and the non-diffractive interactions. Theoretical understanding is also limited. Diffractive measurements made without direct observation of the final proton will typically have this reaction as a background.

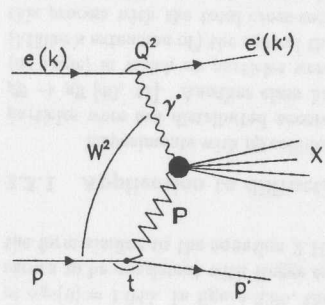


Figure 2.10: Feynman diagram of a diffractive event.

2.4 Diffractive DIS models

Attempts to describe diffraction in DIS have had moderate success, mostly through the use of Regge theory. Three distinct categories have appeared in the literature. Nikolaev-Zakharov attempt to describe the interaction using the BFKL Pomeron, which fixes many characteristics of the interaction. Ingelman-Schlein and Donnachie-Landshoff have used Regge theory, describing the Pomeron as a physical particle which is emitted from the proton. Once emitted, it acts as a normal hadron, and the Pomeron has a structure function and other characteristics of a hadron. The models of Buchmüller, along with work by Ingelman, describe the collision as a standard DIS collision, after which the struck quark system fluctuates into a color singlet state through exchange of soft gluons after the collision, allowing it to fragment independently of the proton.

Although these approaches are substantially different, many predictions turn out to be quite similar. Free parameters make it more difficult for the data to distinguish between these models. In this section, information on these models is presented as an overview on current literature.

2.4.1 Kinematics

The kinematics of diffractive events will be described here as having five degrees of freedom: the electron longitudinal angle and energy, the proton longitudinal angle and energy, and the electron-proton acoplanarity angle between the electron and proton $\Delta\phi$. Additional variables can be attributed to kinematics within the hadronic final state, as discussed in chapter 9. The 5 kinematical variables are easily described by assigning the change in the proton's four-momentum to the Pomeron. The Standard DIS variables, x, Q^2, y, W (section 2.2.1), have the usual definition. Several additional variables are introduced to describe diffractive physics. See figure 2.10 for more information on these definitions. Equation 2.14 is valid in the limit $M_X \gg 0$. Equation 2.15 is valid for $x_L \simeq 1$. An additional

$$x_L = \frac{\text{longitudinal momentum}}{\text{fraction of final proton}} = \frac{E'_p}{E_p} \quad (2.13)$$

$$x_T = \frac{M_X^2 + Q^2 - t}{Q^2 + W^2 + m_p^2} \simeq 1 - x_L \quad (2.14)$$

$$t = \left(\text{four-momentum of Pomeron} \right)^2 \simeq \frac{p_T^2}{x_L} \quad (2.15)$$

$$M_X = \text{invariant mass of Pomeron-photon system } X \quad (2.16)$$

$$\beta = x_{\text{DJ}} \text{ for } \mathbf{P} = \frac{x}{x_T} \simeq \frac{Q^2}{Q^2 + M_X^2} \quad (2.17)$$

$$\Delta\phi = \phi_c - \phi_p \quad (2.18)$$

variable is η_{max} , the maximum rapidity at which a particle is present, not including the outgoing proton. Experimentally, η_{max} is defined by the calorimeter energy deposit with the maximum rapidity, which might be considerably different from the generated value if more than a solitary proton escapes undetected down the beam pipe. $\Delta\phi$ is usually not considered relevant, and thus, a four-dimensional differential cross section is used, often written in terms of the structure function $F_2^{D(4)}$:

$$\frac{d^4\sigma_{diff}}{d\beta dQ^2 dx_T dt} = \frac{2\pi\alpha_{em}^2}{\beta Q^4} (1 + (1-y)^2) F_2^{D(4)}(\beta, Q^2, x_T, t) \quad (2.19)$$

if the longitudinal and parity-violating contributions are ignored. One can also write the differential cross section in terms of Q^2, W, M_X^2 and t , as demonstrated in [51, 52], without any loss of information.

Previous HERA measurements [53, 54] have made the measurements integrated over the entire t range, which gives results for $F_2^{D(3)}(\beta, Q^2, x_T) = \int F_2^{D(4)} dt$ since t could not be measured.

2.4.2 BFKL Pomeron: Nikolaev-Zakharov

The diffractive interaction is viewed [56] as photon diffractive dissociation on a proton, based on earlier development of the BFKL Pomeron [55]. The photon fluctuates in different hadronic states with a wave function which can be expressed as:

$$|\gamma\rangle = |\gamma\rangle_{\text{bare}} + |q\bar{q}\rangle + |q\bar{q}g\rangle + \dots \quad (2.20)$$

The cross section is proportional to the transverse size ρ of these fluctuations, known as *color transparency*,

$$\sigma(\rho) \propto \alpha^2 \rho^2 \quad (2.21)$$

which, for $q\bar{q}$ fluctuations, leads to one of the strongest predictions of the model; since $\rho \propto \frac{1}{m_f}$ (where m_f is the mass of the quark of flavor f):

$$\sigma \propto \frac{1}{m_f^2} \quad (2.22)$$

Therefore, the production of heavy quarks is strongly suppressed. Furthermore, this causes one quark to carry most of the photon's momentum, since this configuration corresponds to the maximal fluctuation size ρ . This "aligned-jet" configuration was anticipated in [57].

The interaction with the proton proceeds through the exchange of two gluons (see figure 2.11) and neither a flux nor a structure function is attributed to the Pomeron. The cross section assigned to the $q\bar{q}$ fluctuations, the valence component of the exchange (dominant at $b > \frac{1}{2}$), is given by:

$$\left. \frac{d^2\sigma}{dt dM_X^2} \right|_{t=0} \propto \frac{M^2}{(Q^2 + M^2)^3}, \quad (2.23)$$

while the cross section corresponding to the $q\bar{q}g$ fluctuations, sea component (dominant for $\beta \ll \frac{1}{2}$), is given, in the triple Regge approach, by:

$$\left. \frac{d^2\sigma}{dt dM_X^2} \right|_{t=0} \approx \frac{\sigma_{\text{TOT}}(\gamma^* p) A_{3P}}{M_X^2} \quad (2.24)$$

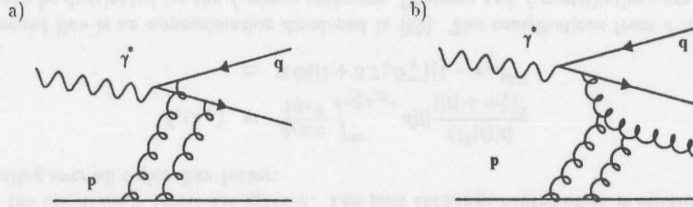


Figure 2.11: Diagrams for the production of $q\bar{q}$ (a) and $q\bar{q}g$ (b) states in the NZ diffractive model.

where A_{3P} is the triple Pomeron coupling. Although the Pomeron in this model is not treated as a particle with a well defined partonic structure, it is possible to give an operational definition of the cross section in terms of a two component (valence and sea) diffractive structure function. Splitting the structure function emphasizes the breaking of factorization predicted by the model. Factorization in this context means an independence of the x_F, t portion of the structure function (process of emission) from the β, Q^2 (photon-Pomeron) dependence. The x_F and β dependence can be factorized for each of the two components separately with the following global result for the cross section:

$$x_F F_2^{D(3)}(\beta, Q^2, x_F) = \frac{\sigma_{TOT}(pp) C_P^2 (m_p^2 x_F^2)}{16\pi B_{3P}} \left[\frac{B_{3P}}{B_{cl}} \phi_{IP}^{val}(x_F) F_{val}^P(\beta, Q^2) + \phi_{IP}^{sea}(x_F) F_{sea}^P(\beta, Q^2) + \phi_{IP}^L(x_F, Q^2) F_{L, val}^P(\beta, Q^2) \right] \quad (2.25)$$

with the factor $\frac{B_{3P}}{B_{cl}}$ arising from the limit $t \rightarrow 0$ of the t -dependent part of the flux factors: $\phi_{IP}(x_F) \exp(-B_{cl}|t|)$ and $f_{IP}(x_F) \exp(-B_{3P}|t|)$.² Their prediction for the longitudinal structure, expected only for $\beta > 0.8$, is included in this expression as well. The x_F dependence is predicted in the theory to be approximately: [36]

$$f_{IP}(x_F); \phi_{IP}(x_F) = \left(\frac{x_F^0}{x_F} \right)^{p_1} \left(\frac{x_F + p_2}{x_F^0 + p_3} \right). \quad (2.26)$$

with $p_1 = 0.569, p_2 = 0.4895, p_3 = 1.53 \cdot 10^{-3}$ for the valence, and $p_1 = 0.741, p_2 = 0.596, p_3 = 0.8 \cdot 10^{-3}$ for the sea. The valence $q\bar{q}$ and sea $q\bar{q}g$ structure functions are defined as:

$$F_{val}^P(\beta, Q^2) = 0.27\beta(1-\beta) \quad (2.27)$$

$$F_{sea}^P(\beta, Q^2) = 0.063(1-\beta)^2 \quad (2.28)$$

Consequently, the valence behavior, including the steep t dependence and $q\bar{q}$ final state, is expected at large β ; the sea component, with the shallower t dependence and $q\bar{q}g$ final state should occur at smaller β .

²The excitation of the $q\bar{q}$ valence is the counterpart of diffraction production of resonances in hadronic scattering and/or real photoproduction, where it is appropriate to use the diffractive slope of elastic πN scattering $B_{cl} \approx 12 \text{ GeV}^{-2}$, whereas excitation of the sea is the counterpart of the triple-Pomeron regime with $B_{3P} \sim \frac{1}{2} B_{cl}$.

2.4.3 Factorizable models

In 1985 Ingelman and Schlein [58] identified the partonic structure of the Pomeron by investigating the reaction $p\bar{p} \rightarrow X\bar{p}$. According to their model, this process could be factorized into the process of emission of a Pomeron and its interaction with the antiproton. Thus, the Pomeron, once emitted, behaves as any other hadron; it therefore has a structure function and parton density functions much like the proton.

The differential cross section for the process $ep \rightarrow epX$ can be written as:

$$\frac{d^5\sigma(ep \rightarrow epX)}{dQ^2 dx dx_F dt dp_T^2} = f_{IP/p}(x_F, t) f_{g(q)/IP}(\beta) f_{\gamma/c}(x, Q^2) \frac{d\hat{\sigma}(\gamma g(q) \rightarrow X)}{dp_T^2} \quad (2.29)$$

where $f_{IP/p}(x_F, t)$ is the flux factor describing the flux of Pomerons in the proton:

$$f_{IP}(x_F, t) = \frac{1}{2} \frac{1}{2.3 \cdot x_F} \cdot (6.38 e^{8t} + 0.424 e^{3t}) \quad (2.30)$$

Given the hypothesis of factorization at the $IP-p$ vertex, f_{IP} is universal and can be extracted from hadron-hadron scattering data. $f_{\gamma/c}(x, Q^2)$ is the photon flux. $\frac{d\hat{\sigma}(\gamma g(q) \rightarrow X)}{dp_T^2}$ is the matrix element for the hard scattering, in which $\gamma^* g \rightarrow q\bar{q}$ should dominate, with the production of high p_T jets in the final state. $f_{g(q)/IP}$ represents the parton densities inside the Pomeron, which, as a consequence of factorization, are independent of the process of emission. Given its quasi-hadronic nature, the Pomeron is treated as a particle and a structure function can be defined as:

$$F^P(\beta, Q^2) = \sum_i c_i^2 [\beta q_i(\beta) + \beta \bar{q}_i(\beta)] \quad (2.31)$$

The normalization of the parton densities is determined by the fulfillment of the momentum sum rule.

In the Donnachie-Landshoff [29] (DL) model, diffraction in DIS is described as Pomeron exchange between virtual photon and proton, with the Pomeron coupling predominantly to quarks, in analogy with the photon. The authors calculate the cross section in the framework of Regge theory:

$$\frac{d^2\sigma}{dt d\beta} = f_{IP}(x_F, t) \cdot F_{q/IP}(\beta, Q^2) \quad (2.32)$$

The flux factor

$$f_{IP}(x_F, t) = \frac{9\beta_0^2}{4\pi^2} F_1(t)^2 x_F^{1-2\alpha(t)} \quad (2.33)$$

is related to the elastic form factor of the proton $F_1(t) = \frac{4M^2 - 2.8t}{4M^2 - t} \left(\frac{1}{1-t/0.7} \right)^2$ and to the Pomeron-quark coupling, $\beta_0 \simeq 1.8 \text{ GeV}^{-1}$, extracted from hadron-hadron data. The Pomeron trajectory is the "soft" one, i.e. $\alpha(t) = 1.08 + 0.25t$. The similarity between the Pomeron and the photon leads to a quark structure function $F_{q/IP}$ of the form:

$$F_{q/IP} = \frac{1}{3} C' \pi \beta (1-\beta), \quad (2.34)$$

with $C \approx 0.25$ for each light quark and antiquark. As with the photon structure function, a "soft" structure function contribution must be added at low β in the form $\beta^{-\epsilon_0}$ (with $\epsilon_0 \approx 0.08$ or larger). No prediction is made for the Pomeron's gluon structure function; as the Pomeron is a Regge trajectory instead of a particle, there is no momentum sum rule.

Many other theories have used a similar premise, with expanded analysis of the Pomeron structure function, for example [60, 59, 61].

2.4.4 Partonic models of diffraction

A non- IP model has been developed by Buchmüller and Hebecker [62] which describes diffractive interactions as ordinary DIS. However, instead of the struck quark leaving the proton and fragmenting in the standard manner, this model predicts that colored system will interact substantially with the gluons within the proton. These soft interactions lead to the production of either a color octet or color singlet state, with probabilities $\frac{8}{9}$ and $\frac{1}{9}$, respectively. This leads to the prediction that diffraction should account for 1/9 of the proton structure function. They further predict a simple scaling law to relate the diffractive and proton structure functions:

$$\xi F_2^{D(3)}(\beta, Q^2, x_p = \xi) = 0.04 F_2(x = \xi, Q^2) \quad (2.35)$$

2.5 Reggeon exchange in DIS: non-Pomeron exchange

While diffraction should be the dominant source of events for small x_p , with increasing x_p other sources are expected to contribute. From the Regge approach, one would expect that the exchange of Reggeons besides the Pomeron would contribute [64, 65, 66, 67]. In [68], Nikolaev and Zakharov have added to their $F_2^{D(3)}$ definition in a manner which presumably could extend other diffractive models equally well. An additional term contributes to $F_2^{D(3)}$ of the form

$$F_2^{LP(3),M}(\beta, x_p, Q^2) = \frac{f_f^2 G_p^2(m_p^2 x_p^2)}{8\pi B_{3M}} F_2^f(\beta, Q^2) + x_p f_\pi(x_p) F_2^\pi(\beta, Q^2) \quad (2.36)$$

The first term corresponds to f exchange, and the second to π^0 exchange.³ For the moment, the interference terms are ignored. The pion exchange contribution is obtained by integrating over all t pion flux factor:

$$f_\pi(x_p) = \frac{g_{\pi NN}}{16\pi^2} \int_{m_\pi^2 x_p^2}^{\infty} d|t| \frac{G^2(t)|t|}{(|t| + m_\pi^2)^2} \quad (2.37)$$

$$\simeq 0.66(1 + 5.7\sqrt{x_p})(1 - x_p)^{3.3} \quad (2.38)$$

The second line is an approximation developed in [69]. The contributions from π appear to always be dominated by the f meson exchange. Pomeron and f contributions are equal at approximately $x_p = 0.1$, according to the assumptions used in [68], with little Q^2 dependence but some β dependence, increasing f contributions as β decreases. However,

³For experiments which do not directly observe the final proton, the π exchange contribution triples due to the addition of a neutron final state.

the exact normalization of the f contribution can only be estimated. In this analysis, the possibility that some f exchange contributes to the observed data sample must be considered.

2.6 Summary

The introduction of QCD has improved our understanding of hadronic processes, and there is every reason to expect that this is the correct theory for these interactions. However, soft interactions limit the ability for predicting hadronic behavior. Deep inelastic scattering has illuminated the power of QCD, but diffractive deep inelastic scattering is interesting because the approaches taken to understand this reaction combine the soft and hard aspects of QCD. More experimental data will help to understand how the diffractive interaction should be interpreted.

Chapter 3

HERA and ZEUS

Initial efforts at deep inelastic scattering were phenomenally successful [15]. The desire to further understand the structure function at small x and its evolution to very large Q^2 motivated DIS research at larger center-of-mass energy \sqrt{s} . Such an increase was achieved at Deutsches Elektronen-Synchrotron (DESY) in Hamburg, Germany. Both proton and electron were accelerated to form the first hadron-electron collider. Collecting physics in a collider presents numerous technical challenges to both accelerator and experimental physicists. A few of these tasks are summarized in this chapter. However, since the Leading Proton Spectrometer (LPS) plays such a crucial role in this analysis, considerable detail is given to this component in the next chapter.

3.1 HERA electron-proton collider

The HERA (Hadronen-Elektronen Ring Anlage) accelerator [70] is designed to collide 820 GeV protons with 30 GeV electrons. Two storage rings are used, placed in a 6.3 km tunnel 10-25m underground. Keeping particles in this orbit requires strong magnetic fields, which are provided by 4.6 T superconducting dipole magnets for the protons; the magnetic field limits the maximum energy for protons. Electrons' maximum energy at HERA is limited by the power dissipated through synchrotron radiation, which must be replaced to maintain the electron orbit. Superconducting radio frequency cavities, powered by microwave klystrons, provide a total power of 13.2 MW. The two oppositely-circulating beams collide in two experimental halls, where the ZEUS and H1 detectors are installed.

The coordinate system used in this thesis is the "nominal proton beam" reference frame, in which the design location of the proton beam defines the $z = 0$ axis, and the y direction is vertical. Polar angles are defined as θ for the angle from the z axis, and ϕ for the angle from the x axis, in the standard polar-angle format. The center of the design interaction point is at $x = y = z = 0$, although in practice the colliding beams have offsets from the design location. Note that this coordinate system is different from the standard ZEUS coordinate system for distances far from the interaction point (and far from the central ZEUS detector), after the proton beam is bent by the final focus magnets, since the ZEUS z axis does not follow the bends of the proton beam. Within the central detector region, this difference is negligible.

HERA parameters	Design values		1994		1995	
	e^-	p	e^+	p	e^+	p
Energy (GeV)	30	820	27.5	820	27.5	820
Instantaneous luminosity ($\text{cm}^{-2}\text{s}^{-1}$)	$1.7 \cdot 10^{31}$		$2.3 \cdot 10^{30}$		$6.0 \cdot 10^{30}$	
Specific luminosity ($\text{cm}^{-2}\text{s}^{-1}(\text{mA})^{-2}$)	$3.9 \cdot 10^{29}$		$3.4 \cdot 10^{29}$		$4.0 \cdot 10^{29}$	
Integrated luminosity (pb)	-		6.0		12.0	
Circumference (m)	6336		6336		6336	
Magnetic field (T)	0.165	4.65	-		-	
Injection energy (GeV)	14	40	11	40	11	40
Current(mA)	58	163	28	38	32	65
Number of bunches	210		153+15	153+17	173+15	173+7
Bunch crossing time (ns)	96		96		96	
Beam σ_x (mm) at IP	0.30	0.27	0.27	0.18	0.27	0.18
Beam σ_y (mm) at IP	0.06	0.09	0.06	0.06	0.06	0.06
Beam σ_z (cm) at IP	0.8	11	0.8	11	0.8	11
β (horizontal)	2	10	2	7	2	7
β (vertical)	0.9	1	0.9	0.7	0.9	0.7
Injection time (min.)	15	20	45	60	45	60
Efficiency	33%		-		-	

Table 3.1: HERA design parameters and actual performance in 1994-95

3.2 Overview of ZEUS detector

The ZEUS collaboration [71, 72] includes over 300 physicists, and the detector has been constructed with the help of many additional technicians at the home institutions of the physicists. Two approaches are generally used to analyze the particles in the final state of the ep collision: Tracking detectors trace the path of a charged particle as it bends in a magnetic field, while calorimeters determine the energy of charged or neutral particles by stopping the particle and measuring the total energy deposited in the material. A large number of smaller detectors, *components* of the ZEUS detector, allow for thorough characterization of the ep final state. Figure 3.1 and 3.2 show the central portion of the ZEUS detector.

Like many modern high-energy physics colliding-beam experiments, the ZEUS detector is solenoidal with a calorimeter which covers nearly the entire solid angle around the interaction point, except for two small holes for the beam pipe. A strong magnetic field of 1.4 Tesla provided by a superconducting solenoid allows for transverse momentum determination.

Of the components in the ZEUS detector, those important for this analysis are the *Uranium Calorimeter*, *Central Tracking Detector*, *Luminosity Monitor*, and *Leading Proton Spectrometer*; the latter is discussed in chapter 4. Other components which will be mentioned on occasion include the *proton remnant tagger* [73] and *forward neutron calorimeter* [74]. Data taking uses a three-level *trigger*.

Overview of the ZEUS Detector
(longitudinal cut)

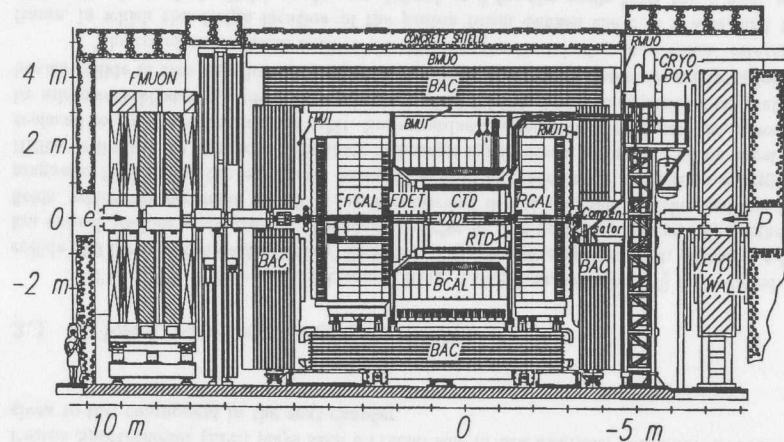


Figure 3.1: A cross-section of the ZEUS detector along the beam pipe (along the $x = 0$ plane), showing the central components.

3.3 Central Tracking Detector

The central tracking detector (CTD) [75] surrounds the vertex detector. It extends from an inner radius of 16.2 cm to an outer radius of 82.4 cm and has a length of 240 cm. The inner structure of the CTD consists of 72 cylindrical drift chamber layers organized in 9 superlayers. The superlayers alternate between those with wires parallel to the beam axis (axial layers) and those with wires inclined at a 5° angle to provide a stereo view. The stereo layers as well as the measurement of the time of the pulse arrival to both ends of the sense wire (z -by-timing) allow for z position of a track to be measured. A spatial resolution of $260 \mu\text{m}$ has been achieved.

3.4 Uranium Calorimeter

This sampling calorimeter [76] is constructed as a sandwich of depleted uranium absorber plates and scintillator tiles. Particles incident on the calorimeter will shower, with charged particles inducing a light response in the scintillators. This light pulse travels through a wavelength shifter and is readout in a photomultiplier tube.

The calorimeter is divided into three parts: the forward (FCAL) covering the pseudorapidity region $4.3 > \eta > 1.1$, the barrel (BCAL) covering the central region $1.1 > \eta > -0.75$, and the rear (RCAL) covering the backward region $-0.75 > \eta > -3.8$ (figure 3.3). Holes are cut in the center of the RCAL and FCAL to allow for the HERA beam pipe, with

Overview of the ZEUS Detector
(cross section)

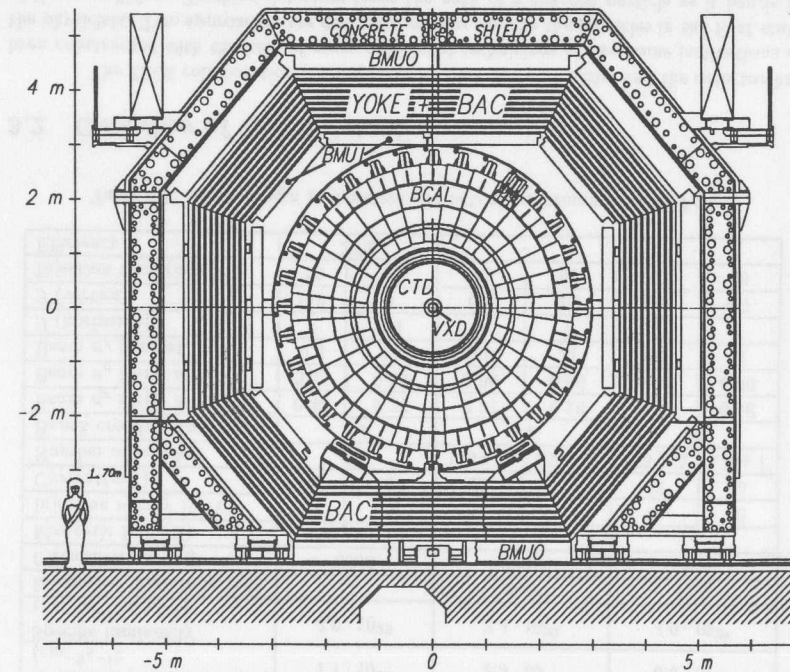


Figure 3.2: Cross section of the ZEUS detector perpendicular to the beam pipe.

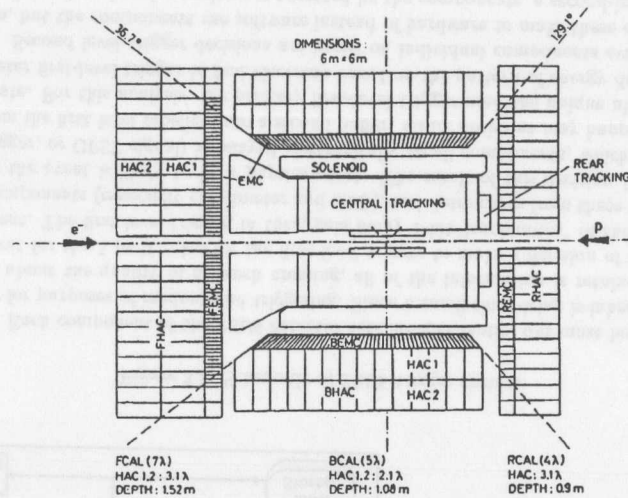


Figure 3.3: A diagram of the ZEUS calorimeter.

sizes of 20×20 cm.¹ Each calorimeter is further subdivided into *towers* measuring 20×20 cm (transverse to the beam). Towers are subdivided into electromagnetic and hadronic sections, and the electromagnetic sections are further subdivided to improve spatial resolution. Each cell uses two photomultiplier tubes for readout, improving position resolution, and providing redundancy and noise suppression.

Under test-beam conditions, the energy resolution determined for the calorimeters is

$$\sigma_E/E = \frac{0.18 (0.35)}{\sqrt{E}} \quad (3.1)$$

for electromagnetic (hadronic) particles. Good hadronic response was achieved through *compensation*. By tuning the scintillator and uranium thickness in the calorimeter, hadronic and electromagnetic showers give identical response.

The use of photomultipliers and scintillator allow measurement of the time a particle hits the calorimeter, with resolution of approximately 1 ns. This information is used for reducing backgrounds.

3.5 Small Angle Rear Tracking Detector (SRTD)

Measurements of the electron energy suffered from poor resolution due to the dead material present in front of the calorimeter, mostly cables and endplate for the tracking de-

¹For the 1995 and later runs, the cutout for the beam pipe was reduced to (10×20) cm in the rear direction, to increase acceptance of low-angle electrons.

tor. This dead material caused many electrons to shower before reaching the calorimeter, causing the calorimeter to read anomalously small energy values. The SRTD [77] corrects this problem by sampling the number of charged particles incident on the calorimeter, and this information about the state of the shower as the electron reaches the calorimeter is used to correct the energy measured in the calorimeter. Additionally, the electron position is determined more precisely by using thin (1 cm) strips of scintillator fiber to determine the center of the shower. A diagram of the SRTD layout is shown in figure 3.4.

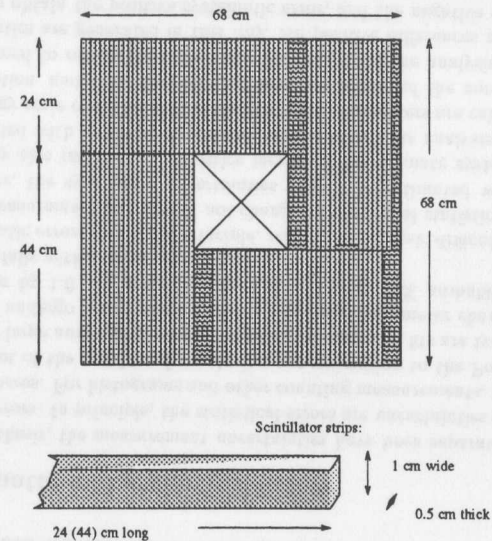


Figure 3.4: A schematic of the SRTD showing the orientation of the scintillator strips in the two orthogonal planes.

3.6 Luminosity Monitor

Two calorimeters, mounted at $z = -35$ m and $z = -107$ m, accept events of the form $ep \rightarrow e\gamma p$, for which the (Bethe-Heitler) cross-section is well-known. The rate of coincidences between the two calorimeters determine the physics luminosity delivered [78, 79, 80].

3.7 ZEUS trigger system

The ZEUS detector must be able to detect an ep collision during any of the 10^7 bunch crossings which occur each second. In order to distinguish and readout physics

events, an complex three-level trigger and data acquisition (DAQ) system has been developed (figure 3.5) [81].

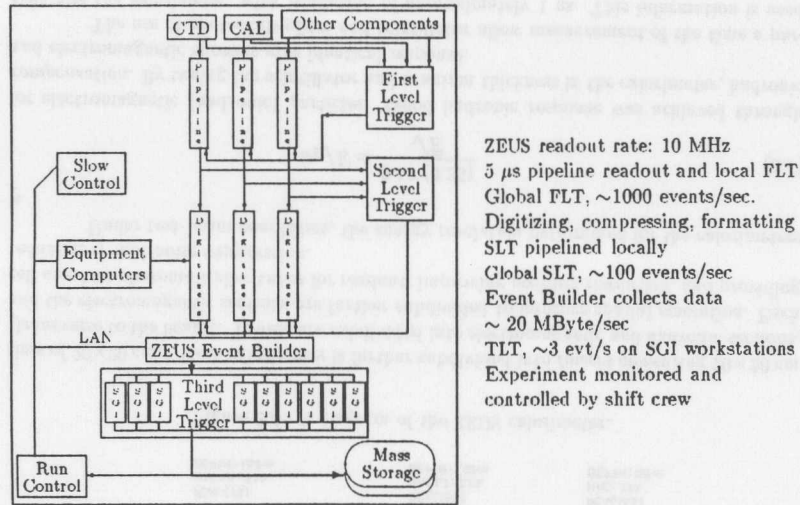


Figure 3.5: Schematic of ZEUS trigger system.

Each component of the ZEUS detector acts independently, but must be interfaced together for purposes of readout and triggering. Since a small time delay is inherent in any decision about the quality of a bunch crossing, all of the information is retained by each component for the 5 μ s it takes for the first level trigger to make a decision of the quality of an event. The first level trigger, in turn, gets many 1-bit "summaries" of the data from many components (especially calorimeter and CTD), and determines from these trigger bits whether the event is likely to be a physics event. The result of this decision (global first level trigger, or GFLT signal) is relayed electronically to all components, which copy their data from the first level pipeline into a second buffer. GFLT decisions may happen at up to 1 kHz rate. For this analysis, the primary first-level trigger used the unique ability of the calorimeter first-level trigger to find electrons based on the pattern of energy deposited.

Second level trigger decisions are based on individual components evaluations of the data, but the components use software instead of hardware to make these decisions. If the data for a given bunch crossing are accepted by the components, a second-level decision is issued, which make the components copy their data to the ZEUS Event Builder.

The Event Builder [82] combines and formats all of the component data into one data set. These data are referred to as an event, and are transferred to the third level trigger (TLT). A farm of 36 Silicon Graphics workstations evaluate the data and make cuts similar to those described in chapter 6, to determine which events are likely to be desirable

physics events. The cuts applied offline are always tighter than the TLT cuts.

3.8 Offline analysis

The ZEUS experiment produces up to 1 MB of physics data each second. These data are stored on tape operated by an AMPEX tape robot with a total storage capacity of 6 TB. The events are processed offline using the ZEUS reconstruction program ZEPHYR. The reconstruction program reconstructs physics variables (energy, momentum of particles) based on the raw data collected by the components, typically using calibration information. A typical event then consumes 26 kB when only physics data are included. A farm of 600 GB of fast hard discs connected to an Silicon Graphics multiprocessor computers [83] allow for users in the ZEUS collaboration to run analysis jobs on the reconstructed data.

3.9 Systematic and statistical errors

In this thesis, the measurement uncertainties have been separated into *statistical* and *systematic* errors. In principle, the statistical errors are uncertainties caused by limited statistics on a process. For histograms and other counting measurements, this is determined by the square root of the number of events (an approximation to the Poisson distribution which is valid for large numbers of events). Statistical errors on fits are typically the change a parameter can undergo before the log of the likelihood parameter changes by 0.5 or the χ^2/DOF changes by 1.0. In principle, there should be a 68% probability that the true parameter value falls within these error bars.

Systematic errors should, in principle, reflect the intrinsic difficulties this setup has in making the measurement and should not change as additional statistics are obtained. In practice, however, the systematic uncertainties cannot be estimated when statistics are limited, and may also improve as statistics increase. To estimate systematic errors, the analysis is repeated with a change in one assumption about the analysis (for example, the calorimeter energy scale could be shifted slightly). All parameters are calculated under this changed assumption, and the differences between the results of the nominal and changed analyses is assumed to reflect the systematic uncertainty in the analysis. A large number of these systematics are generated in this way. All positive differences are added together in quadrature to obtain the positive systematic error, and the negative systematic error is obtained the same way. This assumes that all systematic checks are uncorrelated.

Plot shown in this thesis with dual error bars indicate the statistical error with the inner error bar and the statistical plus systematic error added in quadrature with the outer error bar. Readers are advised that the "true" value of a measurement is expected within those errors with a 68% confidence level.

Chapter 4

LPS Hardware and Reconstruction

The physics potential of leading protons has been demonstrated by the success of experiments at the hadronic colliders [44, 46, 84, 41, 47]. This encouraged the development of the ZEUS Leading Proton Spectrometer (LPS). Detecting particles which would otherwise escape undetected through the beam pipe is a difficult task, which has been addressed using a combination of silicon microstrip detector technology with Roman pots for inserting the detectors into the proton beam pipe. Section 4.1 describes the apparatus for the LPS. Operation of these detectors required careful coordination between the LPS group, IHERA, and ZEUS, and these issues are discussed in section 4.2.

Two major tasks are necessary to determine physics information from the raw LPS data: *reconstruction* and *alignment*. The LPS reconstruction software takes as input the raw hits, plus alignment and magnet information, to determine reconstructed momenta of protons, as described in section 4.3. The alignment information is obtained by carefully analyzing physics tracks observed in the LPS, using the approach described in section 4.4.

The LPS detector has proven to be successful in its goal of observing leading protons at IHERA.

4.1 LPS detector

Silicon microstrip technology has improved the precision with which tracking detectors can operate. The LPS successfully implemented the *binary* readout scheme, which condenses the information from an individual strip into a single bit indicating whether a particle hit that strip. The binary readout method is further described in section 4.1.1. Custom bipolar and CMOS readout hardware were implemented, and these electronics are explained in section 4.1.2. The challenging data-taking environment of the LPS requires that the detectors be movable; section 4.1.3 describes the hardware of these re-entrant Roman pots.

4.1.1 Silicon detectors and binary readout

A *PIN* diode is a slight modification of the standard diode (a junction between *p* and *n* type semiconductor), formed by inserting a very lightly doped, inert material between the *p* and *n* implants. The volume of inert material can be depleted of all charge carriers when the diode is reverse-biased. A charged particle passing through the depleted

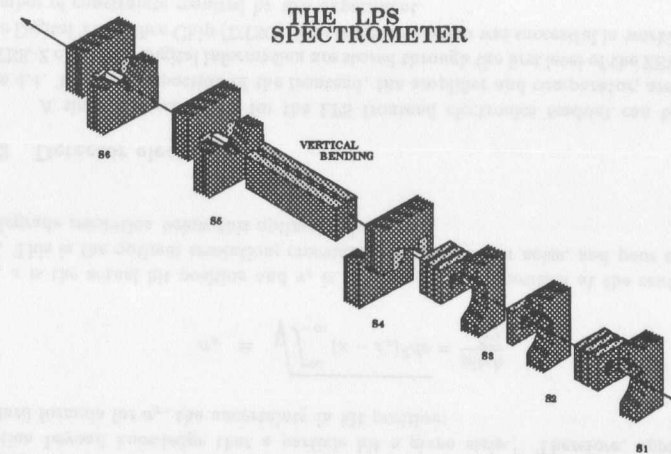


Figure 4.1: Layout of the LPS detectors in the beampipe east of the ZEUS detector. The small trapezoidal detectors on S4-S6 Up are trigger planes. The horizontal scale is compressed in this diagram. The detector lies to the left of the ZEUS diagrams in figures 3.1 and 3.3.

semiconductor produces pairs of electrons and holes, which then travel to the terminals of the diode producing a small electrical signal. Silicon microstrip detectors are a particular geometry of reverse-biased PIN diode. Each diode has a junction which is fabricated as a long, thin strip on the surface of the silicon; signals from a passing charged particle are quickly collected by this junction as shown in figure 4.2. For the ZEUS LPS, detectors are fabricated from a 300 μm thick piece of lightly-doped *n* type silicon, into which 448-1024 *p* type strips are implanted to form diode junctions. Immediately above the implants, conductors carry the signal and leakage current to the frontend electronics (DC-coupled biasing) while a large positive voltage is applied to the backplane.

For this experiment, the detectors are fabricated with strip pitch of either 115 (*x*, *y* views) or $115/\sqrt{2}$ (*u*, *v* views) μm , and lengths of up to 10 cm. One crucial consideration for designing low-noise detectors is the capacitance of the detector, which can be determined as the sum of capacitance between the strip and backplane, and the strip and nearest and next-nearest neighbors (approximately 1 pF/cm). In order to maximize the acceptance of proton tracks, the detectors are designed to operate as closely to the proton beam as IHERA would allow, at a constant distance of 10σ . This design requires elliptical cutouts to be made in the silicon, with the cutout dimensions customized for each station based on beam optics.

One ionizing particle typically produces 25,000 electrons of signal at the input to the amplifier. Detecting such a small signal is a challenge. The ZEUS LPS uses the binary readout scheme: For each channel of microstrip detector, the only recorded data is the presence of a charged particle in that strip. By only keeping one bit of information, the

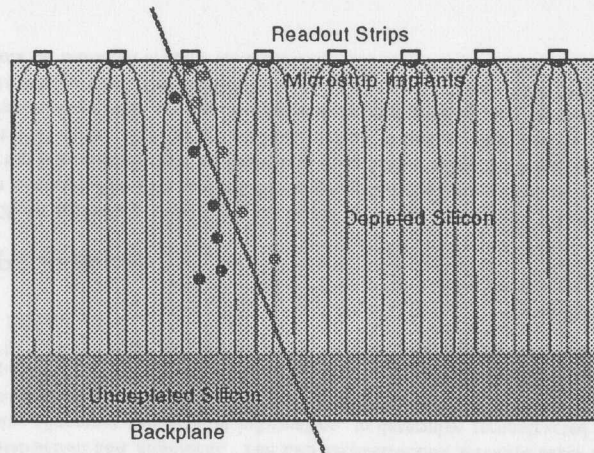


Figure 1.2: Silicon detector functional description. A charged particle (diagonal line) generates electron-hole pairs in the depleted silicon, which are observed as a charge on the readout strips at the top of the diagram.

data analysis is much simpler and readout costs are much lower [85].

In order to understand the performance of binary detectors, the analog readout concept of signal-to-noise ratio must be replaced by the binary concepts of noise occupancy and efficiency. Efficiency indicates what fraction of charged particles result in a digital signal to the readout, and should be large (typically > 99%). Noise occupancy indicates how frequently the detector records a hit in the absence of any charged particles during any given readout period, and should be smaller than 1 hit per plane per event. If efficiency is high and noise occupancy is low, then reconstructing charged particle tracks through multiple planes can be done with little ambiguity and minimal complexity in the analysis software.

Calibration of binary readout is slightly more complicated than for analog readout. The approach developed for this readout method is to measure occupancy (fraction of events with a hit) as a function of threshold voltage, while a fixed charge is injected into the amplifier frontend. For thresholds much below the input charge, occupancy is 100%, and for large thresholds the occupancy is 0. Between these two extremes, the occupancy represents the integral of the amplifier response function up to the threshold voltage. Since noise response is accurately described by a Gaussian, the integral function appears as an error function. The test procedure, shown in figure 1.3, determines the occupancy as a function of threshold voltage for two different input charges. Each result is fit to an error function, which yields the parameters *response* (threshold at which occupancy is 50%) and noise σ . The difference between the response for two input charges curves indicates the small-signal gain and the σ indicates the amplifier noise.

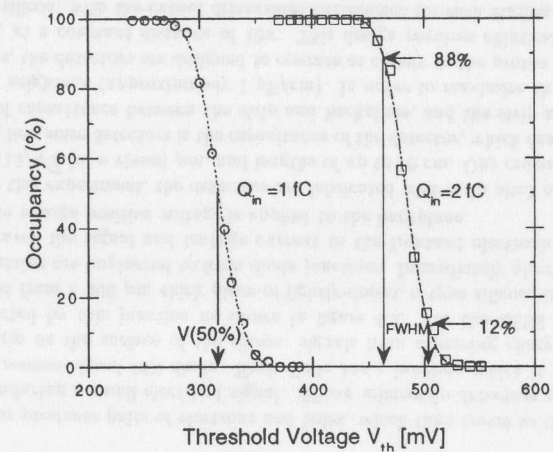


Figure 1.3: Example of calibration procedure for the binary readout system.

Noise occupancy can be related to the σ of amplifier noise using the error function [86]. Unlike the case with analog readout, there is no attempt to improve on position detection beyond knowledge that a particle hit a given strip.¹ Therefore, applying the standard formula for σ_x , the uncertainty in hit position:

$$\sigma_x = \sqrt{\int_{-\infty}^{\infty} (x - x_c)^2 dx} = \frac{\text{pitch}}{\sqrt{12}} \quad (4.1)$$

Here, x is the actual hit position and x_c is the measured hit position at the center of the strip. This is the optimal resolution; crosstalk, δ rays, detector noise, and poor alignment can degrade resolution below this optimal value.

4.1.2 Detector electronics

A simplified schematic for the LPS frontend electronics readout can be seen in figure 4.1. The analog portion of the frontend, the amplifier and comparator, are found in the TEK-Z chip [87]. Digital information are stored through the first level of the ZEUS trigger in the Digital Time Slice Chip (DTSC). The frontend system was successful in working within a number of constraints required by this experiment.

¹Some slight improvement could be obtained for particles near the boundary between two strips, which give signals in two adjacent strips. This generally does not substantially change the resolution, since it occurs in only 10-20% of the tracks. However, in order to take advantage of any charge sharing which does occur, the hit position for all two-strip clusters are placed at the boundary between the two strips.

TEK-Z amplifier-comparator chip

The close proximity to the proton beam, and the high flux of synchrotron radiation from the electron beam, result in high radiation doses. For the digital chip, a radiation-hard CMOS process was used (section 4.1.2). Careful design of the analog TEK-Z ensures that radiation, which changes transistor response, will not change the characteristics of the amplifier. Both chips were tested with large γ (5 Mrad ^{60}Co) and proton fluences.

The pitch of the silicon detectors was relatively small, requiring that the amplifiers and comparators fit within $115\ \mu\text{m}$ per channel including service connections at the sides of the chip.

The detector response needs to be fast in comparison with bunch crossing time at IIERA (96 ns), and should match the time required to collect holes in the detector. Using a shaping time of 30 ns actually allows out-of-time signals to be ignored by the readout, further reducing noise occupancy. Both noise and power consumption should be minimized; TEK-Z design keeps noise below $\sim 1000e^-$ and power below 2 mW/channel. The DC-coupled detectors place leakage current into the front-end of the readout. The TEK-Z amplifier can sink currents of $1\ \mu\text{A}$ per channel and still detect silicon signals.

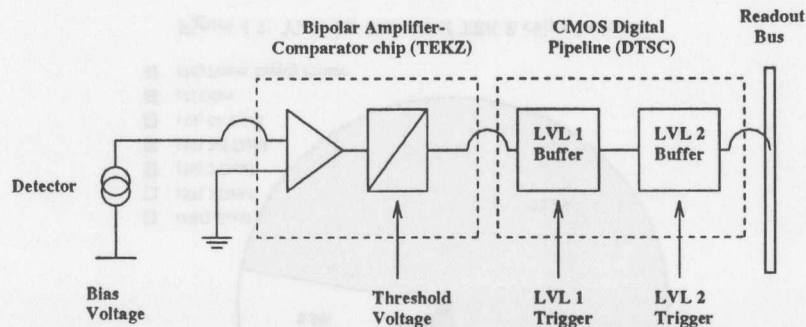


Figure 4.4: Schematic of Binary Readout Technique, as implemented for the LPS.

Manufactured in SHP1 by Tektronix corporation as a full custom VLSI chip, the TEK-Z combines 64 amplifier-comparator circuits; a simplified schematic of one channel is shown in figure 4.5. Each channel has three stages of amplifier, with test points available for investigating signals after each stage.

A small input capacitor of 14 fF allows charge to be injected at the amplifier input for testing the amplifier and readout. This unusually small capacitor was found to have variations between the channels, probably due to inconsistencies in the layout procedure, although stray capacitance might also be an issue. Consequently, the actual value of the calibration capacitor was measured in the lab, rather than using fixed design values. The measured values compared well with the uncorrected gains, as shown in figure 4.6. This agreement demonstrates the good matching in true gain values across channels, and further analysis of the TEK-Z always includes the channel-by-channel calibration capacitance values.

The TEK-Z was tested by sending charge into the amplifier via the calibration

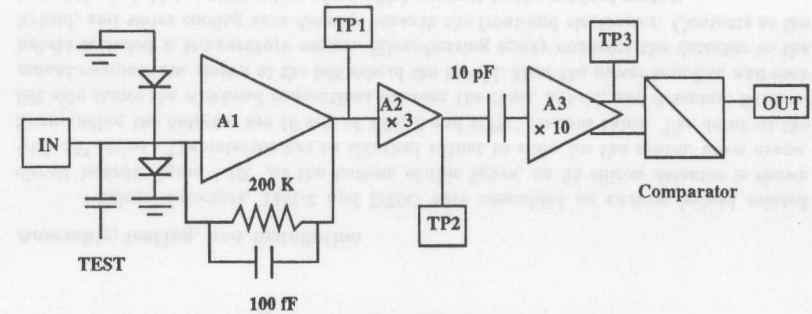


Figure 4.5: Simplified TEK-Z schematic.

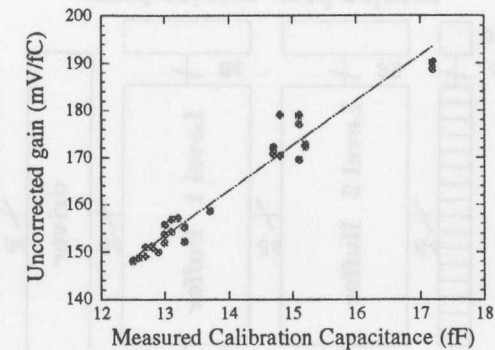


Figure 4.6: Correlation between uncorrected gain and measured calibration capacitance.

capacitors, as described in section 4.1.1. Yield tests indicate that the primary failure was single channel failure, probably due to transistor failures in fabrication. Two wafers had additional failures characterized by short circuits between power supply and ground. Overall yield was high, as shown in figure 4.7 [88].

The gain and noise were also measured during yield testing, as shown in figure 4.8. The gains were highly uniform, with RMS variation of 4%; this uniformity is crucial since all channels on one detector hybrid use the same threshold voltage. Average noise determined in the yield test was 17.2 mV or 660 electrons, which agrees well with simulations.

Digital Time Slice Chip (DTSC)

Information about hits in the detector is transferred from the TEK-Z to the DTSC chip [89]. The DTSC performs two functions: Storing information until the ZEUS first level trigger is complete, and allowing for serial readout of the data. Each bunch crossing, the

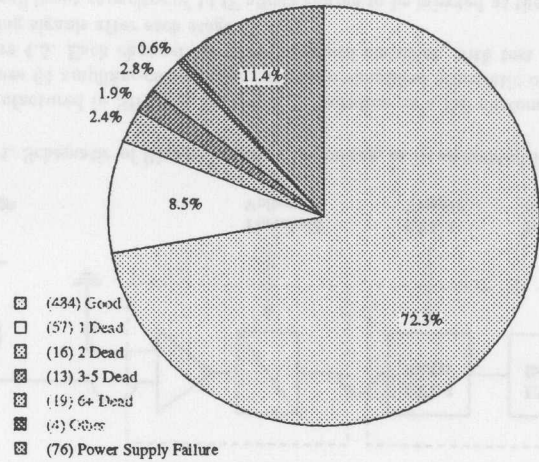


Figure 4.7: Yield for first set of TEK-Z chips tested.

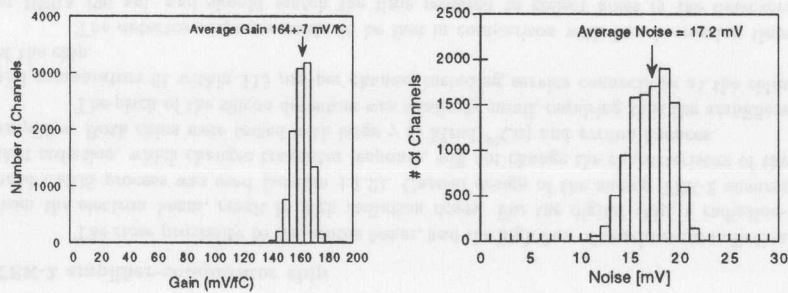


Figure 4.8: TEK-Z gain and noise values from yield test.

comparator outputs are shifted into a register (level 1 buffer), where they are stored while waiting for the ZEUS trigger system (figure 4.9). The level 1 buffer has 64 locations, allowing for a trigger latency of 6 μ s at the IIERA clock rate of 10 MHz. The first level trigger causes the DTSC to copy the memory into the level 2 buffer. Shortly after the first level trigger, the readout sequence begins.

Testing on the DTSC was performed by the fabrication facility UTMIC, based on a set of test vectors derived from simulation. UTMIC used a radiation hard CMOS process to fabricate the DTSC.

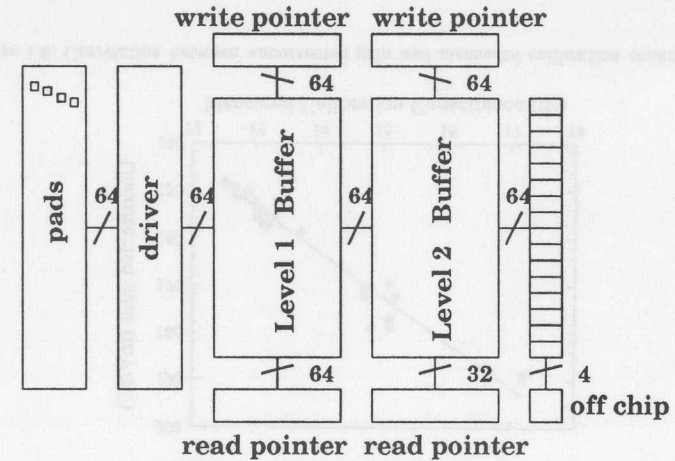


Figure 4.9: DTSC simplified schematic.

Assembly, testing, and installation

Silicon detectors, TEK-Z and DTSC were assembled on custom hybrid printed circuit boards, figure 4.10. At the bottom of this figure, an S1 silicon detector is shown with 45° strips. The detector has an elliptical cutout to allow for the proton beam shape. Surrounding the detector are 16 sets of TEK-Z and DTSC readout chips. The detail at the left side shows the wirebond connections between the chips, hybrid, and detector. Surface-mount components, shown at the left side of the hybrid, filter the power supplies, and each hybrid included a temperature sensor. Silver-bearing epoxy connects the detector to the hybrid, and water cooling runs directly beneath the front-end electronics. Contacts at the top of the hybrid are soldered to wires which connect to the readout system.

The hybrids went through several test steps [90]:

- Each detector was checked for shorts, leakage current, and depletion voltage.
- Each hybrid was checked for continuity and shorts.

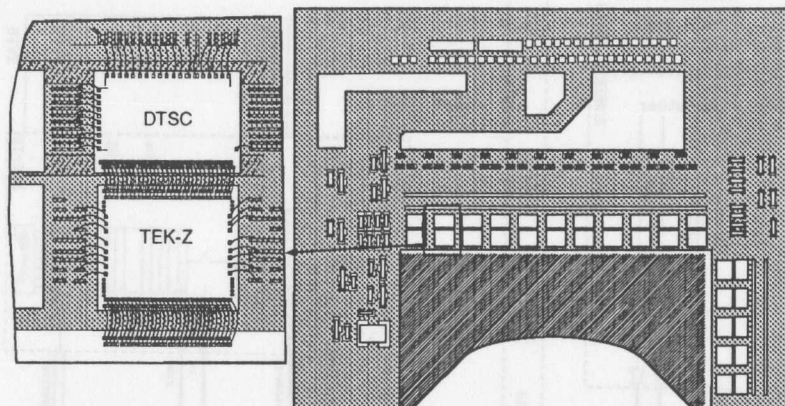


Figure 4.10: Layout of an LPS hybrid. One pair of DTSC and TEK-Z chips are magnified at the left, showing the wirebonds connecting the detector and electronics.

- After connecting all electronics, but prior to attaching a detector, the frontend electronics were thoroughly tested and reworked as necessary.
- After connecting the detector, the frontend was retested, followed by a signal test using a 1064 nm laser, which simulates a charged particle traversing the detector.

The LPS detectors have strips of varying length, and this provides an opportunity to test the noise as strip length, and consequently capacitance at the amplifier input, varies. This comparison agrees well with the predictions based on detector simulations, shown by the line in figure 4.11. Since the simulation does not include additional noise sources due to leakage current or power supplies, this agreement is reasonable. Note that these data were taken while the hybrid was installed at ZEUS.

Assembled detectors were installed in the ZEUS detector according to the time line shown in section 4.4.1. A completed hand contains six LPS planes, oriented in three different views (0, +45°, -45°). A Faraday cage shields these six hybrids from electromagnetic interference.

Readout chain

Figure 4.12 shows a block diagram of the entire readout chain. The portions of the readout are divided into those in the ZEUS hall and the tunnel. During a run, the clock signals are generated by the Readout Controller (ROC); these signals can be delayed by the Fast Fanout (FFO) board before traveling through the long cable to the shelter crates, adjacent to the LPS detector stations. The FCCD fans out the digital signals to the six Plane Interface (PLIF) boards, which buffer these signals prior to their arrival on the hybrid. After the GFLT trigger arrives, the readout sequence is performed by the SRC modules,

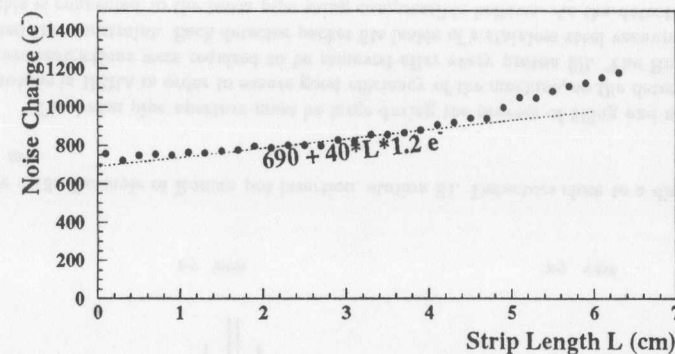


Figure 4.11: Detector noise, averaged over many channels with nearly the same strip length, vs. detector strip length. The line shows the prediction (obtained from simulation of the amplifier) of 690 electrons, plus 40 electrons per pF; ZEUS detectors have approximately 1.2 pF per cm.

buffered through the Readout Multiplexer (ROMUX). The SRC performs zero suppression before the VME formats the data for the ZEUS event builder.

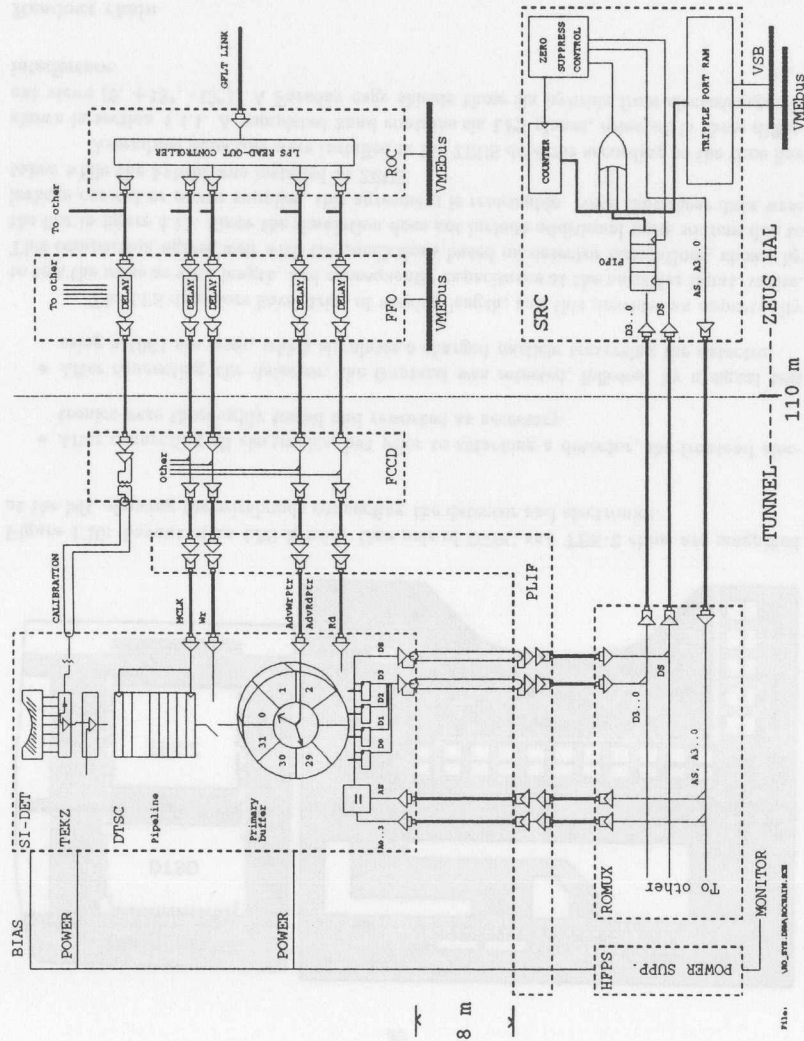


Figure 4.12: Schematic of LPS readout chain.

4.1.3 Mechanics for detector positioning

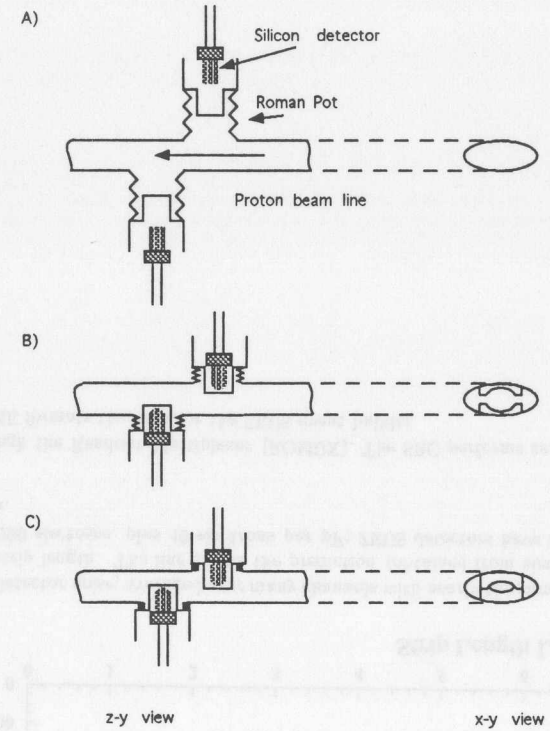


Figure 4.13: Example of Roman pot insertion, station S4. Detectors close to a distance of a few mm.

The beam pipe aperture must be large during the process of filling and accelerating protons in HERA in order to ensure good efficiency of the machine, so the detectors and aperture restrictions were required to be removed after every proton fill. The Roman pot satisfied this constraint. Each detector packet fits inside of a stainless steel vacuum barrier, and this is connected to the beam pipe using compressible bellows. As the detectors move into the beam pipe, the vacuum is displaced by the Roman pot and bellows. Figure 4.13 demonstrates Roman pot operations, for station S4 which has 2 pots for positioning detectors below and above the proton beam. With the detectors positioned inside, the pot compresses the bellows as it approaches the limit of the beam. For S4, S5, and S6, the detectors surround the proton beam and have some overlap once fully positioned.

Several constraints were placed on these mechanics. The detector positioning had to be precise to approximately the same as the silicon resolution of $20\mu\text{m}$. Detectors movement should extract the silicon 0.5 m from the proton beam during IIERA injection. Transverse, as well as longitudinal, motion is required to adapt to changing beam positions.

4.2 Operating conditions

The unique nature of the Roman pots of the LPS made data collection substantially more complex than for a fixed detector. In this section, details of detector operation are presented to demonstrate how these tasks were approached. Both the operation and maintenance of the silicon detectors and the process of positioning the detectors in the proton beam presented unique challenges.

4.2.1 Spectrometer components

For momentum determination, the final focus magnetics allow the LPS to function as a spectrometer. The beamline magnets operate analogous to optical elements with vertical and horizontal bends and focusing elements. These elements are shown in figure 4.14, with the names of the elements and apertures shown in table 4.1. The IIERA accelerator uses a long straight section using normal-conducting magnets. The problem of extracting the electron beam outside of the collision region provides two strong bending fields. First, the electron and proton beams are separated; next, the proton beam is elevated so that the proton and electron rings can be stacked through the ring. The two bending fields give two natural spectrometers, and consequently the S1-S3 set of detectors take advantage of the electron separation magnets, a horizontal bend from a 0.5 T field over 3 meters , and S4-S6 take advantage of the proton bending magnets, a vertical bend from a 1.3 T over 15 meters . The moderate fields of these magnets allow to relatively low momentum of $x_L \gtrsim 0.2 - 0.4$. Dipoles are shown with the prism shape in figure 4.14.

The quadrupole magnets add more fields, increasing acceptance and, in principle, improving momentum resolution, but requiring a more complex reconstruction. Quadrupoles act as lenses in the IIERA optics, focusing in x while defocusing in y (or the reverse). Quadrupoles for both the electron and proton final focus are included in the spectrometer, and considered in simulation and reconstruction, but only the proton magnets dominate the determination of proton trajectories.

Labels for the magnet elements are developed by IIERA and listed in table 4.1. For the aperture restrictions, the codes developed by the LPS group refer to: GC - circular gate, GR - rectangular gate, GA - rectangular gate with rounded corners, and GE - elliptical gate. Gates with *emphasis* are critical apertures for acceptance.

4.2.2 Operation of Roman pots

After IIERA has achieved stable running conditions, the detectors should be inserted into operating position at 10σ from the proton beam position. However, this process proved to be difficult, for a variety of reasons:

- Beyond $3-4\sigma$, the population of protons becomes highly non-Gaussian. These protons, generically called *beam halo* protons, varied in population by orders of magnitude

Index	Start z (m)	Length z (m)	Description	Object Code	Aperture Size (mm)
2	5.80	1.00	Electron Quadrupole	QL	44.4
4	7.10	0.76	Electron Quadrupole	QK	45.3
6	8.26	3×1.00	3 Electron Quadrupoles	QC	33.1
12	12.20	3×1.80	2 Electron Quadrupoles	QB	66.1
16	16.20	0.47	Aperture Gate	GC	29.0
17	16.67	3.36	Bend Magnet	BH	—
18	20.03	0.00	Aperture Gate	GC	28.6
20	20.03	0.38	Aperture Gate	GR	23.5
21	20.41	3.36	Bend Magnet	BH	—
22	23.77	0.17	Aperture Gate	GR	22.7
24	23.94	0.00	Pot 1	S1	—
26	23.94	0.48	Aperture Gate	GE	12.8
27	24.42	2.66	Bend Magnet	BS	17.5
29	27.63	4.00	Proton Quadrupole	QS	29.4
31	32.00	4.00	Proton Quadrupole	QS	30.2
33	36.38	4.00	Proton Quadrupole	QS	28.6
36	40.54	0.09	Aperture Gate	GC	30.4
38	40.62	0.15	Pot 2	S2	—
40	40.78	3.00	Proton Quadrupole	QR	29.6
42	43.90	0.00	Aperture Gate	GC	49.6
44	44.00	0.10	Pot 3	S3	—
46	44.10	0.10	Aperture Gate	GC	30.7
48	44.20	0.30	Bend Magnet	BZ	30.4
50	46.00	2.80	Bend Magnet	BT	30.0
51	48.80	0.00	Aperture Gate	GA	30.0
53	49.25	0.00	Aperture Gate	GA	30.0
58	56.95	3×3.00	3 Proton Quadrupole	QR	30.0
63	62.90	0.11	Pot 4, 5	S4	—
67	64.15	0.60	Bend Magnet	BY	39.0
69	65.33	4.17	Bend Magnet	BU	40.0
71	70.12	4.17	Bend Magnet	BU	40.0
73	74.91	4.17	Bend Magnet	BU	31.1
75	79.55	0.00	Aperture Gate	GC	38.4
77	81.17	0.00	Aperture Gate	GC	100.0
78	81.17	0.00	Pot 6, 7	S5	—
82	89.96	0.00	Aperture Gate	GO	—
83	89.96	0.10	Pot 8, 9	S6	—

Table 4.1: The beampipe elements in the spectrometer, including aperture limitations. Drift spaces have been omitted.

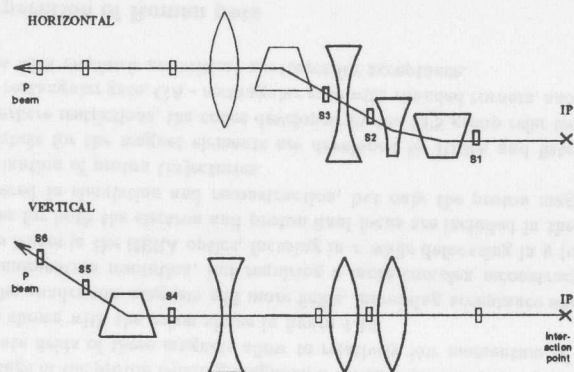


Figure 4.14: IIERA Optics in South-Left octant which provide the magnetic field for the LPS

between different fills and during the same fill.

- Neither the proton beam position nor the detector positions were calibrated on an absolute scale. The 10σ point could not be obtained based purely on measured detector positions.
- The shape of the proton beam changes, because the IIERA machine group periodically adjusts the optics. These changes made the custom shapes of the detectors slightly mismatched to the actual beam shapes.

Since the absolute positions of the detectors was not known, the movement of the detectors proceeded by slowly moving the LPS detectors while watching hit rates in the LPS and the Forward Neutron Calorimeter, just downstream of the LPS. Other rates were observed as well, especially the rates at the proton collimators operated by IIERA. Increases in these rates were used as evidence that the detectors were approaching the beam, and detector movement was stopped.

Of these problems, by far the most important was dealing with beam-halo protons, which caused three major problems. First, background rates would rise long before the detectors were close to normal operating positions. Second, halo protons which strike the LPS Roman pots could be perturbed only slightly, causing them to strike the beam pipe near the other experiments in IIERA. LPS operations were only possible as long as other experiments were not affected, so poor beam conditions (large halo rates) precluded LPS operations. Finally, halo protons were a background which had to be simulated (section 5.3.6) and removed (section 6.5).

Each proton fill had its own characteristics, and therefore the positioning of the detectors was a slow process in order to prevent backgrounds. Typical positioning of one detector took about 10 minutes, so the entire process would take approximately an hour, compared with 8-12 hours for a typical luminosity run. Improvements in the software

have since decreased the time spent checking background rates and automating detector movement.

By working with the IIERA machine group, some improvements in background conditions were obtained. The proton scrapers provided the most direct relief from beam halo protons: These collimators are positioned at 7σ from the beam center and should remove the proton halo completely. However, the automatic procedure for the scrapers would work similarly to the LPS positioning; moving the detectors until rate thresholds are exceeded, so in a fill with highly populated halos, the scrapers would often be positioned farther than 7σ . IIERA mitigated this problem by adjusting the automatic procedure, and by manually adjusting the scraper positions after the LPS ran into problems.

The operation of IIERA-B caused additional problems for the LPS. During test operations in 1995, the IIERA-B wires were observed to cause increases in LPS rates in proportion to the rates on the wires in IIERA-B. Apparently, protons which scatter through the IIERA-B wires would be much more likely to end up hitting the LPS. Considerable testing was performed, and changes made to the IIERA optics and IIERA-B wire positions substantially reduced interference after the 1996-97 shutdown.

In summary, the inconsistent nature of IIERA proton beams prevented LPS operations from becoming completely routine. Only after two years of effort working with IIERA and working on specialized positioning software could the continuous shifts by LPS operators be discontinued and responsibility given to the ZEUS shift crew.

4.2.3 Calibration and performance

Detector health was monitored by observing detector bias currents throughout operations, since bias currents are closely linked to radiation damage. Although many fluctuations were observed, most currents were reasonably stable. Many of the short-term fluctuations have been attributed to surface effects; these anneal out over a few hours or days [85].

The main checks of detector and readout functionality during routine operations were on the raw wiremaps (which act as a check of noise occupancy) and *matches* (which quickly check efficiency). Matches are determined by taking advantage of the redundant planes with identical orientations. For two such planes mounted adjacently, one would expect a charged particle to provide a signal in the same strip on both detectors. Consequently, the difference between the two hit strip numbers can be histogrammed, and a clear peak is observed.

Infrequent checks of detector operation include the calibration procedure using charge injection into the detector frontend, and efficiency determination using charged tracks. The latter procedure takes completed physics tracks (section 4.3.3) which pass track quality cuts and hit at least 15 active detectors, not including the detector being tested. Figure 4.15 shows the inefficiency determined for the LPS silicon planes. For many planes the inefficiency could not be determined, because no examples of inefficient behavior were observed; in this case, the upper limit for the inefficiency is presented. Efficiency for detectors in S6 was improved in 1995 by increasing the bias voltage from 45 to 70 volts. Plane 22 of S4 had poor efficiency due to large leakage current, which limited bias voltage to 15 volts.

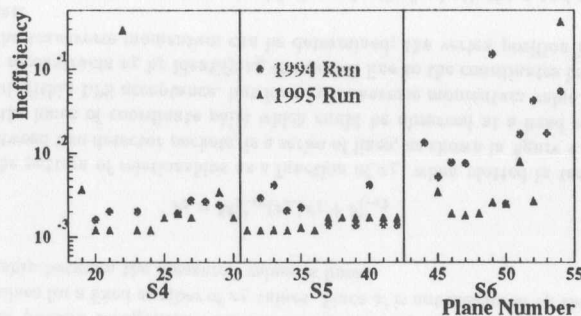


Figure 4.15: Efficiency values determined for 1994 and 1995 data. If no inefficiency was observed, the upper limit is shown.

4.3 Reconstruction software

LPS reconstruction software has the task of translating the raw data (series of silicon detector hits, motor positions, magnet currents) into physics variables (longitudinal and transverse momentum of charged particles). In general, any proton which hits 3 stations can be tracked without any additional constraints. However, tracks which hit only 2 stations can have reconstructed momenta if the vertex is known and used as a constraint; in this case, the five unknown parameters (x and y position at $z = 0$, x , y , and z momentum) are constrained by 6 parameters (x , y vertex, x and y coordinates in 2 stations). The reconstruction software should use all available information on hit detectors to reconstruct these parameters as accurately as possible.

The initial reconstruction software, LPRECON, failed at this task. LPRECON only attempted reconstruction for tracks hitting 3 stations, which are a small fraction of total acceptance. Furthermore, this code was poorly maintained. A complete rewrite of the reconstruction program, LP2RECON, has been used by all physics analyses of the LPS. The logic of LP2RECON is to first determine charged particle hit positions within individual pots, then match these within one station, and finally recognize the patterns of coordinates between stations to form tracks. These tracks are passed through a nonlinear fit routine to optimize the output parameters, and arbitration is done between all fitted tracks in the event to obtain independent tracks.

4.3.1 Coordinate reconstruction

Initially, the information of an LPS event is stored as a list of strips which have been hit in the detector. The first step is to remove from this list channels which are known to be faulty or have failures. Next, adjacent hit strips are combined to form *clusters*. Clusters are formed under the assumption that adjacent hits most likely are due to the same particle, possibly due to charge sharing. Average cluster width is 1.5 strips. The location of the cluster is taken as the center of the series of hit strips.

When two clusters on different detectors with the same view have a difference of less than 2 hit strips, these clusters are identified as belonging to a *match*. Matches are much more likely to correspond to charged particles than clusters, since the dominant noise source, synchrotron radiation, typically have uncorrelated signals, since an individual x-ray photon can be completely absorbed by the silicon.

For each detector packet, coordinates can be reconstructed using these lists of matches and clusters. A coordinate quality code has been developed for LPS detectors in order to distinguish charged particle coordinates (which should hit every plane in a given pot) from noise sources (which usually hit only two planes). Table 4.2 lists these quality values for the best case (3 matches "M") to the worst case (2 unmatched clusters "C"). The pattern recognition phase of coordinate reconstruction uses the design alignment to quickly match the hits between different planes. All possible combinations of the u , v , and x views are combined in an attempt to find an appropriate coordinate. These initial coordinates are then fit using the strip equations determined in the alignment (section 4.1), providing coordinates in the nominal proton beam reference frame.

Match and Cluster pattern	Number of hit detectors	Quality Code
M M M	6	1
M M C	5	2
M M	4	3
M C C	4	4
M C	3	5
C C C	3	6
C C	2	7

Table 4.2: Quality codes for LPS coordinates.

For S4-S6, which contain pairs of detector packets separated by a small distance in z , the coordinates from particles hitting both up and down detector packets are combined. This combination uses the full strip equation to make a local coordinate fit, including local tilt, and centers the coordinate in z between the two detector packets.

4.3.2 Pattern recognition

Pattern recognition in the presence of dipole and quadrupole fields takes advantage of the linearity of the optics as a function of transverse momentum and position, and the independence on x and y position. Writing the position and angle as a vector $(x, x') \equiv \mathbf{x}$, the propagation of a particle from position \mathbf{x}_1, z_1 to a later position \mathbf{x}_2, z_2 can be determined by the matrix

$$\mathbf{x}_2 = \mathbf{M}_{1 \rightarrow 2}(x_L)\mathbf{x}_1 + \mathbf{b}_{1 \rightarrow 2}(x_L) \quad (4.2)$$

Here, $\mathbf{M}_{1 \rightarrow 2}(x_L)$ is a 2×2 matrix, and $\mathbf{b}_{1 \rightarrow 2}(x_L)$ is a vector, and both are determined by the magnets and drift spaces between z_1 and z_2 and vary nonlinearly with momentum x_L .

As examples, three matrices are presented. For a drift between z_1 and z_2 , the appropriate matrix is

$$M_{1 \rightarrow 2} = \begin{pmatrix} 1 & z_{1 \rightarrow 2} \\ 0 & 1 \end{pmatrix}; \quad \mathbf{b}_{1 \rightarrow 2} = 0 \quad (4.3)$$

where $z_{1 \rightarrow 2}$ represents the difference in z position between the start and end of the drift. For a bending magnet which bends particles with momentum x_L by an angle α over a distance $z_{1 \rightarrow 2}$:

$$M_{1 \rightarrow 2} = \begin{pmatrix} 1 & z_{1 \rightarrow 2} \\ 0 & 1 \end{pmatrix}; \quad \mathbf{b}_{1 \rightarrow 2} = \begin{pmatrix} \frac{\alpha}{2} z_{1 \rightarrow 2} \\ \alpha \end{pmatrix} \quad (4.4)$$

Finally, the most complicated case is the quadrupole, with focusing length L , which can be written in terms of the parameter Ω :

$$\Omega \equiv \sqrt{\frac{z_{1 \rightarrow 2}}{|L|}}$$

$$M_{1 \rightarrow 2} = \begin{pmatrix} \cos \Omega & \frac{\sin \Omega}{\Omega} z_{1 \rightarrow 2} \\ -\frac{\Omega \sin \Omega}{z_{1 \rightarrow 2}} & \cos \Omega \end{pmatrix}; \quad \mathbf{b}_{1 \rightarrow 2} = 0 \quad (4.5)$$

and similarly, for defocusing quadrupoles:

$$M_{1 \rightarrow 2} = \begin{pmatrix} \cosh \Omega & \frac{\sinh \Omega}{\Omega} z_{1 \rightarrow 2} \\ -\frac{\sinh \Omega}{\Omega} z_{1 \rightarrow 2} & \cosh \Omega \end{pmatrix}; \quad \mathbf{b}_{1 \rightarrow 2} = 0 \quad (4.6)$$

Quadrupoles which are not centered on the proton beam act as the superposition of a bending magnet and an on-axis focusing magnet. IIERA uses these as a part of the electron extraction process with the proton beam intentionally set far from the quadrupole axis.

The pattern recognition uses this information by computing the $M_{1 \rightarrow 2}(x_L)$ and $\mathbf{b}_{1 \rightarrow 2}(x_L)$ values for a fixed number of x_L values. Since x' is not measured by these detectors, the relationship between the measured values is linear:

$$x_2 = M_{1 \rightarrow 2}^1(x_L) x_1 + b_{1 \rightarrow 2}^1 \quad (4.7)$$

The pattern of relationships as a function of x_L , when plotted in terms of the hit position between two detector packets, is a series of lines, as shown in figure 4.16. Each line represents the locus of coordinate pairs which could be observed at a fixed x_L and vertex position and within LPS acceptance, but for any transverse momentum value. The pattern recognition reconstructs x_L by identifying the closest line to the coordinates in two stations. With x_L , the transverse momentum can be determined; the vertex position is constrained to be a point.

In this method, x_L is determined independently for both the x and y coordinates. These values are combined by estimating the error in x_L from each view, and combining the two values appropriately.

This matching process only finds tracks which hit two detector packets. If more are hit, they are detected because their solutions have nearly the same x_L and p_T values and a coordinate is shared, and subsequently the x_L and p_T values are combined.

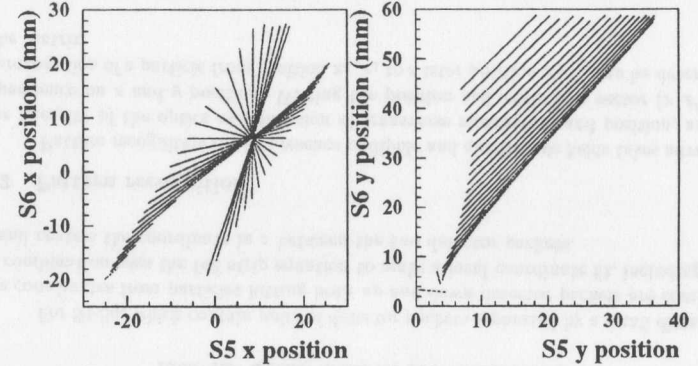


Figure 4.16: Correlations between S5 and S6 coordinate positions for x_L from 0.6 to 1.

4.3.3 Track fitting

The pattern recognition does an excellent job of extracting the track fit parameters. However, the combination of x_L and p_T values does not include correlations between the fit parameters, and is done independently for each pair of detectors with the vertex position is fixed to be a point. Ideally, the track parameters would be tuned to best satisfy all constraints (detector and vertex), and the vertex constraint would allow for variation of the track vertex with respect to the constraint vertex. Therefore, an additional step was added beyond the pattern recognition phase to better constrain the track parameters. This step uses an overall χ^2 fit, with minimization defined by:

$$\chi^2 \equiv \sum_{\text{clusters}} \frac{(x_i - X_i(v, p_T, x_L))^2}{\sigma_x^2} + \frac{(v_x - x_0)^2}{\sigma_x^2} + \frac{(v_y - y_0)^2}{\sigma_y^2} \quad (4.8)$$

where σ_x and σ_y are the nominal widths of the vertex, $v = (v_x, v_y, v_z)$ denotes the vertex position and p is the transverse momentum. X_i is the extrapolated position to the silicon detector. The LPS track fit routine minimizes this χ^2 using the method of Levenberg-Marquardt [91]. This produces the most probable values of the track parameters and an associated error matrix.

In addition to recomputing the physics parameters of each event, some additional parameters are returned by this fit routine: the number of missed detector planes N_{miss} and the distance of closest approach to the beam pipe d_{pipe} . Most of the LPS planes are better than 99% efficient. If a track is predicted to intersect an efficient plane far away from any dead channels and no hit is seen, this is strong evidence that the track is not real.

To find missed planes, each plane on or before the last pot on the track is checked to see if it has a hit on the track. If not, the track is extrapolated to the plane to see if the expected hit location falls at least 1mm inside the active area of the detector. If so, the ten closest strips to the extrapolated point are checked for either clusters (that may have been missed by the pattern recognition) or dead or suppressed strips. Failing this, the plane is

considered missing.

Because all of the tracks seen by the LPS that originate at $z = 0$ travel nearly parallel to the beam line, any track that touches the beampipe should traverse enough material to be lost. Tracks whose fitted trajectory traverses the beampipe in front of the pots which measure it are therefore suspect.

To test the trajectory of a track, the LPS reconstruction code contains a complete and detailed simulation of all beam elements between the LPS and interaction point, which are listed in Table 4.1. Each fitted track is swum through the beampipe, and the distance to the closest aperture along its path is calculated. This quantity is called the *distance of closest approach* or d_{pipe} . A negative value of d_{pipe} indicates that the trajectory of the track takes it through at least one beam element.

A detailed simulation of the beamline has further advantages. In addition to calculating the d_{pipe} , the fitted track is also checked to see how far it comes to missing the bottom and sides of each pot. This information can be used, in conjunction with the Monte Carlo, to estimate the LPS acceptance for any pot position. Tracks are also checked to see if they intersect a region of beampipe at 60 meters that is believed to contain a small obstruction of approximately 8.5 radiation lengths thickness. The actual obstruction has not been observed, but is suspected to be a part of the flange or beam position monitor in that area. Since this obstruction is large enough to effect the tracking resolution and efficiency and is not completely simulated in the Monte Carlo, the user has the option of simply throwing away the tracks that intersect it.

Data from the fitting process are stored in ADAMO [92] tables. Tables have been designed for the cluster, coordinate, and tracking information, with relations between the tables.

4.3.4 Track arbitration

Because of noise and background, or failure of the pattern recognition to appropriately combine 3-station tracks together, multiple tracks can appear in one event. The process of choosing the best or most appropriate tracks is handled by the arbitration part of LP2RECON. This is done in two parts: first, by defining a criteria for selecting the best tracks, and second, by removing all tracks in an event which are incompatible with the best track.

If there are many tracks in a single event, then the list of tracks is reduced by throwing out tracks with particularly bad parameters ($\chi^2/\text{dof} > 20$, $d_{\text{pipe}} < -0.05$ cm, $N_{\text{miss}} > 4$, or $r_L > 1.1$), but keeping at least 1 event in the list. From the remaining tracks, the one with the most silicon hits is selected, with χ^2 used to break ties.

Next, the software makes a list of all clusters which were used to form this track. Under the assumption that no two physics tracks will hit the same cluster, all tracks which were fitted using any cluster also used by a selected track is incompatible and is ignored. In fact, only 0.1% of events in the DIS sample have two tracks without any shared clusters, and 30% of those appear to be overlay of a beam-halo track with a physics track. Only about 0.01% of the events could be considered a viable two-track physics event when kinematical considerations are included. Since two-track events are so rare, arbitration is not strictly necessary, since simply selecting the best track in every event provides essentially an identical sample.

4.3.5 Reconstruction software for alignment

Small modifications to LP2RECON allowed this code to be used for the alignment process. Additional histograms were created, and reconstruction required two additions. In order to ensure efficient track finding during the steps before the vertex location was correctly located, a special 3-station track finding algorithm was used. This algorithm exploits the absence of any horizontal fields in S4-S6. All tracks traversing 3 stations must lie in a straight line in x , so collinear coordinates between S4-S6 are identified as tracks. These tracks would then be fit using LPPIT, which was modified to allow fits without constraint on the vertex location. Aspects of the alignment which utilize these features are referred to as *free-vertex fits*.

During normal operation of LP2RECON, the reconstruction operates using strip equations, which are read from the condition GAF (a GAF is a General ADAMO File, or a type of file which contains data formatted for the ADAMO database). For the 1994 alignment, these strip equations were overridden in LP2RECON and manually manipulated during the steps of the alignment. In 1995, the program MAKEGAF2 vastly improved the alignment process. By combining strip equation and GAF manipulation in one package, MAKEGAF2 required documentation of alignment steps, allowed easier changes in location of pots and stations, and removed the need for modifying LP2RECON code as alignment progressed. Additionally, the output of MAKEGAF2 could be directly installed in the ZEUS offline catalog. Future alignments should certainly make use of this software.

4.4 Alignment

The alignment process determines input parameters to the reconstruction program with which reconstructed tracks can be extracted. Without accurate knowledge of the positions of the detectors with respect to each other, the magnetic fields, and the proton beam, the reconstruction program will fail.

LPS data have been aligned separately in both 1994 and 1995 data taking periods. The LPS data needs to have the alignment procedure repeated compared to the 1994 alignment for a variety of reasons. The LPS hands are removed from the tunnel during shut-downs to prevent damage. Removing and installing these detectors can cause small shifts in the detector positions. Furthermore, some parameters in the alignment, in particular the location of the beam inside the beam pipe, are not necessarily stable with time and need to be determined independently for each year of data taking. In addition, having a completely independent alignment could help identify how misalignment impacts the physics distributions, if the physics distributions change between the two years.

This section presents the results of the 1995 alignment. The 1994 alignment followed a similar procedure and had similar resolutions, so presenting both would be redundant.

4.4.1 LPS configurations

In order to understand the context of LPS detector operation through its first 3 years of data taking, table 4.3 presents the history of all of the run periods in the condition database. "Physics Lumi" indicates the approximate luminosity (in nb^{-1}) which can be

analyzed for each run period; the starting date and event which triggered the separate condition GAF are presented as well.

Major losses of luminosity in 1994 were due to timing problems in the run range 9286-9600, and failure of the beam position monitor in run range 9927-10018. In 1995, the shaft connecting the motor of S4 to the resolver sheared, making precise positioning of this detector impossible. During the repair of this resolver, the S4 auxiliary limit switch was placed in the path of the compensation mechanism, which in turn confused the positioning software. Both problems affected the ability of S4 to take data, and since S4 is used in the trigger — which provided the large rate of elastic ρ^0 events crucial for aligning and data quality checks — data collected in these periods was labeled unusable for physics (runs 12212-12513). Failures in planes 3, 12, and 51 were due to identical failures in a component of the Plane Interface (PLIF).

Of remaining data losses in 1995, 50% were due to poor quality beams preventing LPS from taking data, 10% were due to the delay while waiting for IIERA to adjust the beam position, 28% were due to the time required to insert the LPS, 5% were due to other experiments requesting a delay, and 7% were due to time taken for tests of the LPS hardware.

Run Number	Start Date	Event at start of period which breaks condition	Stations Instrumented						Physics Lumi nb ⁻¹	
			S1	S2	S3	S4	S5	S6		
5000	1/1/93	First LPS Operations				X	X	X	*	0
8810	1/1/94	New Year, electrons				X	X	X	X	0
9286	1/1/94	Positrons; timing jumps; Down pots installed				X	X	X	X	48
9600	8/31/94	Timing problems fixed; Plane 49 recovered				X	X	X	X	587
9883	9/30/94	Plane 40 dies				X	X	X	X	91
10018	10/11/94	Position of S6 changed				X	X	X	X	178
10748	1/1/95	New year	X			X	X	X	X	455
12213	7/28/95	S4 Up Resolver Breaks	X			X	X	X	X	0
12395	8/7/95	Access: S2 installed, S4U repaired, S6 plane added	X	X		X	X	X	X	0
12471	8/16/95	S4 Up cannot move	X	X		X	X	X	X	0
12541	8/21/95	S4 Up repaired	X	X		X	X	X	X	920
13123	9/26/95	S2 cannot move	X			X	X	X	X	582
13291	10/2/95	S2 repaired	X	X		X	X	X	X	144
13329	10/9/95	ROC replaced	X	X		X	X	X	X	492
13663	10/26/95	Plane 3 fails	X	X		X	X	X	X	79
13731	10/29/95	Plane 12 fails	X	X		X	X	X	X	347
13817	11/4/95	Plane 51 fails	X	X		X	X	X	X	504

Table 4.3: Condition periods for 1994-1995 runs.

4.4.2 Data samples

Two physics sources were tapped to determine this alignment. 1995 data used an LPS trigger to obtain large rates of elastic $cp \rightarrow \rho^0 cp$ events. Photoproduction ρ^0 events, where the scattered electron is not observed, have two important properties. First, the proton has momentum fraction x_L very close to 1, since x_p is very small

$$\frac{M_p^2 + Q^2 - t}{ys} \simeq 1 - x_L \ll .001 \quad (4.9)$$

Second, the scattered proton will typically exactly balance the transverse momentum of the ρ^0 , an idea developed in [93]. This physics process is well understood [94]. In the 1995 run, approximately 7000 events were observed, including 1700 in S1-S2. The cuts applied were:

- CTD records two tracks
- Angular range of accepted tracks within $|\eta| < 2$
- For each CTD track, at least 20 hits for $0.59 < \theta < \pi/2$; 30 $\tan(\theta)$ hits for $\theta < 0.59$
- Invariant mass of 2 tracks was < 3.2
- All calorimeter cells, whose energy deposit could not be matched to a CTD tracks, were required to contain less than 200 MeV
- Total $E + p_z$ in the calorimeter was required to be less than 4 GeV

Note that the high rate of elastic ρ^0 was possible thanks to the improved LPS first level trigger. This high ρ^0 rate was crucial for the alignment process.

Some steps in the alignment require additional lower-momentum events. The limited acceptance of the trigger was observed to cause problems, for example by selecting tracks with substantially off-axis vertices for $x_L \simeq 0.9$. So that the sample would not have these acceptance effects, only DIS events were used to get the lower-momentum sample (this trigger sequence did not make selections based on the LPS trigger).

The frame of reference for this alignment is fixed to the nominal beam position in the quadrupoles and the center of the CTD, described as the “nominal beam reference frame.” This is different from the true proton beam reference frame, in which the physical proton beam lies along the $z = 0$ axis, since IIERA does not have to position the proton beam in the nominal position.

4.4.3 Alignment of isolated pots

The first step in this alignment procedure is determining how the planes were positioned with respect to each other within one detector packet. This can be achieved using the strip equation which relates the x and y coordinate with the number of the strip which was hit:

$$x = y \tan \phi_i - O_i - \frac{f_i p_i}{\cos \phi_i} N \quad (4.10)$$

Here, x and y are locations in the nominal proton beam reference frame, and the index i indicates the LPS plane number. The parameters relating strip number N to x and y include: the rotation angle of the strips ϕ_i , the pitch of the detector p_i , and f_i which is either +1 or -1 depending on detector orientation. The values of p_i , f_i , and ϕ_i are shown in table 4.4 for the LPS design, although small adjustments to ϕ_i are made during the alignment procedure. From locally fitted x and y coordinates, the residual was calculated by subtracting the right hand side of the strip equation from the left hand side. The two degrees of freedom in this alignment step for each plane are the offset O_i and a rotation which changes the strip angle ϕ_i .

Plane within pot	S1-S3		S4-S6 Up		S4-S6 down		Pitch p_i
	f_i	ϕ_i	f_i	ϕ_i	f_i	ϕ_i	
1	-1	0°	1	90°	-1	90°	115 μm
2,3	-1	45°	-1	-45°	1	-45°	81.3 μm
4,5	1	-45°	-1	45°	1	45°	81.3 μm
6	1	0°	-1	90°	1	90°	115 μm

Table 4.4: Nominal parameters which define LPS geometry for individual planes.

The offset was just taken as the mean value of the residual, while the rotation angle was determined by minimizing the width of the residual. Several iterations of shifts and rotations were necessary before convergence. The criteria for convergence was a residual mean value of less than 10 μm and a necessary change in the rotation angle for the next step width minimization of the order of 10^{-5} mrad.

4.4.4 Relative alignment of double-pot stations

For the stations S4-S6, the relative alignment of the up and down detector packets was determined by minimizing the residuals between coordinates which pass through both the up and down pots. The roll between the two stations is corrected at the same time. Most correlations of this sort result from $x_L = 1$ and consequently have a tilt in x of $\pm 0.5 \mu\text{rad}$ since these tracks converge at $z \simeq 140\text{m}$; this tilt is corrected over the 10-11 cm spacing in z between the up and down packets. Tilt in y is relatively small. Figure 4.17 shows the difference between up and down coordinates for all elastic ρ^0 events in the 1995 run, for the final alignment. Two corrections were applied which were time-dependent: S6 down was moved in order to insert a new detector plane on August 8, causing a small shift; a correction has been applied for this change. A drift in the relative position of S4 x over the year was corrected by applying two shifts on S4 Down of $-120 \mu\text{m}$ and $64 \mu\text{m}$ in the early and late parts of the run. No explanation is known for the drift in S4 Down, and S4 Down cannot definitively be identified as the pot which has drifted (it could also have been S4 Up); this identification of S4 Down as the unstable pot was based on the change in $\delta_{2,3}$ (equation 4.12).

In addition to an important step in the alignment, these distributions also demonstrate the resolution of position reconstruction, since the up and down positions are uncorrelated. By determining the difference between coordinates averaged over a long run and tracking this average over different runs, the mechanical stability can be estimated. Another method of estimating the stability is by attributing any increase in the width of the

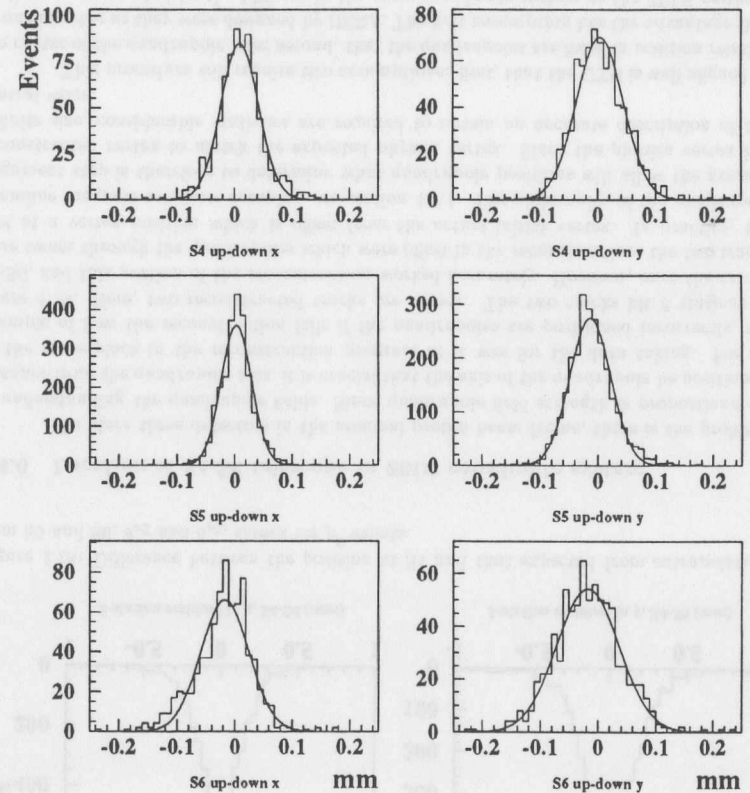


Figure 4.17: Difference between hits in up and down pots at stations S4-S6.

up-down distribution, above that expected from silicon detector resolution, to an unknown instability. These two evaluations usually give similar results; the two stability values are separated by dashes in table 4.5. S6 had especially poor resolution, and in general there is somewhat worse resolution in y than x .

Station	x width	y width	x stability	y stability
S4	32 μm	40 μm	25 μm	25-33 μm
S5	27 μm	35 μm	15-17 μm	17-27 μm
S6	42 μm	54 μm	22-33 μm	27-50 μm

Table 4.5: Mechanical stability of S4-S6, determined using elastic ρ^0 sample.

The difference between up and down pots' coordinates also determines whether there is a roll angle between the two detector packets.

4.4.5 Relative alignment of S4-S6 telescope

The remaining degrees of freedom for each entire station are translations in x and y . This makes a total of 4 degrees of freedom in each of 3 stations. Between S4 and S6 there is a set of strong dipole magnets which bend the proton beam by 5.7 mrad vertically. Thus, tracks which go through 3 stations form a simple spectrometer system which can be precisely aligned without constraint on the absolute x or y position, since no quadrupoles are involved. Relative alignment of the three stations in x is simple since there are no horizontal bends in this region, and a precision of about 5 μm is obtained. Tracks which pass from S4 to S6 should be collinear in x , so the "collinearity variables" δ_{x3} and δ_{y3} are used. In x , the position of a coordinate at S4 can be extrapolated from S5 and S6 coordinates using the formula:

$$x_4^c = \frac{x_5(z_6 - z_4) - x_6(z_5 - z_4)}{z_6 - z_5} \quad (4.11)$$

The difference between the extrapolated coordinate x_4^c and that observed at S4 x_4 is defined as δ_{x3} :

$$\delta_{x3} \equiv x_4 - x_4^c = x_4 - \frac{x_5(z_6 - z_4) - x_6(z_5 - z_4)}{z_6 - z_5} \quad (4.12)$$

For y , there is a bending magnet with substantial (5.7 mrad) angle; however, in the nominal proton beam reference frame, the coordinate system follows this bend for $x_L = 1$. Thus,

$$\delta_{y3} \equiv y_4 - \frac{y_5(z_6 - z_4) - y_6(z_5 - z_4)}{z_6 - z_5} \quad (4.13)$$

should be nearly 0 for any sample of $x_L = 1$ particles. The ρ^0 sample satisfies this criteria, and in figure 4.18, accurate alignment of the S4-S6 telescope is verified by the tight distributions of δ_{x3} and δ_{y3} .

This variable has been checked for any correlation between δ_{x3} and δ_{y3} , which would indicate a roll of the S4-S6 spectrometer.

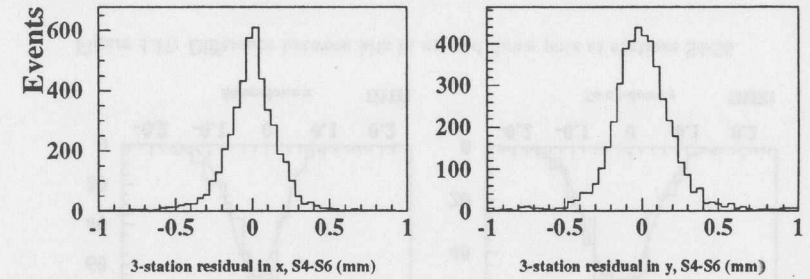


Figure 4.18: Difference between the position at S4 and that expected from extrapolation from S5 and S6, δ_{x3} and δ_{y3} , shown for ρ^0 events.

4.4.6 Location of S4-S6 telescope in ZEUS coordinate system

To place these detectors in the nominal proton beam frame, there is the problem of understanding the quadrupole fields. Since quadrupole field strength is proportional to distance from the quadrupole axis, it is crucial that the axis of the quadrupole be positioned at the same place in the reconstruction program as it was for the data taking. For an example of how the reconstruction fails if the quadrupoles are positioned incorrectly, see figure 4.19. Here, two reconstructed tracks are shown. The two tracks hit 3 stations in S4-S6, and this portion of the reconstruction worked accurately. However, once the tracks were swum through the quadrupoles which were offset in the reconstruction, the two tracks met at a vertex position which is offset from the actual initial vertex. In practice, the beamline magnets are more complex, see section 4.2.1. The philosophy of the quadrupole alignment step is therefore to determine what quadrupole positions will allow the average reconstructed vertex to match the expected physics vertex. Since the physics vertex has a finite size, considerable statistics are required to obtain an accurate description of the central value.

This procedure will require two assumptions: first, that the CTD is well aligned to the center of the quadrupole axis; second, that the quadrupoles are fixed in position relative to one another as they were designed by HIERA. The first assumption has the advantage that vertices reconstructed by the LPS are in the same coordinate system as the ZEUS vertices.

To implement this, 3-station tracks are reconstructed with free-vertex fits. These tracks are swum to $z = 0$. The S4-S6 telescope is translated in x and y , and allowed to pitch and yaw, in order to realize the goal that the reconstructed vertex location be independent of x_L and identical to the average CTD vertex for the same run period. A special fit procedure was developed for this task, which yielded a reasonable solution, shown in table 4.6. The fit minimizes the spot size by simultaneously adjusting the positions of S4-S6 (x and y offset, pitch, and yaw). An additional constraint was placed on the fit routine, requiring the expected S5-S6 correlation lines to pass through the points observed in a scatter plot of S5-S6 y positions. For reference, the covariance matrix is shown in table 4.7.

With this fit complete, the vertex position is shown as a function of x_L for the x and y views in figure 4.20. There is a small tendency for the vertex in x to be lower at small

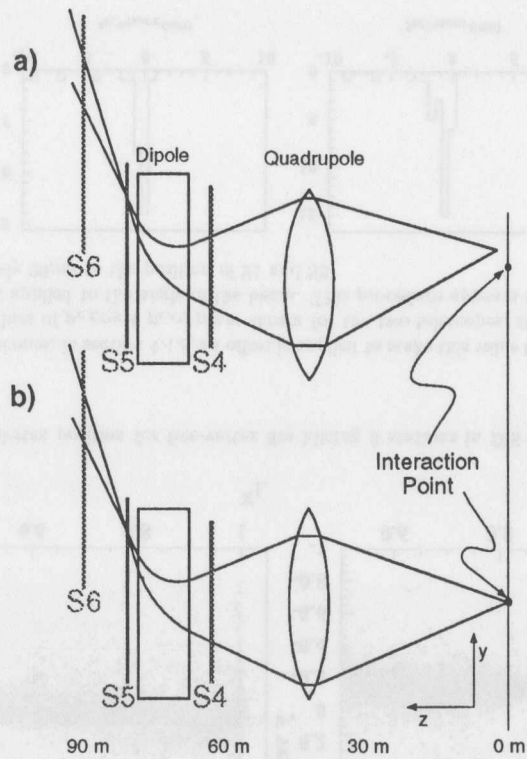


Figure 4.19: Example of how 3-station alignment can use the physics vertex distribution to extract information on the quadrupole focal length and transverse position. a) indicates poor quad position and focal length, which has been corrected in b)

QS field strength adjustment	1.0104 ± 0.0007	times nominal field
QR field strength adjustment	1.0045 ± 0.0007	times nominal field
Vertex X	1.17	mm (fixed)
Vertex Y	-1.24	mm (fixed)
Pot offset in x at S4	-0.05 ± 0.09	mm
Pot offset in y at S4	0.0 ± 0.003	mm
Pitch S4-S6 about S4	0.016 ± 0.032	mrاد
Yaw S4-S6 about S4	-0.0040 ± 0.0014	mrاد

Table 4.6: Results of quadrupole fits.

	QS Field	QR field	x offset	y offset	x rotation	y rotation
QS Field	1.00					
QR Field	0.26	1.00				
x offset	-0.07	-0.36	1.00			
y offset	-0.82	-0.11	0.05	1.00		
x rotation	0.07	0.47	-0.89	-0.02	1.00	
y rotation	-0.15	0.01	0.07	0.48	-0.02	1.00

Table 4.7: Covariance matrix for quadrupole fits.

x_L values, and when the vertex is constrained a larger χ^2 value results. The actual cause of this problem is unclear, but the effect on the reconstructed variables should be small.

4.4.7 Location of S1-S2 telescope

With the S4-S6 telescope aligned to the nominal proton beam reference frame, there are 2 degrees of freedom which need to be fixed for both S1 and S2, corresponding to the lateral positions of these two stations. Rolls of these 2 pots are not considered. There are 3 sources of information about these detector systems:

1. In one run (12855), S1 was placed far into the beam pipe, which provided a few overlap events which hit both S1 and part of the S4-S6 telescope.
2. Any source of $x_L = 1$ events can be used to identify the vertex location if x_L is fixed in the fit routine. This vertex can be required to match the vertex for the same run range in S4-S6.
3. p_T balance with elastic ρ^0 events defines the detector position for both detectors in x and y .

In order to maximize the resolution of these 3 information sources, the following method was used. First, the information from run 12855 was used to fix the position of S1 (figure 4.21). Next, the position of S2 was adjusted until the average vertex position for free-vertex ρ^0 events (with x_L constrained to 1) was identical between S1-S2 and S4-S6. Finally, the positions of S1 and S2 are adjusted simultaneously without changing the vertex position, until the average value of $p_{x,LPS} + p_{x,CTD}$ in elastic ρ^0 events is identical in both the S1-S2

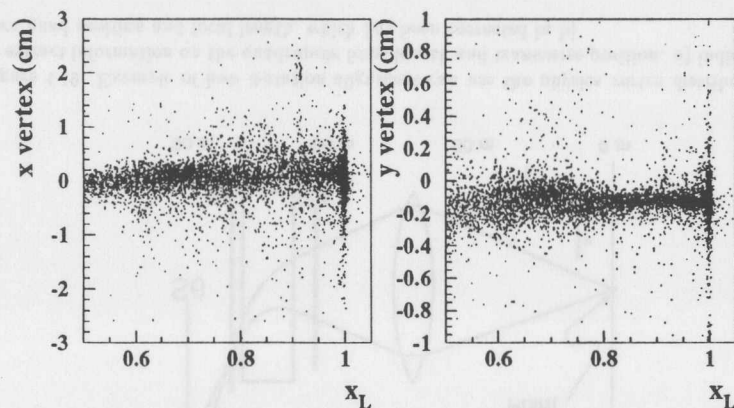


Figure 4.20: Vertex position for free-vertex fits hitting 3 stations in DIS sample, plotted against x_L

and S1-S6 telescopes; in section 4.4.8, an offset is applied to make this value 0. In figure 4.24, the average values of $p_{x,LPS} + p_{x,CTD}$ are shown for the two telescopes, after an identical offset has been applied to the angle of the beam. This procedure appears to give precision of approximately $20\mu\text{m}$ to the position of S1 and S2.

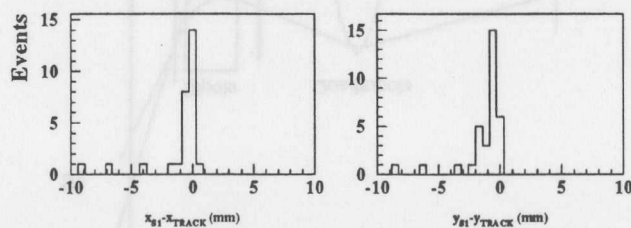


Figure 4.21: Difference between S1 coordinate and S4-S6 track extrapolated to S1, for run 12853

4.4.8 Location of beam

Previous parts of the alignment have addressed the procedure of locating detector position with respect to the nominal beam frame. The next step is to determine where the actual beam lies in this reference frame. Information about the beam position is used for two purposes by the reconstruction. The vertex position constrains the fit, allowing 2-station tracks to be fit. The angle of the track at the vertex is compared with the angle

of the proton beam to calculate transverse momentum. The 1995 run was divided into 42 run periods, each of which had about 300 elastic ρ^0 events tracked through S4-S6. Within each of these periods, the beam position was assumed to be constant.

At first it may seem redundant to determine the average vertex using the LPS, since in section 4.4.6 the vertex was fixed so as to be identical to the average vertex determined using central tracking. In fact, this step should determine changes in the average beam position over time, since HERA could have changed the interaction point location with respect to this average location over time. To check this, elastic ρ^0 events are fitted without vertex constraint, but with x_L fixed to 1, and the average value is looked at as a function of run number, as shown in figure 4.22. By looking at the vertex position over a short amount of time, vertex spot sizes of $(400, 150)\mu\text{m}$ for S1-S2 and $(1090, 180)\mu\text{m}$ for S4-S6 in (x, y) . The vertex spot sizes for S1-S2 are dominated by the actual spot size of the colliding beams.

In addition to showing the LPS average vertex as a function of time in figure 4.22, the parameterization of the CTD average vertex position is also shown with straight lines. In y , the two determinations of the vertex using the LPS agree on the movement of the beam, which is not confirmed by the CTD parameterization. Since S1-S2 and S4-S6 are completely independent in terms of their determination of shifts in vertex position, these shifts are likely to indicate actual movement of the interaction vertex. In x , all 3 measurements of the vertex position disagree, so no conclusion can be made as to which measurement (that of the CTD or LPS) best describes the true motion of the vertex. If the CTD parameterization were used to constrain the LPS vertex positions, the x_L resolution would be degraded.

These averages are included in the calibration GAF, and the reconstruction software uses these as constraints in the fit procedure. The vertices from S1-S2 were used when available, because S1-S2 is very sensitive to the constrained vertex location, while S4-S6 has much less dependence on the x vertex constraint, as evidenced by the errors shown in figure 4.22

Next, the tilt of the beam is determined. For each run period, the value of $p_{T(\rho)} + p_{T(\text{proton})}$ was averaged for the ρ^0 events to determine the beam tilt, shown in figure 4.23. The y tilt values were inconsistent with a fixed tilt for the entire run ($\chi^2/DOF = 5.4$ for fixed-tilt hypothesis), so the tilt has been set equal to the average in each run period. However, in x , the data are nearly constant with time ($\chi^2/DOF = 1.4$ for fixed-tilt hypothesis), so one universal tilt is applied to all runs.

The elastic ρ^0 give an estimation of the resolution of the spectrometer at $x_L = 1$, since the transverse and longitudinal momentum of the proton are known to high precision from the kinematics of the ρ determined in the ZEUS detector. The distributions of x_L , and sum of p_T for the ρ^0 and LPS tracks, are shown separately for S1-S2 and S4-S6 telescopes in figure 4.24. One of the main purposes of using the vertex constraints determined by using ρ^0 events, was to ensure that the $x_L = 1$ peak for ρ^0 events would be constant in time. This is approximately true, as shown in figure 4.25.

The x_L distribution for S4-S6 is fitted to the sum of two Gaussian distributions, which seem to describe the data well enough, and those results are shown in figure 4.24. Presumably the dual Gaussians were needed because of the variation in x_L resolution depending on the track phase space and combination of pots which were hit. Momentum resolution appears somewhat worse than for 1994, although transverse momentum resolution is essentially identical between the two years and between S1-S2 and S4-S6. S1-S2

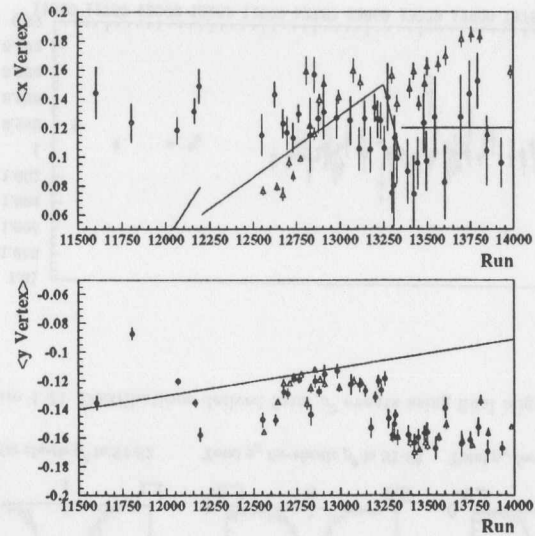


Figure 4.22: Average vertex as a function of the run number, for S1-S2 (open triangles) and S4-S6 (solid circles)

has longitudinal momentum resolution of about 2%, a factor of 6 worse than the S4-S6 telescope. A small correlation in the error in x_L and p_x is expected before the effects of beam emittance are considered; the p_x uncertainty in S1-S2 is about 20 MeV, compared with 40 MeV from the smearing of the proton beam.

Another item which should be monitored is the position of the $x_L = 1$ peak. Its mean position as a function of run number, derived from elastic ρ events, is shown in figure 4.25.

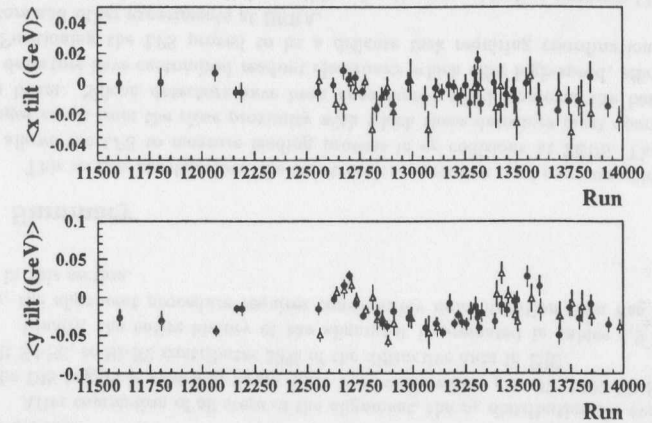


Figure 4.23: Beam Tilt as a function of the run number, for S1-S2 (open triangles) and S4-S6 (solid circles).

Fit	Number of Events	Mean	Sigma
x_L S4-S6	3281	$0.9999 \pm .0001$	$.00358 \pm .000117$
	2020	$0.9998 \pm .0003$	$.011 \pm .00034$
x tilt, S4-S6	4684	$.61 \pm .66 \text{ MeV}$	$42.6 \pm .7 \text{ MeV}$
y tilt, S4-S6	5203	$0 \pm 1.4 \text{ MeV}$	$97 \pm 1.3 \text{ MeV}$
x_L S1-S2	1707	$.999 \pm .001$	$.0190 \pm .0004$
x tilt, S1-S2	1594	$0 \pm 1.3 \text{ MeV}$	$47.2 \pm 1.3 \text{ MeV}$
y tilt, S1-S2	1720	$0 \pm 2.3 \text{ MeV}$	$94 \pm 2.1 \text{ MeV}$

Table 4.8: Fits to ρ^0 distributions, which estimate resolution of physics variables near $x_L = 1$.

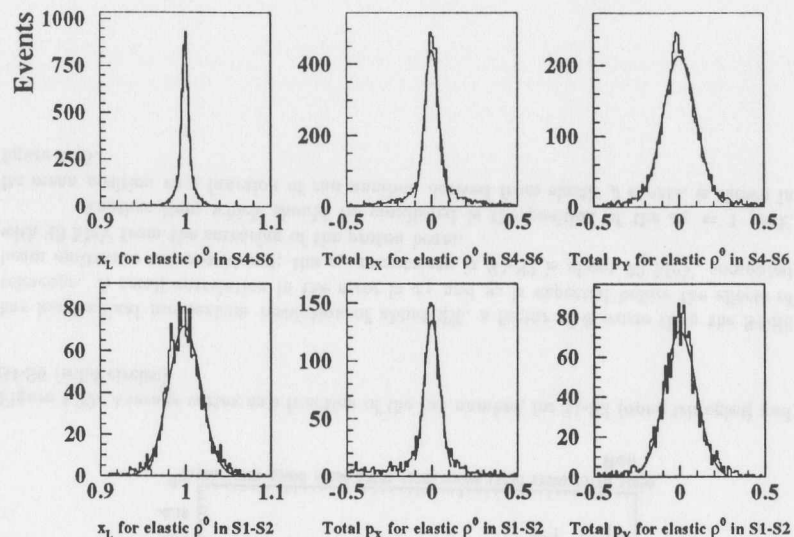


Figure 4.24: Distributions derived from ρ^0 events using final alignment.

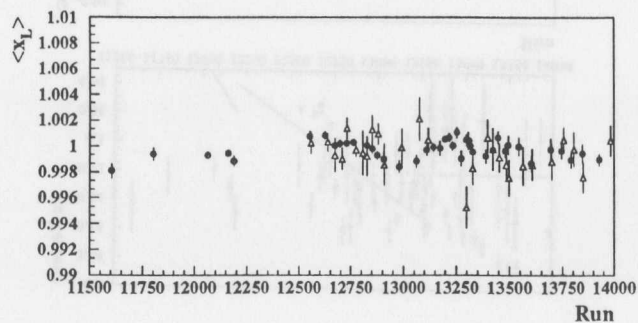


Figure 4.25: Position of kinematic peak versus run number, for S1-S2 (open triangles) and S4-S6 (solid circles).

4.4.9 Determination of beam apertures

The key to accurate LPS acceptance is knowing the locations and sizes of the beam apertures. These have been carefully simulated in MOZART (section 5.1), but a few simulated apertures did not match IIERA drawings. Release NUM12V7 contains a number of changes to the apertures applicable for S4-S6, making it suitable for acceptance correction of these tracks. Positions of these elements were carefully checked by plotting where tracks lie in slices of z , providing clear outlines of these beam elements. Four examples of these plots are shown in figure 4.26. The lines indicate the edges of the apertures or detectors, and the points are extrapolations of tracks from the DIS sample. These four locations are critical aperture restrictions, the first two limiting S1-S2 acceptance, and the second two limiting S4-S6 acceptance. The positions of these four apertures have been adjusted in MOZART by up to 2 mm to ensure that the acceptance in the Monte Carlo matches the data. The lines indicate the positions of these apertures as simulated in MOZART, and clearly are effective in demonstrating the limit of LPS acceptance. These four regions are *emphasized* in the list of aperture restrictions in table 4.1.

The alignment procedure does not enforce any requirement that the apertures remain fixed between two years of data taking. In particular, the quadrupole fit procedure could have given a substantially different result from the 1994 alignment. Fortunately, the results for 1994 and 1995 seem to be quite similar, with the shift predicted at 60 m differing by only 0.6 mm.

After completion of all steps of the alignment, the x_L distribution for events satisfying the DIS trigger is shown in figure 4.27. For events with $x_L > .97$, 1427 hit S1-S2 and 3412 hit S4-S6, so S1-S2 contributes 30% of the diffractive data in DIS.

Finally, the entire history of the alignment is presented in tables 4.9 and 4.10. Clearly, the alignment procedure requires considerably more iteration than has been presented in this section.

4.5 Summary

This section has described the construction, operation, and reconstruction process which allows the LPS to measure leading protons in cp collisions at ZEUS. The primary challenges result from the close proximity with which these detectors must operate to the proton beam. Silicon detectors have been constructed which conform the beam shape. These detectors have customized readout electronics which offer high-speed, efficient readout. Positioning the LPS proved to be a delicate task requiring coordination with the operators and other experiments at IIERA.

Analysis of proton tracks is possible using the reconstruction program LP2RECON. By applying a number of clever algorithms, the reconstructed momenta of the final proton can be determined with considerable accuracy. A precise alignment is required for the reconstruction to be successful. Careful analysis of physics tracks reveals the locations of all detectors to sufficient precision for physics analysis to proceed.

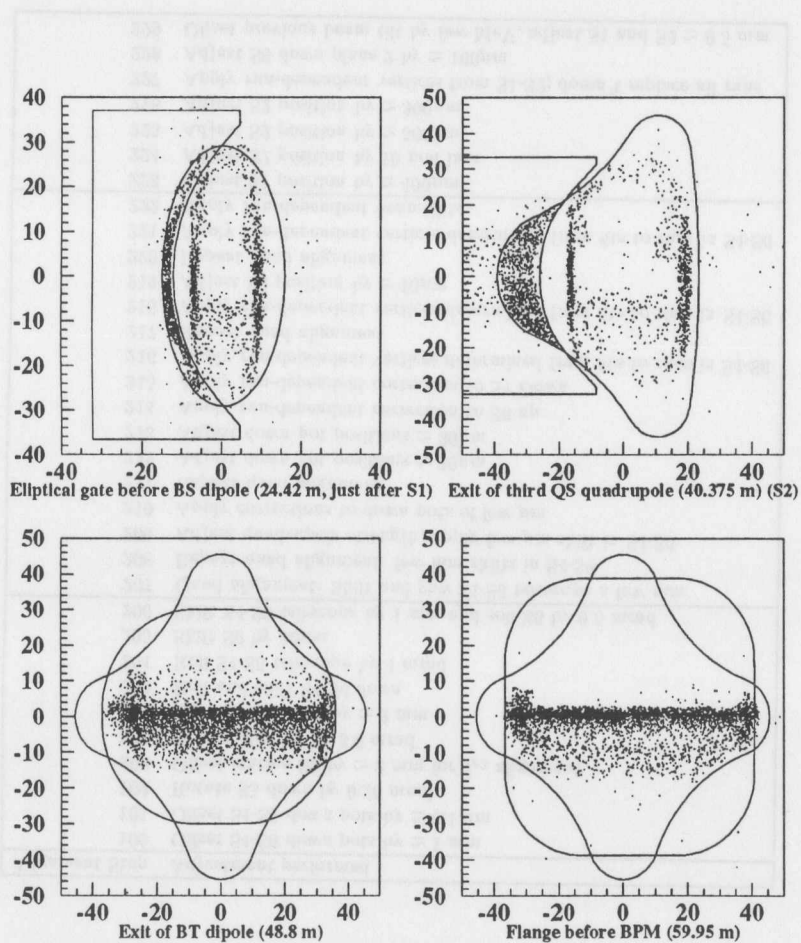


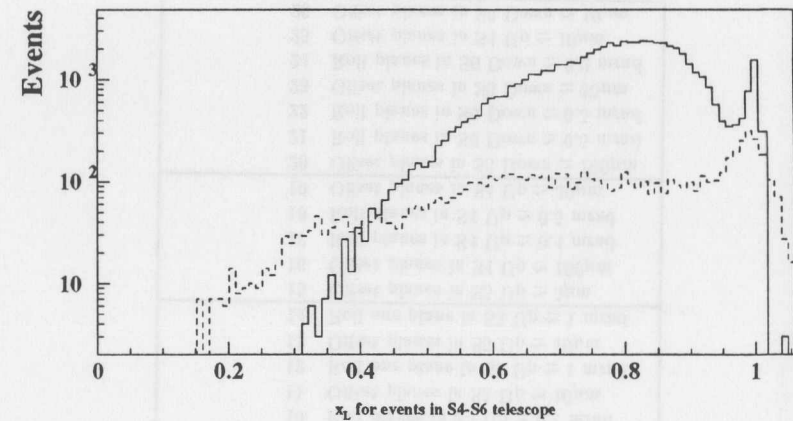
Figure 4.26: Scatter plots of x vs. y position for tracks in DIS sample, plotted at fixed z positions. The tracks locations are used to identify the boundaries of apertures and detectors.

Alignment Step	Adjustment performed
2	Offset planes in S5 Up $\approx 100 \mu\text{m}$
3	Offset plane in S5 Down
4	Roll planes in S5 Down $\approx 0.6 \text{ mrad}$
5	Offset planes in S5 Down $\approx 10 \mu\text{m}$
6	Roll planes in S5 Down $\approx 0.1 \text{ mrad}$
7	Offset planes in S5 Down $\approx 10 \mu\text{m}$
8	Roll planes in S5 Up $\approx 0.5 \text{ mrad}$
9	Offset planes in S5 Up $\approx 20 \mu\text{m}$
10	Roll planes in S5 Up $\approx 0.1 \text{ mrad}$
11	Offset planes in S5 Up $\approx 10 \mu\text{m}$
12	Roll one plane in S5 Up $\approx 1 \text{ mrad}$
13	Offset planes in S5 Up $\approx 10 \mu\text{m}$
14	Roll one plane in S5 Up $\approx 1 \text{ mrad}$
15	Offset planes in S5 Up $\approx 5 \mu\text{m}$
16	Offset planes in S4 Up $\approx 100 \mu\text{m}$
17	Roll planes in S4 Up $\approx 0.4 \text{ mrad}$
18	Roll planes in S4 Up $\approx 0.5 \text{ mrad}$
19	Offset planes in S4 Up $\approx 30 \mu\text{m}$
20	Offset planes in S6 Down $\approx 100 \mu\text{m}$
21	Roll planes in S6 Down $\approx 0.5 \text{ mrad}$
22	Roll planes in S6 Down $\approx 0.5 \text{ mrad}$
23	Offset planes in S6 Down $\approx 30 \mu\text{m}$
24	Roll planes in S6 Down $\approx 0.2 \text{ mrad}$
25	Offset planes in S4 Up $\approx 10 \mu\text{m}$
26	Offset planes in S6 Down $\approx 10 \mu\text{m}$
27	Offset planes in S1 and S2 $\approx 100 \mu\text{m}$
29	Roll planes in S1 and S2 $\approx 0.5 \text{ mrad}$
30	Offset planes in S1 and S2 $\approx 10 \mu\text{m}$
31	Roll planes in S1 and S2 $\approx 0.3 \text{ mrad}$
32	Offset planes in S6 Up $\approx 60 \mu\text{m}$
33	Roll planes in S6 Up $\approx 0.9 \text{ mrad}$
34	Offset planes in S6 Up $\approx 50 \mu\text{m}$
35	Roll planes in S6 Up $\approx 0.2 \text{ mrad}$
36	Offset planes in S6 Up $\approx 5 \mu\text{m}$
37	Offset planes in S4 Down $\approx 60 \mu\text{m}$
38	Roll planes in S4 Down $\approx 0.7 \text{ mrad}$
39	Offset planes in S4 Down $\approx 10 \mu\text{m}$
40	Offset all planes a few μm
41	Rotate all planes a few mrad
42	Offset all planes a few μm

Table 4.9: Steps to align planes within detector packets.

Alignment Step	Adjustment performed
100	Offset S4-S6 down pots by $\simeq 1$ mm
101	Offset S4-S6 down pots by $\simeq 0.1$ mm
102	Rotate S5 down by 0.26 mrad
200	Offset station S6 by $\simeq 2$ mm for δ_{x3} alignment
201	Roll station S6 by 3.6 mrad
202	Shift S4-S6 down by $\simeq 3$ mm
203	Roll and shift S4-S6 down
204	Roll S4-S6 telescope by 4 mrad
205	Shift S6 by $30\mu\text{m}$
206	Shift S4-S6 telescope by 1 mm and roll S6 by 0.5 mrad
207	Quad alignment: Shift and yaw S4-S6 telescope a few mm
208	Repeat quad alignment: few mm shifts in S4-S6
209	Adjust quadrupole strength, apply few μm shift in S4-S6
210	Apply corrections to down pots of few μm
211	Repeat quad alignment
212	Adjust down pot positions $\simeq 30\mu\text{m}$
213	Adjust down pot positions $\simeq 30\mu\text{m}$
214	Apply run-dependent correction to S6 up
215	Apply run-dependent correction to S4 Down
216	Apply run-dependent vertices determined from fits to rhos in S4-S6
217	Repeat quad alignment
218	Apply run-dependent vertices determined from fits to rhos in S4-S6
219	Adjust S6 position by $\simeq 10\mu\text{m}$
220	Repeat quad alignment
221	Apply run-dependent vertices determined from fits to rhos in S4-S6
222	Apply run-dependent beam tilts
223	Adjust S1 position by $\simeq 400\mu\text{m}$
224	Adjust S2 position by 10 mm in x
225	Adjust S2 position by $\simeq 500\mu\text{m}$
226	Adjust S2 position by $\simeq 300\mu\text{m}$
227	Apply run-dependent vertices from S1-S2; doesn't replace all runs
228	Adjust S6 down plane 2 by $\simeq 100\mu\text{m}$
229	Offset previous beam tilt by few MeV, adjust S1 and S2 $\simeq 0.5$ mm

Table 4.10: Steps to locate pots

Figure 4.27: x_L distribution for DIS events, for S4-S6 (solid) and S1-S2 (dashed).

Chapter 5

Monte Carlo Simulation

Modern high-energy physics has grown to depend on detailed simulation of both particle-level processes and the detector response for making physics measurements. Because these simulations depend on random processes, both at the physics level and at detector level of simulation, they are termed *Monte Carlo*. These simulations provide information required to interpret measurements.

- Accurate simulation provides confirmation that detector operation is well understood. If all observable parameters have similar distributions in data and Monte Carlo, major problems in the detector are unlikely to have occurred.
- Resolution of detector for reconstructing physics variables can be calculated. For example, the resolution of Q^2 can be determined by comparing the virtual photon Q^2 from the physics simulation with the value reconstructed by the simulated detector.
- Acceptance of the detector can be determined from these simulations. For example, the LPS event sample only contains those protons which have hit at least 2 active detectors, which for the diffractive DIS sample is only a few percent of the events. Understanding the physics rate requires understanding of what fraction of the events actually hit the detector.
- Monte Carlo provides a consistent method for including understood physics processes. For example, the QED corrections to the cp interaction can be removed if the Monte Carlo includes these processes.
- Complex, poorly understood physics processes can be simulated. For example, fragmentation processes cannot be predicted, but Monte Carlo models have been written to approximate experimental observations. Selecting different Monte Carlo models allows the effects of fragmentation (on resolution, acceptance, etc.) to be tested, allowing better understanding of the systematic error.
- By comparing observed distributions generated by different models, the most appropriate model can be selected, or parameters in a model can be tuned.
- In order to allow comparisons between different experiments, the effects of acceptance and resolution can be removed from a data set using the process of *unfolding*. Generally, the unfolding process has a cross section as the final result.

- Monte Carlo provides a wealth of information about systematic uncertainties in the detector or measurement. For example, if the calorimeter calibration has accuracy of 1%, then Monte Carlo simulations can determine the effect of that 1% uncertainty on measurements.

The Monte Carlo process starts by the simulation of the collision of the electron and proton. A *generator* is responsible for accurately predicting the particular reaction of interest. For each collision, the generator returns a list of particles for the final state of that event. A variety of generators have been used in this analysis, as described in section 5.3.1–5.3.4. These particles are then given to the simulation program for the detector, described in sections 5.1 and 5.2.

While the Monte Carlo method has many advantages, measurements which depend on Monte Carlo simulation can be incorrect. Because the programs are so complex, errors can easily occur. Therefore, any opportunity to make a measurement which does not require Monte Carlo corrections should be exploited, as in sections 7.2, 7.3, 7.5, and section 9.1. When Monte Carlo corrections are applied extra cross-checks are required, as has been performed in sections 7.4, 8.3 and 9.3.

5.1 ZEUS Monte Carlo system

At ZEUS, the program MOZART simulates the passage of particles through the detector, including particle decay, interactions with materials in the detector, and detector response to particles. This package, one of the largest programs used at ZEUS, relies heavily on the CERN simulation GEANT [95]. Detector response is simulated with a variety of specialized codes [96]. Once the detector response has been simulated, ZGANA simulates the trigger system, and the event is reconstructed using the same code as standard physics events.

5.2 LPS GEANT implementation

In their Monte Carlo code, most ZEUS subsystems have the task of maintaining in GEANT the geometry of their detectors. The LPS has the additional burden of maintaining the geometry of 85 meters of the HERA beam line, including 23 magnets with accessories. Developed over a span of five years [97, 98], the LPS GEANT simulation includes updates based on observations from the 1994 data.

This section details the simulation of the beamline, magnetic fields, and detector response (digitization). Additionally, some limitations of GEANT required some additional work to include the effects of the moving detectors in the LPS. In the simulation, the detector positions are fixed, leading to a problem of changing acceptance in the data, which is considered in section 5.2.6, and also to loss of precision with which coordinates are measured, since the detector positions can only be determined to the precision of the mechanics.

5.2.1 HERA apertures

Typical magnets are simulated as a box or cylinder made out of magnet material containing a volume of air to define the inside dimensions. For quadrupole magnets where

the inside dimensions are more complicated, four 90° slices of cylinders of magnet material are used instead. A beampipe, made out of iron and containing vacuum, is placed inside in the inner dimension.

Whereas magnets are only approximately simulated, more attention has been placed on the exact shape of the beampipe because of its influence on acceptance. Except for small approximations, all beampipe inner dimensions match blueprint specifications (listed in table 4.1). Every attempt has been made to reproduce the critical apertures exactly (see figure 4.26 for examples of some of the beampipe shapes), although some of the less crucial apertures are approximations, including the elliptical shape of BS. The positions were verified or slightly relocated based on the patterns in the data, as described in section 4.4.9.

The unusual shape of active silicon was difficult to implement in GEANT, and required overlapping trapezoidal and elliptical volumes [97]. The resulting simulation matches the actual detector shapes. A GEANT drawing of hand S4 up is shown in figure 5.1; other hands are similar.

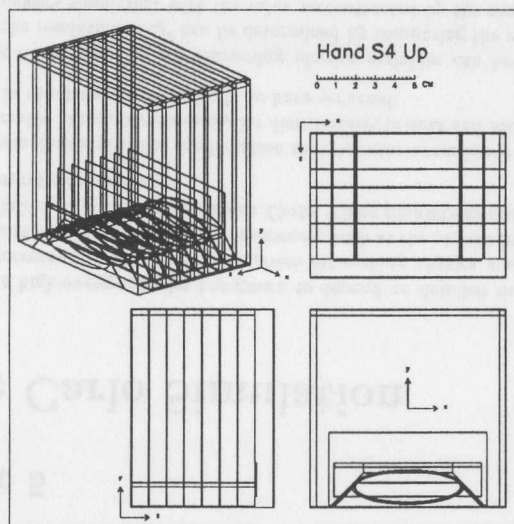


Figure 5.1: Implementation of hand S4 in GEANT.

5.2.2 Magnetic field

Since the HERA magnets are expected to produce nearly ideal dipole and quadrupole fields inside their beampipes, this is simulated in GEANT. Accurate strengths of the dipole and quadrupole fields have been obtained with the help of HERA personnel, and are also included in the reconstruction and the stand-alone ray-tracing program BEAM9.

5.2.3 Digitization

Since LPS silicon detectors employ the binary readout scheme, simulating their response is relatively simple. To first order, LPS channels respond only when charged particles pass through them, and digitization indicates which strips. Inefficiency, noise, cluster size, and dead channels extend this simplistic model to realistically simulate the detectors.

Each charged particle hit is randomly tested using the efficiency values determined from physics tracks (figure 4.15). Correlations with incident angle and track energy are ignored.

Noise is simulated by randomly generating for each plane in each event n noise hits according to a Poisson distribution. Typically 0.2 hits/event/plane are simulated in each event, based on information from random triggers. Each hit is placed onto a random spot on the surface of the active detector, matched with the closest strip, and added to the raw data as noise. This produces noise in proportion to a strip's area, expected for synchrotron radiation, which dominates the noise occupancy. This approximation would need to be reviewed if the electronics noise dominated the noise occupancy.

The simulation assumes that all detector strips between the particle entrance and exit points are hit. A small addition to this range is added to simulate charge sharing. The simulation of the suppression of dead and noisy channels is performed in the reconstruction program. In a treatment similar to actual data, the reconstruction reads the dead and noisy channel list from the Monte Carlo database and removes the specified hits from the simulated raw data.

5.2.4 Beam simulation

The LPS reconstruction uses the beam position for constraining vertex position and for measuring transverse momentum with respect to beam angle (section 4.4.8). If the beam is traveling at an angle through ZEUS, this produces an absolute p_T offset in the LPS. The proton beam emittance, which smears the transverse momentum of individual protons in the beam, is an effect large enough to dominate the p_T resolution of the LPS. Therefore, the accurate simulation of the vertex position, vertex size, proton beam tilt, and proton beam emittance is essential for an accurate simulation of the LPS.

To this end, MOZART was modified with routines to reproduce, to the best of our knowledge, these beam related effects. These include the addition of Gaussian smearing in the x and y vertex positions and a routine to boost and rotate the entire event in order to account for proton beam tilt. The parameters used by the beam simulation are:

- A vertex position of $x = 0.139$ cm and $y = -0.129$ cm for the positron running in 1994.
- A vertex Gaussian width of $\delta x = 0.033$ cm and $\delta y = 0.009$ cm.
- A proton beam tilt of $p_x = -16$ MeV and $p_y = -109$ MeV (for 820 GeV protons).
- A emittance of Gaussian width $\delta p_x = 40$ MeV and $\delta p_y = 90$ MeV

5.2.5 LPS resolution with moving detectors

Since the LPS depends on mechanical resolvers to determine the position of the detectors each run, the precision of the mechanics limits coordinate accuracy. This precision is the same magnitude as the silicon detector resolution, and consequently degrades resolution in x_L and p_T . The resolution of p_T is irrelevant since the precision of the detector, less than 10 MeV, is small enough compared to the beam spread (100 MeV) that measurements are insensitive to any loss of precision in p_T ; therefore, I concentrate on x_L resolution.

In order to include the effects of small mismeasurements of the detector positions, the detectors are randomly shifted by 10–20 μm according to values determined from the data, table 4.5. Checks using ρ^0 data, where the physics distribution is effectively a δ -function at $x_L = 1$, indicate that even with this smearing the Monte Carlo distribution is slightly better than the data distribution. The smeared Monte Carlo is brought into agreement with the data by smearing x_L by $\sigma = 0.0017$.

The error value for x_L is determined from the covariance matrix from LP2FIT. However, Monte Carlo studies have shown that the actual uncertainty in x_L can be obtained by scaling the value from the covariance matrix by 1.6. Inadequacies of the linear error approximation result in the slight underestimation of the error value returned by LP2FIT.

Finally, the decreased precision of the data causes the χ^2 values to be larger. Scaling the χ^2 values by 1.4 in the Monte Carlo produces excellent agreement. This value is not particularly important, except that a cut is made in χ^2 and it would be good to have roughly the same amount of tail removed in the data as Monte Carlo. By placing this cut far from the peak, the measurement will be less sensitive to the cut in this value. Figure 5.8 includes a comparison of the data χ^2 values and the scaled MC values.

5.2.6 Accounting for changes in run conditions

Due to varying run conditions, the LPS had to be positioned at different locations for each run in the data. The Monte Carlo, due to the inflexibility of GEANT, had to be generated with fixed geometry. To reconcile these different acceptance conditions, Monte Carlo events are reweighted. For each generated event in which there is an LPS track, a ray-tracing Monte Carlo is executed which tests whether that track would have been observed under run conditions different from those in MOZART.

The weight is calculated using two different methods. The first method executes the ray-tracing Monte Carlo for each run configuration, and tests whether a proton with the same p_x , p_y , x_L and vertex would hit at least 2 stations. This weight is almost always one, unless the track is passing close to the edge of the detector. The second method works like the first, except that the vertex and track angle are modified to take into account the changes in average vertex and beam tilt for each run. The second method is more reliable, since movements of the beam influenced the decisions on how to move the detectors. When correcting Monte Carlo for simulation of 1995 data, only the second method is applied due to the considerable changes in beam position and tilt.

Figure 5.2 shows the detector S4 Up, with a small corner enlarged to demonstrate this reweighting scheme. A hypothetical track which is assumed to hit well within the active region of S5 is shown near the edge of detector S4. Two different detector positions are shown by the two diagonal lines on the expanded view. The Monte Carlo was generated using the

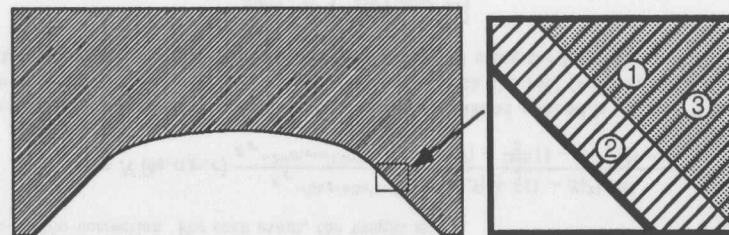


Figure 5.2: Example of conditions where weights are required to correct for run-to-run changes.

lower detector position. Four scenarios are presented in which the Monte Carlo could have incorrectly estimated the acceptance by not including changes in the run conditions.

- 1a. The detector was positioned at the lower line and the hit position is identified by 1. The Monte Carlo and data have identical acceptance, and the event was accepted in both data and Monte Carlo.
- 1b. In this run, the detector was positioned at the higher line, causing the hit to be observed closer to the edge of the detector. The event is observed in both data and Monte Carlo, but is removed from the data because it passes too close to the edge of the detector.
2. The detector was positioned at the lower line, but the beam moved, causing the track with the same generated p_x and p_y to hit the detector at 2. The event was again removed from the data.
3. Finally, beam movement sent the track to 3. The track is observed in both data and Monte Carlo, but was removed from the data sample because it passed too closely to the beam pipe edge.

In this case, the applied weight would be the luminosity for the first run configuration divided by the total luminosity of all four run configurations.

Since only weights less than 1 can be applied with this method, the Monte Carlo geometry must have more acceptance than all run configurations. To ensure this, the MOZART configuration was chosen to be the same as a run in which the detectors were unusually close to the beam, and therefore had high acceptance. Furthermore, in the data, events are cut if the track passes too close to the beam pipe (d_{pipe} cut) or to close to the edge of the detector (d_{det} cut). These cuts are not made directly in the Monte Carlo events; instead, the cuts are applied to the ray-traced tracks during the reweighting process.

The average value of the weight applied as a function of x_L and p_T are shown in figure 5.3. For the diffractive analysis, the net result is to reduce the overall acceptance by 19%, with little x_p or t dependence in the 1994 configuration for events within the diffractive cut of $x_L > .97$.

A simple comparison with the method of [99] demonstrates that for diffractive events, both methods are approximately consistent with a fixed decrease in acceptance [100].

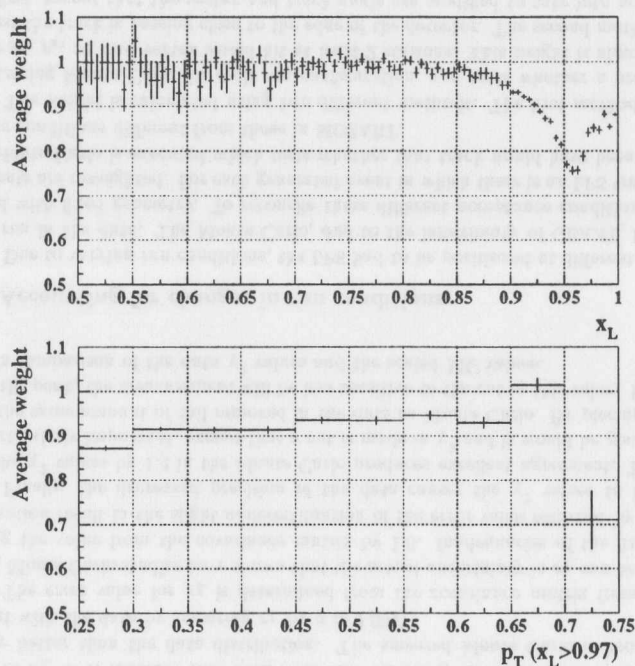


Figure 5.3: Weights applied to account for run-to-run changes in detector and beam positions, for 1994 data set.

5.3 Monte Carlo event generators

Successful simulation of the complex particle physics events starts with the Monte Carlo generator. First, the generator randomly selects the kinematic variables based on the cross sections of the physics process. These kinematic variables are checked for consistency, and then the final particle momenta are determined. Often the final particles are quarks, in which case a fragmentation Monte Carlo is required to evolve the high-energy quark system into a large number of final hadrons. Many events are generated in order to have several times the simulated luminosity compared with the observed luminosity.

5.3.1 RAPGAP single diffractive DIS

RAPGAP is a generator for $ep \rightarrow epX$ events [101] and includes radiative corrections. A sample of 450K events have been generated using a structure function similar to that measured by ZEUS. In fact, the β -dependence is identical to that measured by ZEUS; the ‘‘Pomeron flux’’ was based on the work of Stremg [102]:

$$F_2^{D(4)} = \frac{\beta_F^2(0)}{16\pi} x_F^{1-2\alpha_F-2\alpha't} e^{b_0 t} \left[\beta(1-\beta) + \frac{c}{2}(1-\beta)^2 \right] \quad (5.1)$$

The parameters in this model include $\beta_F = 58.74 \text{ GeV}^{-2}$, $\alpha_F = 1.085$, $\alpha' = 0.25 \text{ GeV}^{-2}$, $b_0 = 4 \text{ GeV}^{-2}$. Because of the t dependence in α' , the effective exponential slope b_{eff} is between 5 and 9 at measured x_F values ($b_{\text{eff}} = 4 + 2\alpha' \log(1/x_F)$)

HIERACLES [103] provides QED radiative corrections to the model. The parton shower (hard interactions, gluon radiation) is implemented using the ARIADNE [104] color dipole model, assuming that the hadronic final state starts as a $q\bar{q}$ pair. Fragmentation (soft interactions) uses the Lund string model as implemented in JETSET [105]. Events in the low mass region ($< 2 \text{ GeV}$) were usually replaced with either a ρ or ϕ resonance, to approximate the natural formation of resonances.

The parameterization of equation 5.1 can also be compared to the results of [51], where $c = .78 \pm 0.32$, $a = 1.46 \pm .04 \pm .08$.

The generated quantities can be seen in figure 5.4. The following cuts are applied at generator level:

- $Q^2 > 3 \text{ GeV}^2$
- $y > 0.005$
- $M_X > 2m_\pi$
- $x_L > 0.9$
- $t < 1.0 \text{ GeV}$

Since it is desirable that the Monte Carlo agree as closely as possible with the data, weights are applied to the generated events, allowing the parameters b_0 , α_F , and α' to be adjusted. Optimizing the generated structure function is especially important for the bin-by-bin correction. For each event, the weight is:

$$w = N(b_0, \alpha_F, c) \frac{x_F^{-2\alpha_F+2\alpha't-1} [\beta(1-\beta) + \frac{c}{2}(1-\beta)^2] e^{b_0 t}}{x_F^{-2\alpha_{F,gen}+2\alpha't-1} [\beta(1-\beta) + \frac{c_{gen}}{2}(1-\beta)^2] e^{b_0, gen t}}$$

To determine appropriate values for α_F , a Poisson likelihood method is utilized. The data are divided into bins, and the number of events in both the MC (with weights) and the data are accumulated. The likelihood is then calculated using the formula:

$$\log(\mathcal{L}) \equiv \sum_i \log \left[\frac{\mu_i^{n_i}}{n_i!} e^{-\mu_i} \right] \quad (5.2)$$

where μ_i is the number of expected predicted by the Monte Carlo in bin i and n_i is the number of observed events in that bin. This likelihood is maximized by allowing MINUIT to vary the parameters, giving the most probable value of α_F or b_0 . For α_F , two binnings

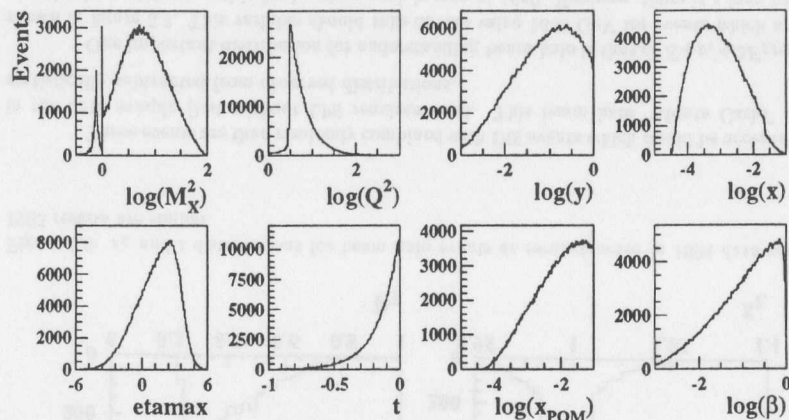


Figure 5.4: Generated quantities for RAPGAP Monte Carlo. Note the resonances apparent in the M_X spectrum.

are used, either the bins of the M_X analysis, or the bins of the x_F analysis. In the $F_2^{D(3)}$ bins, $2\bar{\alpha}_P - 1 = 1.03 \pm_{-0.05}^{+0.05}$, under the assumption that $\alpha'_P = 0.25$. Consequently, α_P was weighted to be 1.08. This will be the nominal weight applied whenever RAPGAP is used. When averaged over t , this corresponds to $\bar{\alpha}_P = 1.04$.

The value of c was tested as well, and the generated value of 0.57 was appropriate.

Agreement between data and Monte Carlo is improved if b_0 is reweighted as well. A similar Poisson reweighting scheme demonstrates that the agreement between data and Monte Carlo is optimized if $b_0 = 1.8 \pm 0.1^{+1.4}_{-0.8}$. Since there is x_F dependence to the t distribution, the effective t distribution is given by

$$\frac{dN}{dt} \propto \exp[(b_0 + \log x_F) t] = \exp(b_{\text{eff}} t) \quad (5.3)$$

where $b_{\text{eff}} \simeq 6.5$ in the generated Monte Carlo and $b_{\text{eff}} \simeq 7.2$ after the weights are applied.

The systematic errors quoted above will be described in section 7.4 and chapter 8.

5.3.2 NIKZAK single diffractive DIS

The NIKZAK Monte Carlo, written by Ada Solano [108], also simulates $cp \rightarrow cpX$ but uses a more complex structure function from the model of Nikolaev and Zakharov (section 2.4.2) to describe single-diffractive events. A sample of 350K events are used to double-check the unfolding procedure. Since low-mass ($M_X < 1.7$ GeV) events were not simulated, the normalization of the ρ MC is increased 30% when used with NIKZAK. This Monte Carlo does not include radiative corrections, and the fragmentation implemented is always a $q\bar{q}$ state even when the physics model requires a $q\bar{q}g$ state.

5.3.3 DIS ρ^0 diffractive

In order to fill in the low-mass region (which may be inadequately described by RAPGAP), a DIS ρ^0 Monte Carlo, which uses HERWIG [109] to include radiative corrections. A sample of 13.3 pb^{-1} is used with $Q^2 > 3$. These events are included in the diffractive sample with the normalization determined from the parameterization of the 1993 measurement of the DIS ρ^0 cross section [110].

5.3.4 EPSOFT double diffractive DIS

This Monte Carlo [111] is used to estimate the background contribution due to diffractive events with proton fragmentation. The overall normalization of this Monte Carlo is determined using a fit to the x_L spectrum for events with $\eta_{\text{max}} < 1.5$. The x_L dependence has been tuned by weighting by $(1 - x_L)^\gamma$, with $\gamma = 0.2$. This gives reasonable agreement between data and Monte Carlo at $x_L \sim 0.9$. Unfortunately, the fragmentation model of EPSOFT could be an inappropriate model for the physical process. The nucleon fragmentation might be different, perhaps modeled better by the Monte Carlo PYTHIA. Diffractive π^0 exchange would also produce a different background. Resonant baryon production such as N^* or Δ production should be considered. Fortunately, these three alternatives are expected to introduce smaller amounts of background, so the EPSOFT value is considered an upper limit on the background at 1%. One systematic check would be to remove this background by statistical subtraction as in chapter 8.

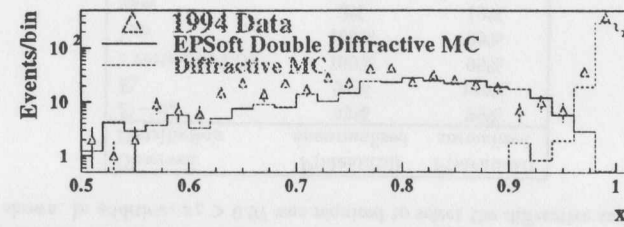


Figure 5.5: x_L distribution for events with $\eta_{\text{max}} < 1.5$.

5.3.5 π^0 Exchange

A sample of π^0 exchange events were simulated using RAPGAP. These events suggest that about 1% of the events observed in the $x_L > .97$ sample could come from this process. This background is statistically subtracted from the observed bins as a systematic check.

5.3.6 Beam halo simulation

Analysis of the 1994 data set has revealed a class of events in which a standard (non-diffractive) DIS event occurs in coincidence with a proton of x_L near 1. These events have been interpreted as overlays of a DIS event with a "Beam Halo" proton, which is a

track from a proton not involved in the collision. Analysis of these events have shown that they are distributed uniformly through the run range. If during reconstruction, the fit is not constrained to the nominal vertex, we observe that the y vertex is somewhat lower than for normal diffractive events, and the distribution of the vertex is in general more broad. The normal reconstruction mode for the LPS is to always constrain the vertex, and with this constraint, the x_L distribution becomes more broad since the track is constrained to a vertex through which the physical particle did not pass.

A sample of overlay protons is easily obtained by taking all events with total calorimeter $E + p_z$ greater than 100 GeV (calorimeter variables are defined in equations 6.2–6.5). It is impossible to have a physics event with $x_L > 0.95$ and $E + p_z > 100$ GeV, because $E + p_z$ for the entire event is a conserved quantity whose initial value is 1640 GeV. After the collision, the LPS track carries $1640x_L$ of $E + p_z$, leaving at most 82 GeV for the calorimeter.

1.1 million events have $E + p_z > 100$ GeV in the 1994 sample, of which 5000 have an LPS track with $x_L > 0.95$. For 1995, the DIS sample provides about 1000 events; other triggers were avoided due to possible bias from the LPS trigger. The x_L and t distributions for the 1994 sample are shown in figure 5.6.

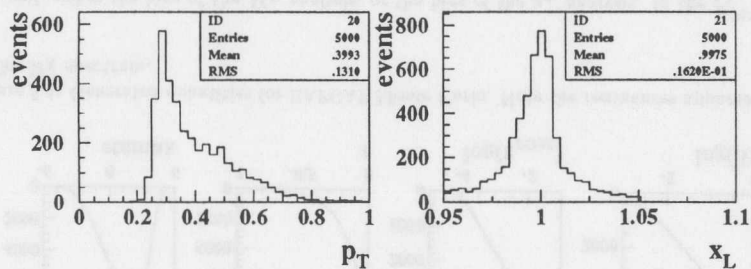


Figure 5.6: x_L and t distributions for beam halo events as reconstructed in 1994 data set. 1995 results are similar.

These events are then randomly combined with DIS events which would be accepted in the data sample (but without LPS requirements). This beam halo “Monte Carlo” is statistically subtracted from observed distributions.

One important distribution for understanding beam halo is that of $E + p_z + 2E_{LPS}$, shown in figure 5.7. This variable should take on the value 1640 GeV for events which are completely contained, and indeed a clear peak is seen at 1640. However, there is a long tail of events with substantially more than 1640 GeV. These beam halo overlay events are easily removed by requiring $E + p_z + 2E_{LPS} < 1660$ GeV; before this cut is made, these events are used to normalize the beam halo Monte Carlo. The fraction remaining after this cut represents a background of about 5%, mostly *diffractive* DIS events with a proton overlay, since primarily diffractive event are observed with small $E + p_z$ value.

5.4 Comparison of data with Monte Carlo

Many variables have been checked to insure that the data are accurately reproduced by the sum of the (RAPGAP, π^0 exchange, beam halo, DIS ρ and EPSOFT) Monte Carlo. These plots are shown in figures 5.7–5.9. Using the Kolmogorov-Smirnov test, these distributions are demonstrated to be likely to have the same parent distribution. These tests can be done either with floating normalization for each comparison or with a fixed normalization; both results are shown in table 5.1, but the result using fixed normalization is probably more appropriate. Chapter 6 has definitions of these variables. In these comparisons, the cuts described in chapter 6.5 are always applied unless the cut involves the variable shown. In addition, $x_L > 0.97$ was required to select the diffractive sample.

Observed Distribution	$P(\text{identical})$ unnormalized	$P(\text{identical})$ normalized
$E - p_z$	93%	99%
E_c	92%	100%
z vertex (CTD)	100%	99%
Y_{JB}	100%	99%
η_{\max}	3%	13%
$E + p_z + 2E_{LPS}$	100%	99%
d_{pipe}	91%	98%
$N_{\text{miss}}/N_{\text{hit}}$	72%	94%
$p_{x,LPS}$	20%	49%
$p_{y,LPS}$	92%	98%
χ^2	99%	99%
x_L	0%	0%
N_{hit}	0%	1%
$x_{\pi LPS} - x_{\pi CAL}$	99%	99%
β	92%	96%
x_T	97%	98%
x_{DA}	100%	99%
M_X^2	100%	95%
Q_{DA}^2	89%	97%
y_{DA}	100%	99%
t	100%	99%
x_L for $\eta_{\max} < 1.5$	100%	37%

Table 5.1: Agreement of 1994 data and Monte Carlo, determined using Kolmogorov-Smirnov test. Shown is the probability that the data and Monte Carlo distributions have been drawn from the same parent distribution.

Some distributions do not show agreement between data and Monte Carlo and need further explanation. The x_L distribution is poorly reproduced at small $x_L \lesssim 0.6$; this shouldn't be surprising since no effort has been made to reproduce the low- x_L region in this thesis. The N_{hit} distribution is poorly reproduced because this variable was not a target of the run-to-run detector movement corrections of section 5.2.6. As a result, more

events are 2-station tracks in data than in the Monte Carlo, which has a higher-acceptance configuration.

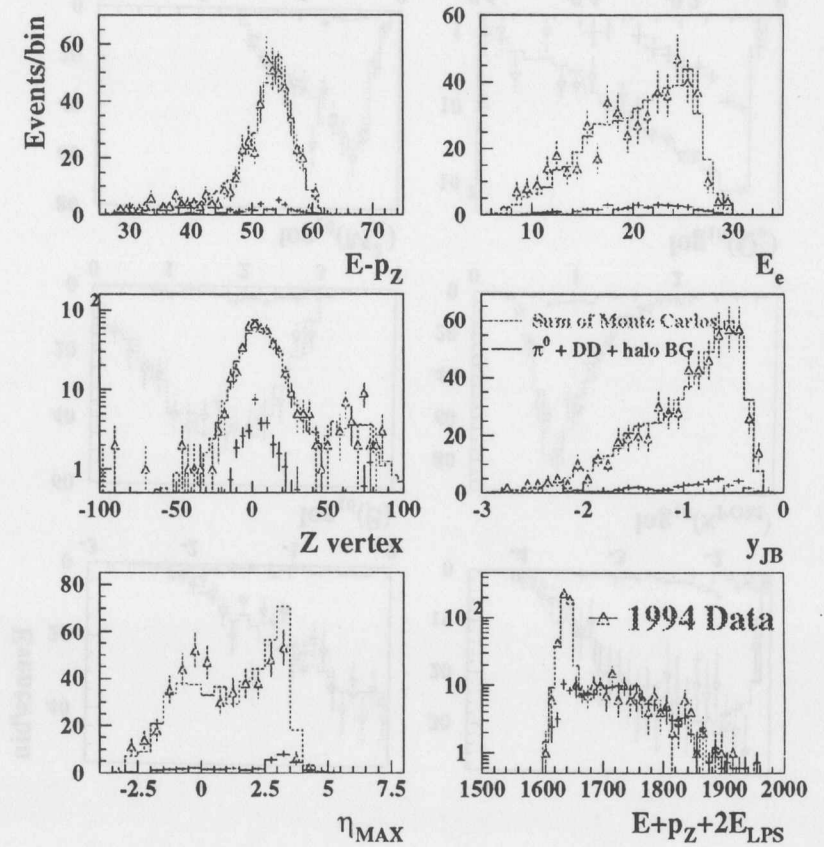
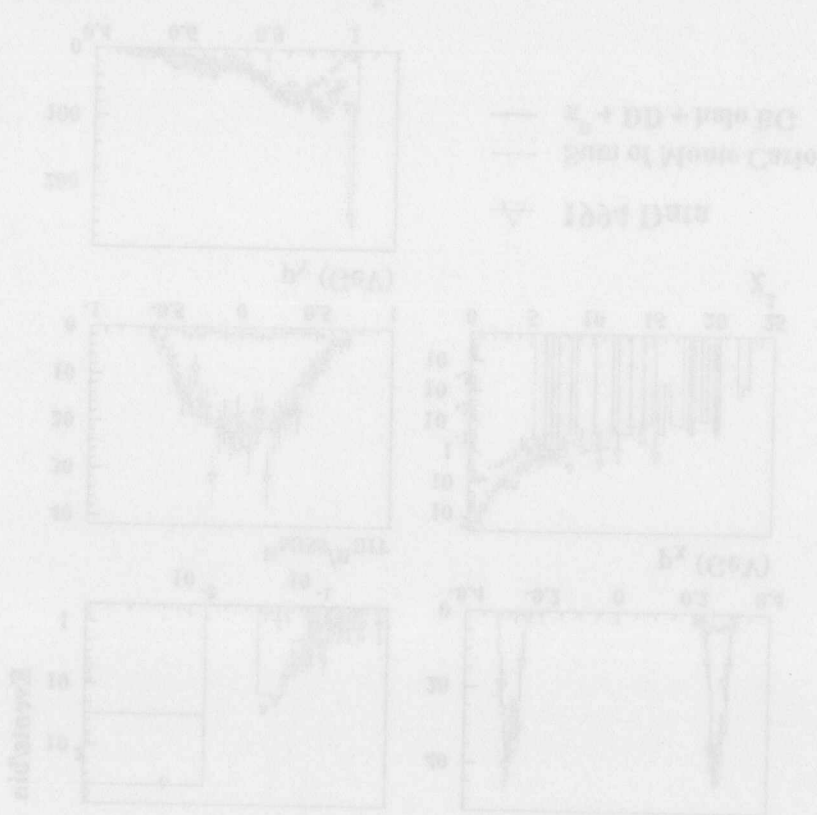


Figure 5.7: Comparisons of 1994 DIS variables in data and Monte Carlo. Data are triangles, and the histograms represent all Monte Carlo samples, or only the background samples.

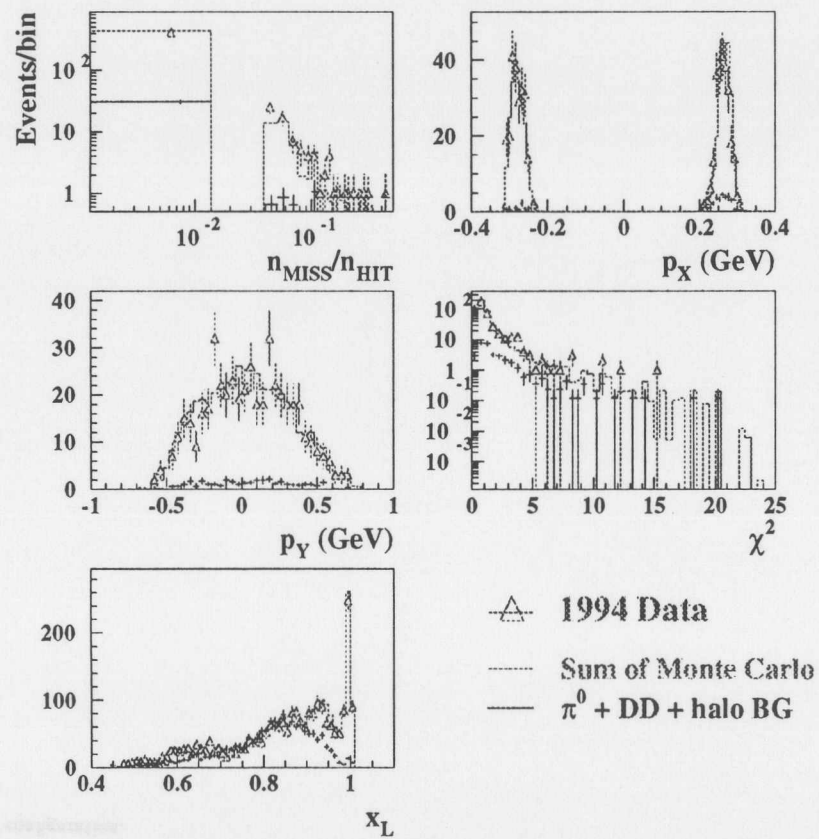


Figure 5.8: Distributions of LPS variables in 1994 data and Monte Carlo.

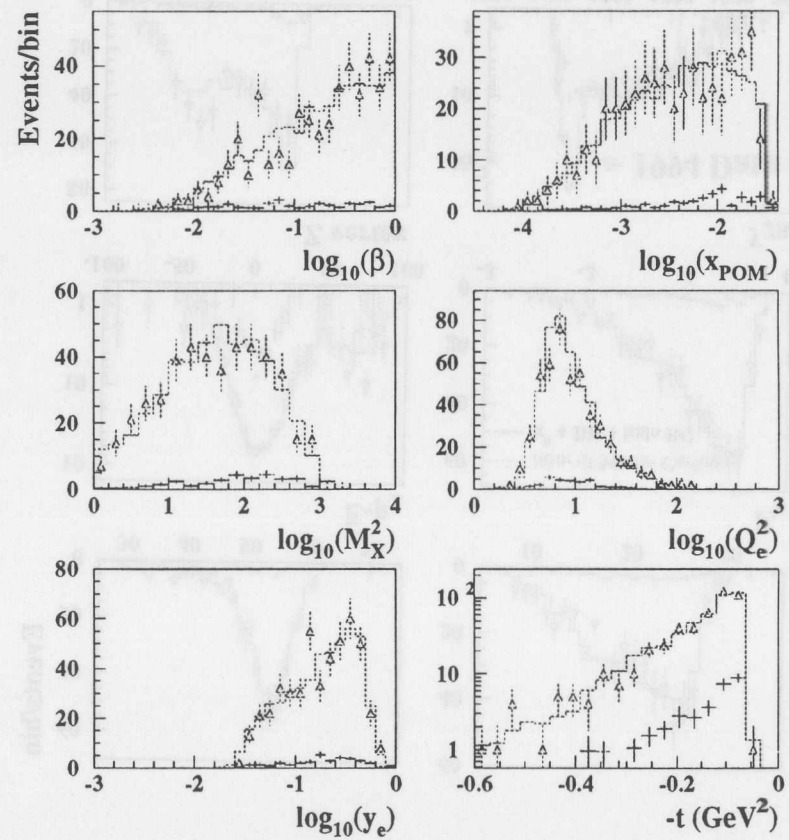


Figure 5.9: Comparisons of physics variables for 1994 data and Monte Carlo.

5.5 Simulating 1995 data

The 1994 Monte Carlo simulation was extended in order to describe the 1995 data. There were a few changes to the detector which influenced the acceptance for 1995 data:

- The beam pipe hole in the RCAL was reduced to 10×20 cm
- S1-S2 detectors were added for part of 1995
- Locations of S4-S6 were considerably farther from the beam than 1994
- Beam tilt and vertex positions are different

The beam pipe change can easily be accommodated by using the same box cut for both 1994 and 1995 data, although this results in the loss of considerable statistics at low Q^2 . However, including the change in LPS configuration is more complex. Many of the leading protons which hit S4-S6 detectors in their 1994 configuration will be accurately simulated if the appropriate reweighting file is included (section 5.2.6). However, some of the 1995 tracks could not be observed by detectors in the 1994 configuration, including all tracks reaching S1-S2. For these tracks, the solution was to parameterize the reconstructed variable resolution using the ρ^0 information from table 4.8. For the tracks which were expected to reach the LPS but did not due to the 1994 configuration, the generated parameters were smeared to approximate the appropriate reconstructed values. The reconstructed x_L was further smeared as in section 5.2.5, somewhat more than for 1994 reconstruction, to better reproduce the observed x_L spectrum for ρ^0 events (table 4.8).

A comparison of this simplified simulation with the combined 1994 and 1995 data sets can be seen in figures 5.10 and 5.11. The agreement is not as good as the 1994 data alone.

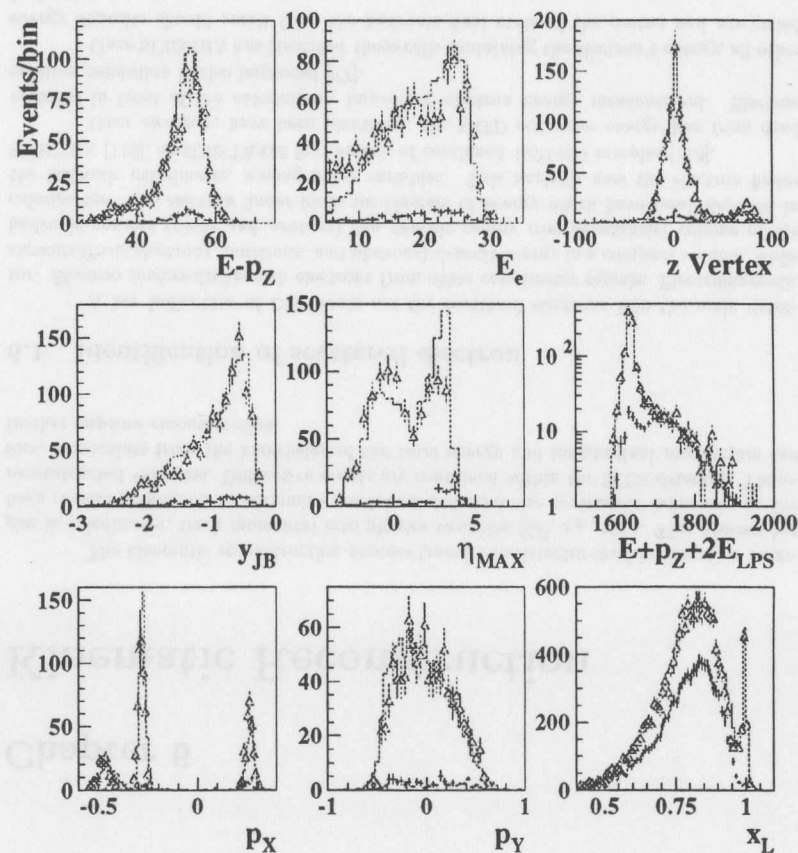


Figure 5.10: Comparison of detector-level variables with 1994 and 1995 data.

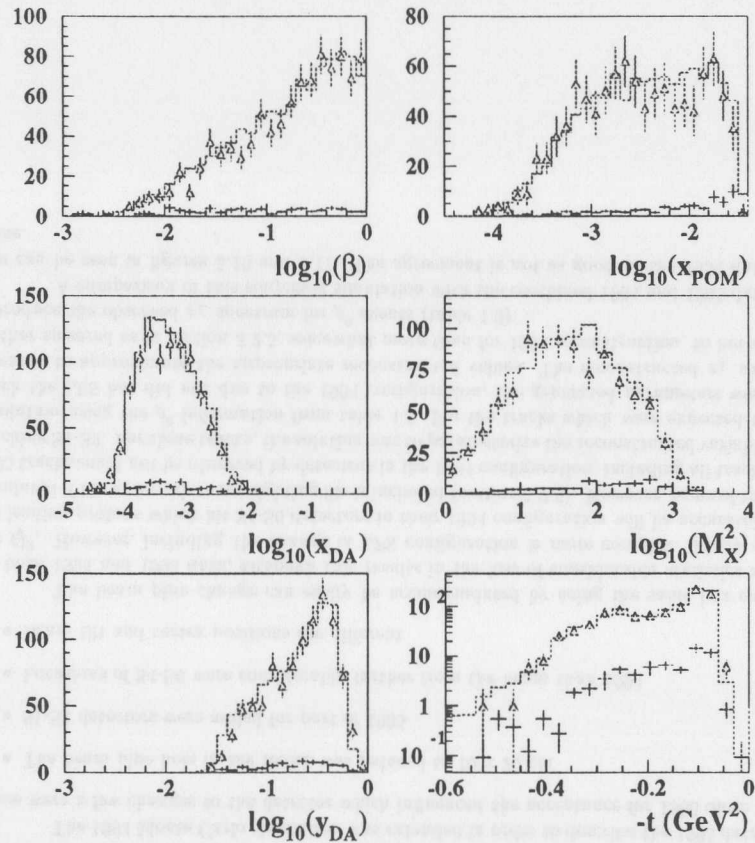


Figure 5.11: Comparison of physics variables between data and simulation.

Chapter 6

Kinematic Reconstruction

The kinematic reconstruction process transforms detector-level information (energies in calorimeter, track momenta) into physics variables (Q^2 , x_p , etc.). This process has been carefully designed to maximize resolution and minimize systematic influences on the reconstructed variables. Diffractive events are contained within the ZEUS detector. Therefore, constraints from the knowledge of the total energy and longitudinal momentum can further improve reconstruction.

6.1 Identification of scattered electron

A key indication of DIS events are the scattered electrons into the main detector. *Electron finders* distinguish electrons from other calorimeter signals. Electromagnetic showers (from electrons, positrons, and photons) deposit energy in a compact volume, while hadronic sources (pions and protons) can deposit energy over substantial volume of the calorimeter. The electron finder looks for clusters of energy which have small deposits in the hadronic calorimeter, among other variables. This analysis uses the electron finder SINISTRA [112], or SINISTRA95 for analysis of combined 1994+95 samples [113].

Once electrons have been identified, the SRTD estimates energy loss from dead material in front of the calorimeter, improving electron energy measurement. Electron position resolution is also improved [77].

Once SINISTRA has identified those cells containing the electron's energy, all other energy deposits should result from the hadronic final state of the proton and are called *hadronic*.

6.2 Calorimeter-track matching and noise suppression

For track matching, tracks are associated with energy deposits in the calorimeter. The routine responsible for making this match, TRAILS, extrapolates tracks to the calorimeter. Tracking requirements are identical to the ρ^0 sample of section 4.4.2. Cells which are touched by the extrapolated track, and additionally adjacent cells to those tracks, are matched to the track. Correlation between track momentum and the calorimeter energy associated with the track is shown in figure 6.1. In this figure, the solid line denotes equal

calorimeter and tracking momentum. Tracks which have less than 300 MeV are removed by the tracking quality cuts.

Once matches have been made, the track energy (assuming the particle has mass of a π^\pm) is subtracted proportionally from all matched cells, leaving a new calorimeter energy pattern denoted by the values E'_{cell} . Electron energy and any tracks leading to it are ignored. The intention here is to identify isolated, charged particles. The remaining energy deposited in the calorimeter would be the result of neutral or large-angle energy deposits (which have no associated tracks) or clusters of neutral and charged particles.

The noise suppression algorithm differentiates between isolated cells and clustered cells. All cells are required to meet the conditions:

$$E'_{cell} > 0.15 * \sqrt{E_{cell}} + 0.04(\text{EMC}); E'_{cell} > 0.35 * \sqrt{E_{cell}}(\text{HAC}) \quad (6.1)$$

Thus, cells with less than 80 (110) MeV are always removed from the analysis. This cut can be seen in figure 6.1 by the dotted line; events with energy less than this line will have all calorimeter energy removed from the analysis. Islands are made from the remaining cells. Isolated cells are removed if they have less than 140 (160) MeV, are on the list of noisy calorimeter cells, or if they have imbalance greater than $0.5 * E_{cell} + 0.03$ GeV. Histograms in figure 6.2 show the amount of calorimeter noise suppressed by these requirements.

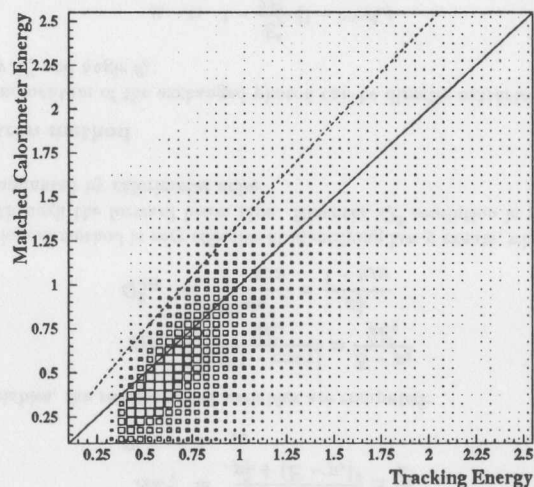


Figure 6.1: Correlation between tracking energy and calorimeter energy for events in the 1994 DIS sample

This hadronic information is used to calculate y_{JB} , M_X , and Double-Angle variables. Since the noise cut is quite high, no further effort has been made to optimize Monte Carlo description of calorimeter noise.

Another calorimeter-track matching algorithm developed within the ZEUS collaboration, called ZUFOS, has been used as a systematic check.

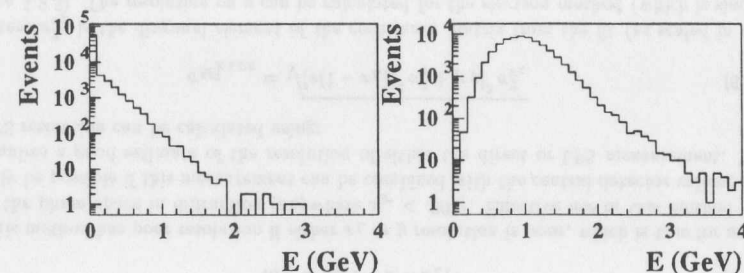


Figure 6.2: Calorimeter noise suppressed from non-isolated (left) and isolated cells.

6.3 Reconstruction of DIS kinematical variables

Variables related to the virtual photon (x , Q^2 , and y) are reconstructed using one of four methods: Jacquet-Blondel, electron, Double-Angle, or Σ . While each has particular advantages and limitations, the Double-Angle method has been chosen as the primary reconstruction method. Each method is briefly described here; further information including systematics are available in [19, 114]. Formulas for Q^2 and y are presented; x and W can be reconstructed using $x = Q^2/ys$ and $W^2 \simeq ys$.

The information from the calorimeter generally requires the electron energy E'_e and angle θ_e . The hadronic energy is generally expressed in terms of the energy and momentum sums E and p_x , p_y , and p_z :

$$E = \sum_{\text{cells}} E_i; \quad (6.2)$$

$$p_x = \sum_{\text{cells}} E_i \cos \phi_i \sin \theta_i; \quad (6.3)$$

$$p_y = \sum_{\text{cells}} E_i \sin \phi_i \sin \theta_i; \quad (6.4)$$

$$p_z = \sum_{\text{cells}} E_i \cos \theta_i; \quad (6.5)$$

$$p_T = \sqrt{p_x^2 + p_y^2} \quad (6.6)$$

For this analysis, the sum over i includes all CTD tracks plus calorimeter energy not matched to those tracks.

6.3.1 Jacquet-Blondel method

With the Jacquet-Blondel method, variables are reconstructed using only the information from the hadronic part of the event. Ideally, this reconstruction method would use the angle of the struck quark, γ , and its energy F . However, fragmentation prevents direct measurement of these variables. Jacquet and Blondel [115] developed a method for recovering the struck quark angles and energies from the final state hadrons after fragmentation. This method works even when some of the final hadrons escape undetected through

the forward beam pipe (otherwise, the detector must be hermetic). The energy sums give the struck quark energy F and angle γ :

$$\cos \gamma = \frac{p_T^2 - (E - p_z)^2}{p_T^2 + (E - p_z)^2} \simeq \frac{p_z}{E} \quad (6.7)$$

$$F \sin \gamma = p_T \quad (6.8)$$

From these variables, the reconstructed variables are computed:

$$y_{JB} = \frac{F(1 - \cos \gamma)}{2E_c} = \frac{E - p_z}{2E_c} \quad (6.9)$$

$$Q_{JB}^2 = \frac{F^2 \sin^2 \gamma}{1 - y_{JB}} = \frac{p_T^2}{1 - y_{JB}} \quad (6.10)$$

The Jacquet-Blondel method is very effective at identifying low- y events, where all hadronic energy is lost through the forward beam pipe. However, Q^2 resolution is poor, and low- y resolution is dominated by calorimeter noise.

6.3.2 Electron method

The momentum of the exchanged photon can be directly extracted from the final electron energy E'_c and angle θ_c :

$$y_c = 1 - \frac{E'_c}{2E_c} (1 - \cos \theta_c) \quad (6.11)$$

$$Q_c^2 = 2E_c E'_c (1 + \cos \theta_c). \quad (6.12)$$

The electron method has very good resolution at large- y and generally has good Q^2 resolution. At low- y , y is determined from $E_c - E'_c$, which is nearly zero and smaller than the electron energy resolution. Therefore, the electron method cannot be used for small y . The electron method is the most sensitive to radiative effects.

6.3.3 Double-Angle method

Both electron and Jacquet-Blondel methods require accurate absolute calorimeter calibration. The Double-Angle method has no dependence on the overall energy scale (although relative calibration within the calorimeter must be accurate). The two angles, γ (equation 6.7) and θ_c are related to the physics variables as:

$$y_{DA} = \frac{(1 - \cos \gamma) \sin \theta_c}{\sin \gamma + \sin \theta_c - \sin(\theta_c + \gamma)} \quad (6.13)$$

$$Q_{DA}^2 = 4E_c^2 \frac{(1 + \cos \theta_c) \sin \gamma}{\sin \gamma + \sin \theta_c - \sin(\theta_c + \gamma)} \quad (6.14)$$

6.3.4 Σ method

An alternative method for reconstructing kinematic variables comes from the III experiment [116]. This method should have good precision at low- Q^2 , and does not depend on the transverse momentum of the hadronic particles, which generally have poor resolution.

$$y_\Sigma = \frac{E - p_z}{E - p_z + E_c(1 - \cos \theta_c)} \quad (6.15)$$

$$Q_\Sigma^2 = \frac{E_c^2 \sin^2 \theta}{1 - y_\Sigma} \quad (6.16)$$

6.4 Reconstruction of diffractive variables

The diffractive variables can be measured more precisely with the inclusion of LPS information. First, the method for obtaining diffractive variables in the absence of LPS information is presented.

Diffractive variable reconstruction in the central detector starts with reconstructing M_X . There are two methods: using the angle [53] or direct approach. The angle method is not sensitive to changes in the energy scale of the calorimeter, but has poor resolution. The direct approach uses the energy deposited in the calorimeter (or matched calorimeter-track objects) according to the formula

$$M_X^2 = E^2 - p_x^2 - p_y^2 - p_z^2 \quad (6.17)$$

and is used in this analysis. Dead material reduces the energy observed by the detector, and this loss needs to be compensated by scaling the observed M_X by a factor determined from the Monte Carlo to be 1.68 (1.62 for ZUFOs). For comparison, using only the calorimeter (no tracking) for M_X determination, the scale factor was determined to be 2.16. In order to correctly reconstruct M_X using this method, the entire event needs to fall within the calorimeter. Analysis of the generated rapidities of individual particles within RAPGAP events demonstrates that for $x_L > 0.95$, only 1.2% of the events have particles (besides the leading proton) generated at rapidities greater than 1.3. Thus, diffractive DIS events are, in general, fully contained.

M_X can also be measured using only the electron and proton with the formula:

$$M_X^2 = sy(1 - x - x_L) \quad (6.18)$$

This method has poor resolution if either x_L or y resolution is poor, which is true for much of the phase space in diffraction (anywhere $x_p < .003$). Effective use of this method will only be possible if this measurement can be combined with the central detector values; this requires a good estimate of the resolution of either the direct or LPS measurement. The LPS resolution can be calculated using:

$$\sigma_{M_{X,LPS}}^2 = \sqrt{[s(1 - x_L)]^2 \sigma_y^2 + [sy]^2 \sigma_{x_L}^2} \quad (6.19)$$

where $\sigma_{x_L}^2$ is the diagonal element of the covariance matrix from the fit (as scaled in section 5.2.5). The resolution on y can be calculated for the electron method (which is similar to the Double-Angle resolution):

$$\sigma_y^2 = \frac{1}{4E_c^2} \left[\sigma_{E'}^2 (1 - \cos \theta_c)^2 + \sigma_\theta^2 (E'_c \sin^2 \theta_c) \right] \quad (6.20)$$

The errors on the electron measurement are $\sigma_E = 0.26\sqrt{E_c}$ and $\sigma_\theta = 2$ mrad. A weighted average is calculated using the calorimeter error in measuring M_X , 30%, and averaged with the error from the electron+proton method:

$$M_X^2 = \frac{\frac{M_{X,LPS}^2}{\sigma_{M_{X,LPS}^2}^2} + \frac{M_{X,cal}^2}{(0.4M_{X,cal}^2)^2}}{\frac{1}{\sigma_{M_{X,LPS}^2}^2} + \frac{1}{(0.4M_{X,cal}^2)^2}} \quad (6.21)$$

The variable β can be easily calculated using equation 2.17 while t is reconstructed using the proton p_T as in equation 2.15.

The LPS provides additional information about x_p . As shown in equation 2.14, x_p can be obtained either from M_X , W and Q^2 or from the p_x of the proton. LPS resolution is approximately constant with x_L , and the central detector can do better than the LPS for small x_p . The errors are well understood: in the LPS, they are taken from the covariance matrix of the LPPFIT; in the calorimeter, they are approximately 20% of the measured x_p . A weighted average of the LPS $x_p = 1 - x_L$ and the central detector $x_p = \frac{Q^2 + M_X^2 - t}{W^2 + Q^2 - M_p^2}$ (with M_X only from the central detector), provides the final reconstructed x_p .

The offsets and resolutions of these reconstructed variables, based on the RAPGAP simulation, are shown in figure 6.3.

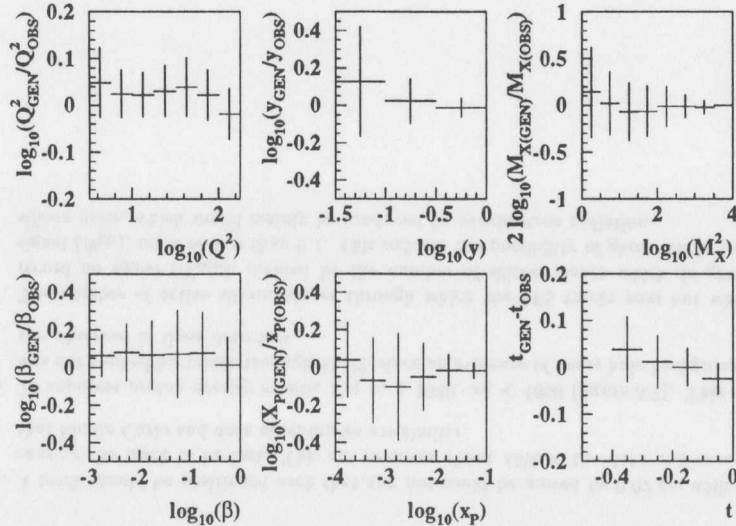


Figure 6.3: Resolutions of reconstructed variables. The horizontal axis is the measured variable. The error bars indicate 1- σ resolution from a Gaussian fit in that bin.

6.5 Event selection

During 1994 (1995), 905 (3531) nb^{-1} have been selected from stable runs with reliable LPS data taking conditions. Event selection is nearly identical to the F_2 analysis [20]. Additional cuts are applied to ensure good kinematic reconstruction and select the LPS diffractive sample.

One variable used in the F_2 analysis is $\delta \equiv E - p_x$ including the electron. For a perfect detector which has contained all backwards particles (but lost an arbitrary amount of particles through the forward beampipe), δ should be exactly twice the electron energy, since both E and p_x are conserved from their initial values. Photoproduction and events with substantial initial state radiation lose particles through the rear beam pipe hole. For these events, δ falls by twice the energy of the lost particle (since for particles through the rear beam pipe, $p_x \simeq -E$). Thus, requiring δ to be near $2E_c$ reduces these backgrounds.

A similar variable is used for LPS backgrounds: $E + p_x$. However, the problematic background for this measurement comes from overlay of beam-halo protons with nondiffractive DIS events. By requiring $E + p_x$ not much more than $2E_p$, most of these events are eliminated. Those which remain (approximately 5%) are statistically subtracted using the beam halo Monte Carlo (section 5.3.6)

With these definitions, the actual cuts to extract the DIS sample include:

1. Box cut. In 1994, any electrons for which the x or y position at the calorimeter was smaller than 13 cm was removed, because these electrons were too close to the beam pipe for accurate reconstruction. In 1995, the calorimeter geometry was modified, allowing a reduction of the box cut to $|y| < 6$ and $|x| < 12$ cm. Some additional cuts removed faulty regions of the calorimeter. When precise simulation of the acceptance was required, the 1994 box cut was applied to the 1995 data as well.
2. $y_{JB} > 0.03$ for good electron reconstruction
3. $y_e < 0.9$ to reject photoproduction
4. $40 < \delta < 65$ to exclude photoproduction and ISR events
5. SINISTRA electron. The finder must return a confidence above 90% and energy greater than 10 GeV after SRTD corrections. Analysis of 1994+95 data uses version SINISTRA95.
6. Vertex. If the z vertex is reconstructed, it is required to be between -50 and 100 cm; otherwise, the average z vertex for that run is used. The x and y vertices are always placed at the average VCTRACK value for that run.

The LPS selection entails the following cuts:

1. Require a reconstructed LPS track.
2. Require χ^2/DOF of the fitted track to be less than 10.
3. $x_L < 1.02$
4. Distance of closest approach to the beam pipe should be at least 0.04 cm.

5. A track should be positioned such that any pot could be moved by 0.02 cm without causing the track to be lost. This cut removes about 15% of the data and ensures that Monte Carlo and data acceptances are similar.
6. To suppress proton overlay events, $E + p_z + 1640 \cdot x_L < 1660$ (figure 5.7). This cut was not applied for tracks through S1-S2, since no evidence of beam halo backgrounds was observed in these detectors.
7. The number of active silicon planes through which the LPS tracks pass but which record no signal (N_{miss}), divided by the number of silicon planes which do give a signal (N_{hit}), must be less than 0.1. This reduces the possibility of ghost tracks from silicon noise, which would mainly be produced by synchrotron radiation.

Chapter 7

General Properties of DIS Events with LPS Tracks

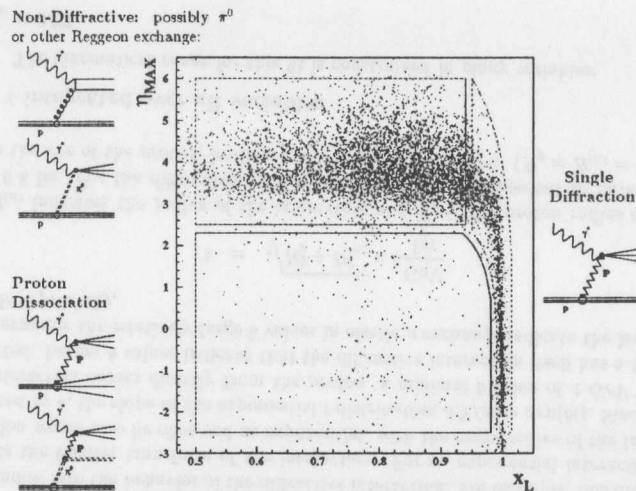
7.1 LPS selection of diffractive events

Many previous analyses have attempted to analyze diffraction without selecting events with a forward proton. These selections typically use either the presence of a rapidity gap [53, 54, 117, 118] or small diffractive masses [51]. However, tagging the leading proton is clearly far superior to previous methods, for a number of reasons:

- Non-diffractive background is difficult to accurately simulate (one discussion follows in section 7.5), and therefore final results have dependence on the assumption of the non-diffractive event shape.
- Diffractive event shapes can lead to varying η_{max} distributions. Event distributions may be poorly described by the Monte Carlo, which leads to dependence on the η_{max} cut.
- QED Compton events, of the form $ep \rightarrow e\gamma p$, can mimic a diffractive signal at high- y . However, the proton's transverse momentum is almost always too small to place the proton in the LPS, so these events are suppressed.
- The LPS provides additional information on the longitudinal momentum transfer (x_p) and the only information on transverse momentum transfer (t and $\Delta\phi$).
- Events in which the proton dissociates would be unlikely to be mistaken for single-diffractive events. Without direct observation of the proton, such events would ordinarily be accepted, since the proton remnant would likely remain inside the beam pipe.

7.2 x_L distribution

The x_L distribution for DIS events reveals that the LPS accepts a large number of events at moderate- x_L . This is primarily due to the large increase in acceptance for events near $x_L = 0.8$. The other traditional diffractive selection variable, η_{max} , can be compared

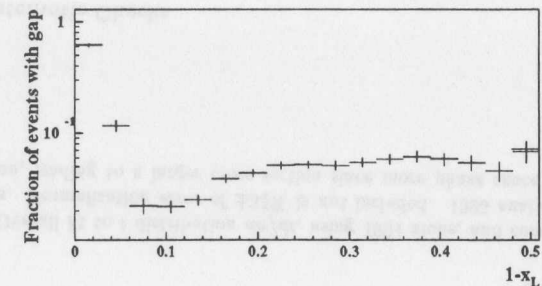
Figure 7.1: Regions of the $x_L - \eta_{\max}$ plane.

with the LPS variable x_L as shown in figure 7.1. Three regions are defined on this scatter plot. First, the events with x_L near 1 and (mostly) a rapidity gap are on the right edge of this picture; these are traditional single-diffractive events. A second category, with a leading proton which carries less than 95% of the initial proton momentum and without a detectable rapidity gap, could be the result of either π^0 (or other Reggeon) exchange, or could result from a fluctuation in the fragmentation leading to a very forward final particle. Finally, there are events with x_L relatively small, and with a rapidity gap. In events of this sort, the detector was not hermetic and some particles escaped into the forward beam pipe. Two possible sources are shown. If the proton dissociates into many particles, one could carry enough momentum to be observed in the LPS. Resonances (N^* , for example) would be particularly likely to produce a high-energy particle which could be observed in the LPS. The other possibility is that these events represent diffraction on a pion (or other Reggeon) exchange.

As a function of x_L , the fraction of events satisfying the diffractive cut $\eta_{\max} < 1.5$ can be determined. Figure 7.2 demonstrates an interesting feature: the events immediately below the single diffraction peak are unlikely to produce rapidity gaps. At $x_L = 0.93$, only 2% of the data produce rapidity gaps, compared with closer to 6% at very low x_L [119].

7.3 $\Delta\phi$ distribution

Using a Regge-based prediction, Gehrman and Stirling [120] predicted an enhancement of events with $\Delta\phi$ near 180° . $\Delta\phi$ is the electron-proton acoplanarity angle. This section considers this variable in some detail. First, a short discussion of the argument

Figure 7.2: Fraction of events with a rapidity gap as a function of $1 - x_L$.

for why Gehrman and Stirling expect a correlation. According to their analysis, the Regge prediction for the x_F dependence of the structure function should be expressed in terms of the variable α_p . This variable can be expressed as

$$\alpha_p = \frac{(p - p') \cdot k}{p \cdot k} \quad (7.1)$$

This definition differs slightly from the previously defined variable x_F . α_p is much closer to $1 - x_L$. The difference between x_F and α_p is simply

$$\frac{\alpha_p - x_F}{x_F} = 2\beta \sqrt{-\frac{t(1-y)}{Q^2}} \cos \Delta\phi_{cp} \quad (7.2)$$

and is typically a few percent, largest at small Q^2 or large β . Therefore, instead of expecting the x_F distribution to be distributed as $x_F^{1-2\alpha_p}$, the correct distribution would have dependence $\alpha_p^{1-2\alpha_p}$. This leads to a dependence on the variable $\Delta\phi_{cp}$.

This measurement is easy to perform, since the resolution is good in both electron and proton ϕ . Since electron ϕ acceptance is essentially uniform, the variable $\Delta\phi$ has uniform acceptance. The raw $\Delta\phi$ values for all diffractive events, as well as for those events with values of $x_F < .0003$ (about 347 events) are shown in figure 7.3. For these small x_F values, a clear preference is observed for the electron and proton to be anticorrelated. To both distributions, a fit of the form:

$$\frac{dN}{d\Delta\phi} \propto 1 + \rho \cos \Delta\phi \quad (7.3)$$

has been performed. The resulting ρ values are -0.067 ± -0.026 for the inclusive DIS sample, and -0.17 ± -0.07 for events with small observed x_F ($\chi^2/DOF = 1.3$). Thus, a statistically significant deviation from a uniform $\Delta\phi$ distribution is apparent. This result is essentially consistent with the values expected from Gehrman and Stirling, for those events where the change in longitudinal and transverse momentum are nearly the same.

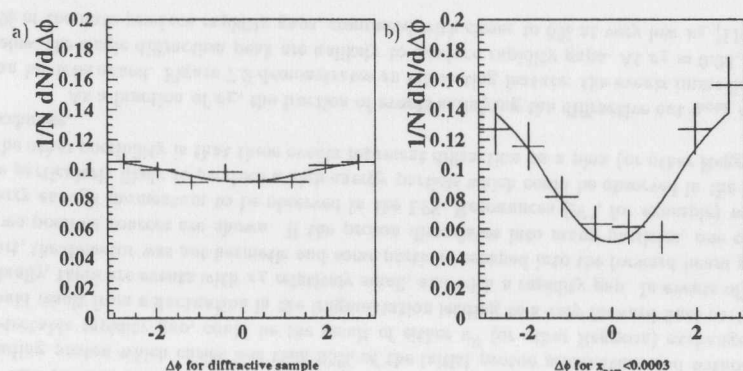


Figure 7.3: Distribution of the variable $\Delta\phi$, for all diffractive events and those at small x_p .

7.4 t Distributions

The transverse momentum distribution for the outgoing protons provides an interesting window into the behavior of the diffractive interaction. For example, this distribution represents the Fourier transform of the interaction. For an exponential interaction, the t distribution would also be observed as exponential, with the mean radius of the interaction represented by b , the slope of the exponential t distribution $dN/dt = \exp(bt)$. Since the size of the interaction comes directly from the proton, a minimal b value of 1 GeV^{-2} should be expected. Larger b values indicate that the diffractive interaction itself has a transverse size, for example the relatively large b values in elastic ρ exchange indicate the large size of the ρ . More precisely,

$$b = \sqrt{R_p^2 + R_{int}^2} \times 5 \frac{\text{GeV}}{\text{fm}} \quad (7.1)$$

where R_{int} indicates the radius of the interaction and R_p is the proton radius of approximately 0.8 fm. For the diffractive reaction, the interaction is expected to have the same range as the size of the proton, leading to a b value of closer to 6. ($R_p = R_{int} = 0.8$).

7.4.1 t integrated over all variables

The kinematical range for this fit is constrained in many variables:

- $x_p < 0.03$
- $0.02 < \beta < 0.5$ ($0.02 < \beta < 1.0$, 1995)
- $50 < W < 210 \text{ GeV}$ ($W < 210 \text{ GeV}$, 1995)
- $5 < Q^2 < 20 \text{ GeV}^2$
- $0.073 < |t| < 0.1 \text{ GeV}^2$

The cross sections are determined using a bin-by-bin correction (section 8.1), and the center of the bin is placed at the appropriate value for the exponential dependence shown in figure 7.4. Details about the binning, including the purity, efficiency, and cross section values, are shown in table 7.1. The smearing of the t values dominate the purity determination.

A χ^2 fit is made to the data points using an exponential function e^{bt} , where b is referred to as the t slope for the fit, yielding values $b = 6.6 \pm 0.6^{+1.2}_{-0.6}$ for χ^2 method; compare with $b = 7.2 \pm 0.4^{+1.4}_{-0.8}$ obtained by reweighting the MC. The χ^2 value obtained with this fit is 0.34 (with 2 degrees of freedom). The results of the systematic checks are plotted in figure 7.5. The top row indicates the effects of systematic checks on the overall cross section, after removing correlated changes amounting to $\pm 35\%$. The bottom row indicates the systematic changes to χ^2 , likelihood, and MC reweight methods.

Correlated errors in normalization, amounting to $\pm 35\%$, have been removed in these plots.

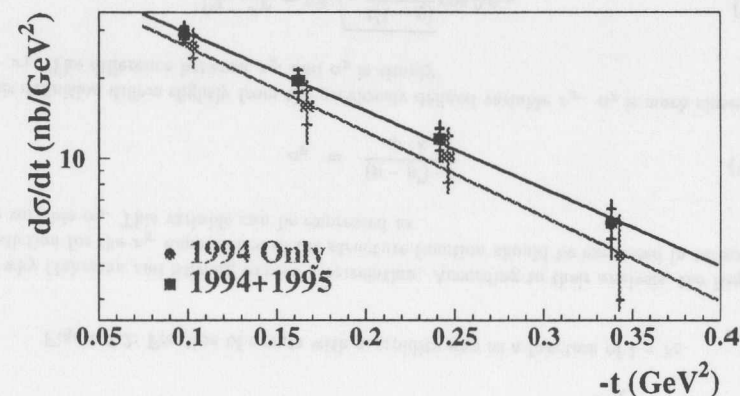


Figure 7.4: Overall fit to t distribution $d\sigma/dt$, using 1994 alone, and combined 1994 and 1995 samples. Normalization error of $\pm 35\%$ is not included. 1995 analysis uses relaxed event selection, leading to a larger cross section since more phase space in y and β are included.

7.4.2 Systematic Checks

Many systematic checks were applied to the t distribution measurement. They can be loosely categorized into checks on electron reconstruction, proton reconstruction, diffractive kinematics reconstruction, and simulation. Figure 7.5 shows a plot of these systematic checks on the χ^2 fitted b values.

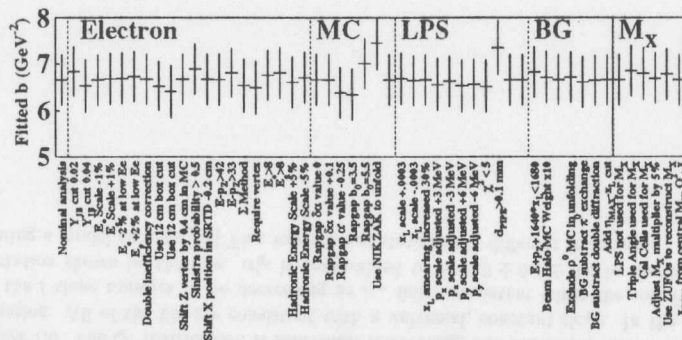


Figure 7.5: Results of systematic checks.

t range	$\langle t \rangle$	N_{data}	N_{MC}	Purity	Efficiency	Background	$d\sigma/dt$
$-1 < t < -0.29$	-0.33	11	14	23%	1.4%	4.1%	$4.3 \pm 1.4^{+1.2}_{-0.9}$
$-1 < t < -0.29$	-0.33	68	74	20%	1.1%	2.5%	$5.8 \pm 0.7^{+1.0}_{-1.0}$
$-0.29 < t < -0.2$	-0.24	28	31	40%	2.9%	4.6%	$10.2 \pm 2.0^{+2.0}_{-1.9}$
$-0.29 < t < -0.2$	-0.24	131	138	40%	2.1%	3.5%	$11.8 \pm 1.1^{+1.7}_{-1.9}$
$-0.2 < t < -0.13$	-0.16	51	62	35%	3.8%	2.8%	$15.7 \pm 2.3^{+3.1}_{-3.7}$
$-0.2 < t < -0.13$	-0.16	113	125	35%	1.9%	3.9%	$19.5 \pm 1.9^{+3.3}_{-2.9}$
$-0.13 < t < -0.072$	-0.099	106	120	50%	5.4%	3.5%	$26.3 \pm 2.7^{+3.7}_{-3.7}$
$-0.13 < t < -0.072$	-0.099	229	267	50%	2.2%	2.5%	$29.0 \pm 2.0^{+3.0}_{-1.6}$

Table 7.1: Results for $d\sigma/dt$ (nb/GeV²) and details on binning. Background refers to the beam halo background, which has been subtracted from each bin. Within each bin, the top line refers to the 1994 analysis alone, and the bottom line to the combined 1994 and 1995 analysis.

Electron and M_X systematic checks

Using the Σ method instead of double-angle for reconstruction of Q^2 and x results in a small normalization and slope change. Adjusting the box cut to 12 cm and 14 cm caused normalization changes of approximately 8%, indicating the normalization uncertainty caused by the inappropriate simulation near the electron beam pipe. Other changes, which all caused less than 5% change in the results, included: varying the electron energy scale $\pm 1\%$, varying the y_{JB} cut to 0.02 and 0.04, requiring a z vertex, requiring $E - p_x > 42$ or 35 GeV, requiring the energy of the electron to be greater than 8 GeV, shifting the z vertex or calorimeter position, adjusting the minimum SINISTRA probability, and varying the overall calorimeter energy scale by 5%. Varying the reconstruction of diffractive variables caused small changes in normalization.

Proton checks

The x_L scale is determined using elastic ρ^0 events whose energy is very close to 820 GeV. However, the limited statistics cause the placement of the $x_L = 1$ peak to have limited resolution, and prompting a check on the influence of this limited resolution. The measured x_L value is adjusted by ± 0.0004 , consistent with the resolution from ρ^0 measurements (section 4.4.4). The resulting change in the slope is negligible.

The x_L resolution is not known exactly due to the problem of small movements of the motors, as described in section 5.2.5. The amount of smearing applied is increased by 33% to check the sensitivity of the measurement on this value. The slope changes negligibly.

The p_x and p_y values are centered on zero (equivalent to finding the beam) by using ρ^0 events (section 4.4.8). Again, this step has limited resolution, so the p_x scale is varied (each event has 3 MeV added to it in data only) as well as the p_y scale (6 MeV), which considerably overestimates the resolution of this alignment step. The slope changes at most 1% when p_y is adjusted.

In order to test the reconstruction, the χ^2 cut was doubled in data and Monte Carlo, causing a 1% change in the slope and a slightly larger change in normalization.

In order to test the effect of poor placement of beam pipe apertures in the Monte Carlo, the d_{pipe} cut was changed so that tracks had to miss all beam pipe elements by at least 1 mm. This changed the slope by 10% and normalization -7%, one of the most substantial systematic checks. This systematic could be better controlled with a more accurate Monte Carlo; in this case, the cut changes only the data selection and does not affect the selection of Monte Carlo events.

Monte Carlo systematic checks

Since the initial distribution of diffractive events is not exactly known, the RAP-GAP Monte Carlo is reweighted to test different possible generated distributions which could also have described the data set observed.

The α_{P} value in particular is not well known and is varied from the generated value of 1.09 to 1.19 by applying weights, resulting in less than 2% change. The α'_{P} value was adjusted to 0, resulting in a small change in normalization.

The generated b_0 value was changed to 4.4 in making this measurement; it is adjusted to 3.5 and 5.5 as systematic checks. The changes were about $\pm 5\%$ in the slope. Using Nikolaev-Zakharov in place of RAPGAP had a 10% effect on the slope and considerable influence on the normalization, probably due to the considerably different generated t distribution in this model.

To check the effect of beam halo, the normalization of the beam halo monte carlo was increased by a factor of 8, causing a small change in the slope but a larger change to the normalization. The $E + p_x$ cut was increased to 1680, with little change.

Background subtracting π^0 and double diffractive samples had a very small effect on the reconstructed values, and adjusting the x_L cut to 0.96 similarly had little effect.

The total systematic error for b was obtained by adding the differences between nominal and check values in quadrature, with the result $b = 6.6 \pm 0.6^{+1.2}_{-0.6}$, completely compatible with the results in [121]. The normalization uncertainty is determined by combining changes from the total cross section in quadrature. The poor simulation of the LPS and rear beam pipe lead to an estimated $\pm 35\%$ normalization uncertainty.

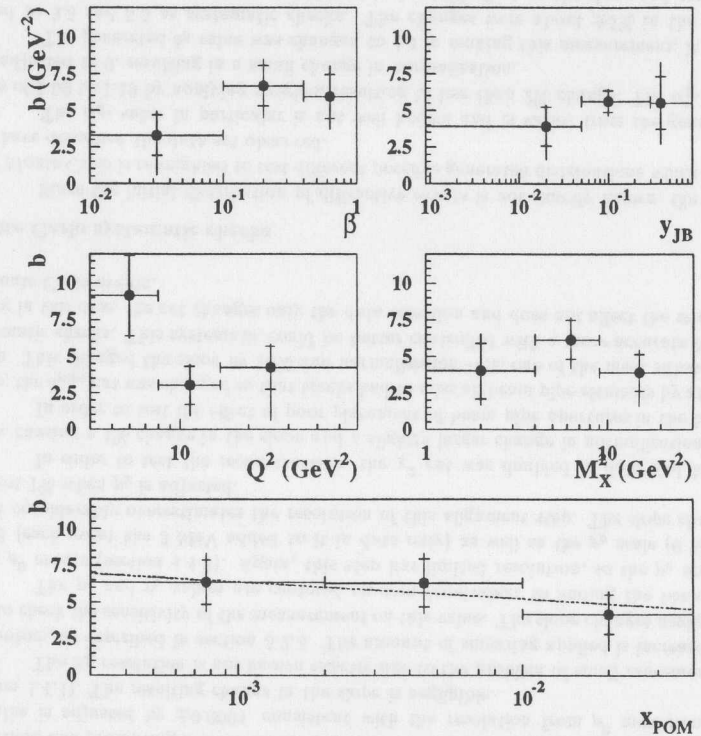
Criteria	β	Q^2	x_P	M_X	y_{JB}
Boundaries	.01, .1, .4, 1	4, 8, 16, 60	.0003, .002, .01, .04	0.4, 9, 30	0.05, .3, .9
Special cuts				no y_{JB}	no y_{JB}
(Purity) t +var	30%	33%	32%	31%	34%
(Purity) var only	70%	76%	73%	73%	78%
χ^2 /DOF bin 1	1.5/2	4.3/2	0.4/2	3.4/2	4.4/2
χ^2 /DOF bin 2	0.3/2	0.9/2	4.8/2	6.0/2	4.5/2
χ^2 /DOF bin 3	6.5/2	0.5/2	1.4/2	2.9/2	1.1/2
b value bin 1	$3.3 \pm 1.4^{+2.3}_{-0.8}$	$9.1 \pm 2.7^{+1.0}_{-3.3}$	$6.3 \pm 1.5^{+1.3}_{-1.3}$	$4.0 \pm 1.9^{+1.3}_{-1.7}$	$3.9 \pm 1.3^{+1.9}_{-0.6}$
b value bin 2	$6.7 \pm 1.4^{+1.8}_{-1.2}$	$3.0 \pm 1.3^{+1.6}_{-0.5}$	$6.3 \pm 1.6^{+1.4}_{-1.2}$	$6.1 \pm 1.3^{+1.5}_{-0.7}$	$5.6 \pm 0.7^{+1.7}_{-0.4}$
b value bin 3	$5.9 \pm 1.5^{+1.7}_{-1.5}$	$4.2 \pm 1.5^{+3.3}_{-0.8}$	$4.1 \pm 1.3^{+2.0}_{-0.8}$	$3.9 \pm 1.3^{+1.9}_{-1.0}$	$5.5 \pm 1.8^{+2.2}_{-2.1}$

Table 7.2: Information about fits to t distributions in bins of physics variables.

7.4.3 t in bins of physics variables

The next step has been to look for a correlation or dependence of t with other physics variables, using the same basic procedure as the previous section. Some summaries of the fit results are shown in table 7.2. For each variable, the data are divided into 4 bins in t and 3 bins in another variable. The purity for the t and variable bins is shown on the first line describing the purity. The second line describes the purity of the bins before the t divisions are included. The systematic checks described in section 7.4.2 to obtain the systematic errors shown. Since this analysis depends on an accurate simulation of the LPS, this analysis was performed only on the 1994 data.

Unfortunately, the statistics are too small to identify patterns in the data, as shown in figure 7.6. The Q^2 distribution is somewhat interesting, but consistent with a statistical fluctuation. All of the fits are consistent with a universal, constant slope. In the bottom plot, the t slope appears to be decreasing as x_P falls, consistent with the soft Pomeron expectation shown by the line. α'_P is constrained to be $0.3 \pm 0.3 \pm 0.4$ by the last plot, assuming a model such as [29] This value is not statistically different from zero.

Figure 7.6: Fits to the t distribution in bins of β , y , Q^2 , M_X^2 , and x_{POM} .

7.5 Non-diffractive M_X distribution

One problem in previous determinations of diffraction without tagging events with a leading proton has been the determination of the distribution of non-diffractive events in the diffractive physics variables. In particular, previous analyses [51] have attempted to determine the non-diffractive distribution from a fit to the M_X distribution in W and Q^2 bins. This section attempts to verify the procedure used to determine background results using the LPS data. The tube fragmentation model (section 2.1.1) provides a simplistic framework for discussing the fragmentation of DIS events. Since this discussion involves predictions in the central detector region, the difference between pseudorapidity and rapidity is negligible.

According to the tube model, the probability that a particle will be produced within a region $\delta\eta$ is constant, and can even be calculated from the mean multiplicity. Assuming that there is one neutral particle for every 2 charged particles,¹ the measurements of [122] have shown that $dN/d\eta = 2.55$ –3.2 particles per unit of pseudorapidity for the W range at ZEUS. Since the backgrounds to diffractive measurements arise primarily from fluctuations in the fragmentations in which a rapidity gap happens to occur, a simple calculation of their probability follows: The probability that no particles happen in a region $\delta\eta$ is the Poisson probability that 0 particles are observed when N are expected, where $N = \delta\eta dN/d\eta$. Then the probability of observing a gap $\delta\eta$ is simply:

$$P(\delta\eta) = \exp\left(-\delta\eta \frac{dN}{d\eta}\right) \quad (7.5)$$

The value of $dN/d\eta$ here must be the *uncorrelated* probability density for particles; over small η ranges, correlations have been observed, possibly due to the decay of resonant states. Thus, the effective $dN/d\eta$ is smaller than the scaled charged particle multiplicity mentioned above.

It may be more convenient experimentally to determine the experimental background using other variables than η . In fact, the coarse segmentation of the ZEUS calorimeter, as well as the nature of hadronic energy deposits, prohibit the direct observation of $dN/d\eta$. In [51], the background was determined as a function of $\log M_X$. However, the background could be better described as a function of $\kappa \equiv E + p_z$ measured in the central detector, a variable defined for this discussion as κ . This variable has the advantage that essentially all events without any rapidity gap have the same κ value, whereas the $\log M_X$ distribution has a peak which shifts with W . However, the value of $\log(M_X/W)$ does not shift with W ; experimentally,

$$\frac{M_X^2}{W^2} = \frac{E^2 - p_z^2 - p_T^2}{(E - p_z) * 2E_p} \quad (7.6)$$

$$= \frac{\kappa}{2E_p} - x(1-y) \quad (7.7)$$

which for the small x values at HERA is effectively $\kappa/2p$. The energy sums are defined in equations 6.2–6.6. Thus, an exponential distribution in $\log \kappa$ would have an identical

¹For a final state dominated by π particles, isospin arguments suggest that π^+ , π^0 and π^- should be produced in equal quantities. However, measurements of $dN/d\eta$ have only looked at the charged particles, so an extrapolation must be made to include neutrals.

slope as a distribution of $\log M_X^2/W^2$, which for a narrow W bin would be identical to the distribution of $\log M_X^2$.

Using the tube model to extract the expected κ distribution involves summing the κ of all final particles which hit the detector. These particles have pseudorapidity values between η_{\min} and η_{\max} ; so the resulting κ value is:

$$\kappa(\eta_{\min}, \eta_{\max}) = \sum_i E_i (1 - \cos \theta_i) \quad (7.8)$$

$$= \int_{\eta_{\min}}^{\eta_{\max}} \int_0^{\infty} E(\eta, k_T) [1 - \cos \theta(\eta)] \exp\left(\frac{-k_T^2}{\langle k_T^2 \rangle}\right) dk_T d\eta \quad (7.9)$$

$$= \int_0^{\infty} k_T \exp\left(\frac{-k_T^2}{\langle k_T^2 \rangle}\right) dk_T \int_{\eta_{\min}}^{\eta_{\max}} e^{\eta} d\eta \quad (7.10)$$

$$= \langle k_T \rangle (e^{\eta_{\max}} - e^{\eta_{\min}}) \quad (7.11)$$

For η values used in this analysis, η_{\min} in equation 7.11 is small enough that $\exp(\eta_{\min})$ can be ignored. Thus, if every event filled the η spectrum up to the maximal value, then every event would have an identical κ value.

For physical event shapes, in which the final state can include a fluctuation which produces a rapidity gap, the observed κ could be smaller:

$$\frac{dN}{d \log \kappa} = \frac{dN}{d\eta_{\max}} \frac{d\eta_{\max}}{d \log \kappa} \quad (7.12)$$

$$= \exp\left[\frac{dN}{d\eta} (\eta_{\max} - \eta_{\text{det}})\right] \quad (7.13)$$

$$= \exp(a_{nd} + b_{nd} \log \kappa) \quad (7.14)$$

Equation 7.14 adopts the notation of [51], and in particular, b_{nd} should be equal to $\frac{dN}{d\eta}$ for uncorrelated particle production. The parameter a_{nd} would be hard to define, but physical factors which define it include the detector cutoff in η , the average transverse momentum produced during fragmentation, and possibly detector response as well. Thus, fragmentation effects alone should produce an exponential dependence to $\log(E + p_z)$ with a dependence proportional to the average number of uncorrelated particles per unit of pseudorapidity.

Previous measurements have observed a shallow power dependence, $b_{nd} = 1.46 \pm 0.04$ [51]. However, this observation is based on a complex fit including a simple parameterization for the expected diffractive M_X distribution. Since the goal is to measure the diffractive structure, it would be better to use actual data for the shape of the non-rapidity gap events rather than a parameterization. The LPS data provide this opportunity.

Here, the solution for determining this power-law parameter is to plot the κ values for a large number of DIS events, and for events with a leading proton. For these events, the acceptance is parameterized and each event is weighted for the acceptance of a proton with that x_L value. A fit is performed with 3 parameters: the slope and offset for the power κ behavior, and the normalization of the acceptance-corrected LPS data. The LPS data is allowed to have free normalization since some proton dissociation is also expected to produce some low-mass events, but probably with the same κ distribution as the single-diffractive events.

The fit predicts a form for the non-diffractive κ distribution with $b_{nd} = 1.98 \pm 0.16^{+0.20}_{-0.13}$. A variety of systematic checks ensure that the above value is accurate. The

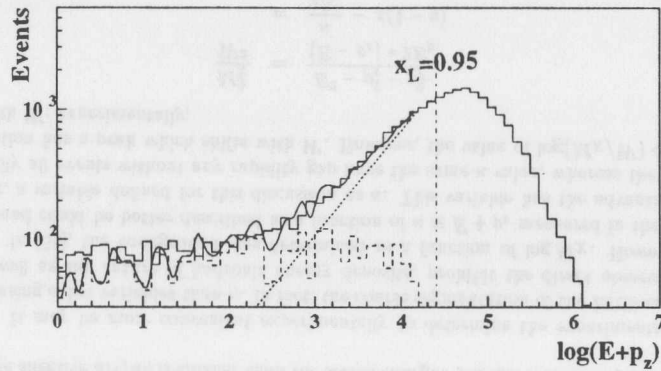


Figure 7.7: Fit to the observed $E + p_z$ distribution for $8 < Q^2 < 25$.

dominant systematic comes from varying the cutoff point for the fit, although using ZUFOS also increased the observed slope considerably. Other systematics included: varying the LPS acceptance shape; omitting the LPS acceptance corrections altogether; varying the x_L cutoff to 0.94 and 0.96; using cells instead of hybrids; fitting M_X^2/W^2 instead of κ ; and including the electron in calculation of κ . A further test omitted all events with a hit in the PRT, and performing the same sort of fit. While the normalization of the LPS contribution dropped by a factor of 10, the slope remained exactly the same. These tests give confidence that this measurement accurately reflects the uncorrelated rate of particle production during fragmentation.

The normalization of the LPS contribution corresponds to $1.25 \pm 0.15 \pm 0.20$. This suggests that a proton dissociative contribution of about 25% is included in the low-mass sample. This agrees with previous calculations of the contribution of proton-dissociative events.

The b_{nd} value found above is much larger than the value obtained in reference [51] of 1.46 ± 0.15 , a 2σ discrepancy. This difference presumably results from the fixed parameterization of the diffractive contribution as well as the fact that in [51] the fits are made to the $\log M_X$ distribution instead of $\log \kappa$. While the physics requires that the actual slopes be identical in both cases, the practical issues of fitting this slope in W bins could change the resulting fits.

The analysis of [51] has a high degree of sensitivity between the b_{nd} value used for background subtraction and the resulting α_P values [123]; a change in α_P of 0.1 should be expected for this discrepancy of b_{nd} , for the M_X bin between 3 and 7.5. Care should be exercised when considering the results of any analysis which depend on the subtraction of non-diffractive background; the analysis presented in this section indicates that the conclusions drawn in reference [51] are incorrect. Moreover, further analysis using this technique should be questioned if the b_{nd} value is set much smaller than 2.

Chapter 8

$F_2^{D(4)}$ Analysis

A primary objective in this analysis is measuring the probability that a diffractive event would be observed with final state variables β, Q^2, x_F, t . This probability is most efficiently expressed in terms of the structure function $F_2^{D(4)}(\beta, Q^2, x_F, t)$ (equation 2.19). This measurement requires removal of the detector effects, the process of *unfolding*, performed using the Monte Carlo. Once the bin boundaries are defined in β, Q^2, x_F, t -space, the number of events within each bin is counted and corrected to obtain the most likely F_2 value at the center of that bin which would produce the numbers of events observed. Further analysis of the significance of this result will be presented.

8.1 Unfolding

A simple unfolding method is used to determine the expected F_2 value from the generated F_2 and observed numbers of events in the data and Monte Carlo samples within one bin:

$$F_2^{meas} = F_2^{gen} \frac{\mathcal{L}_{gen} N_{obs,data}}{\mathcal{L}_{data} N_{obs,MC}} \quad (8.1)$$

This is similar to the method used in [20] to determine F_2 , commonly known as the bin-by-bin correction.

Some common parameters which describe bin quality are defined here. The *purity* is the ratio of observed events generated within a bin and observed in the same bin, to observed events generated in a bin. The *efficiency* is the fraction of events generated in a bin which are observed in the final data sample. The *acceptance*, used for the bin-by-bin correction, is the number of events observed in a bin, divided by the number of events generated in that bin.

8.2 Bin choice

Bin boundaries were chosen in β at 1.0, 0.5, 0.25, 0.1, 0.04, 0.02, and 0.008. Bins in x_F and Q^2 had to be enlarged relative to the 1993 analysis [53], so the x_F bins were doubled in size with boundaries at $\log x_F$ values -3.4, -3, -2.6, -2.2, -1.8, -1.5. One Q^2 bin

was chosen with boundaries at 5 and 20 GeV², and the single t bin spans values of -0.4 GeV² to -0.073 GeV². The β and x_F boundaries are shown in figure 8.1.

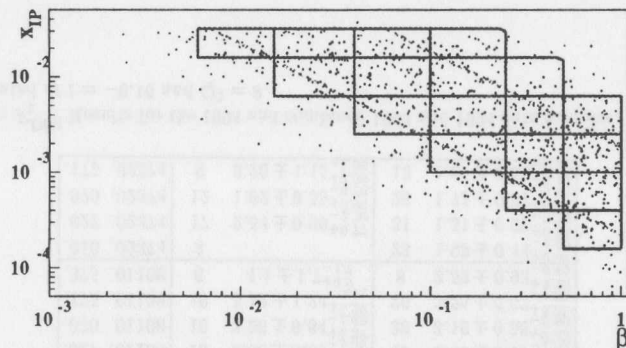


Figure 8.1: Plot of x_F vs. β for DIS events. The bin boundaries are shown by the lines.

The restrictions on y impose additional boundaries on these bins in a Q^2 dependent manner. At $Q^2 = 20$, the largest y cut defines the edge of bins at small β values, as shown by the leftmost dashed line. For $Q^2 = 5$, the bins at the upper right of figure 8.1 are further restricted, with a boundary shown by the rightmost dashed line.

Bins were rejected if the number of events or number of expected events was less than 5, bin purity was less than 30%, efficiency was less than 1%, or background was greater than 10%. Bins shown in figure 8.1 all pass these bin quality requirements.

8.3 Results

Since the simulation of the 1994 data was more robust than the 1995 sample, all results have been carefully cross-checked with the results based on 1994 data alone. No substantial differences exist between the results of the combined and 1994 samples. One minor change for the combined analysis was the change in the x_L cut to 0.95 from 0.97, in order to accommodate the reduced resolution of the S1-S2 tracking. The lowest x_F allowed into the bins remained at 0.03, however, so the measured phase space remains the same between 1994 and 1995. The β range spans up to 1, in contrast with the results of [121].

The structure function data are plotted in figure 8.2. The calculation details are shown in table 8.1. The one bin in Q^2 (from 5 to 20 GeV²) has been centered at 8 GeV²; one bin in t covers -0.4 to -0.073 GeV², and is centered at -0.16 GeV². This table shows the results for 1994 results only, and 1994 and 1995 results together. Because the combined results seem to be compatible with the 1994 only results, this section will discuss the analysis of the combined samples. Note that all further results in this chapter have been checked to be compatible with results obtained from my analysis of the 1994 data alone as well as with the results from [121].

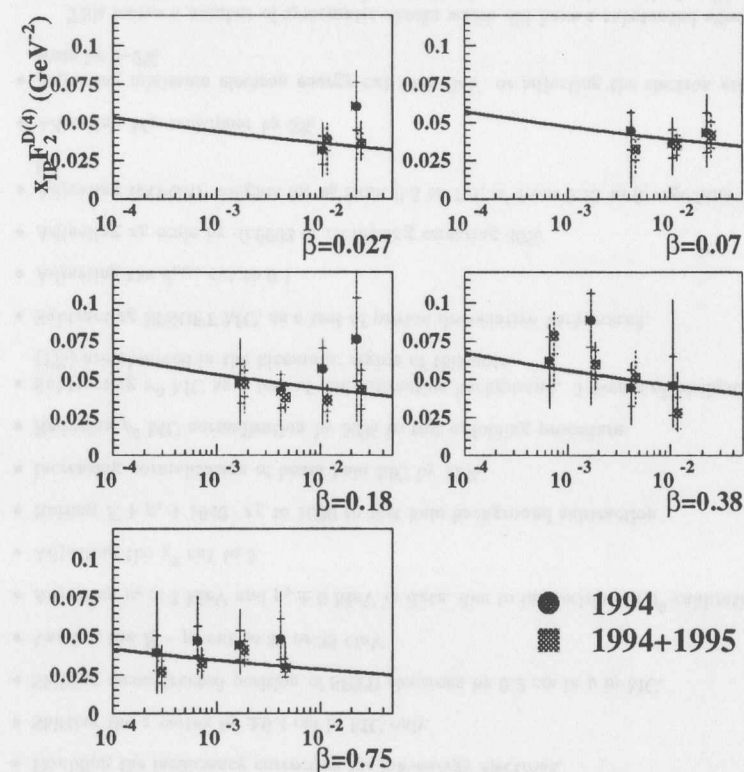


Figure 8.2: Structure function $F_2^{D(4)}(\beta, Q^2 = 8 \text{ GeV}^2, x_F, t = 0.16 \text{ GeV}^2)$ (GeV²) multiplied by x_F .

β	x_p	1994 Results		1995 Results	
		N_{cuts}	$F_2^{D(4)}$	N_{cuts}	$F_2^{D(4)}$
.750	.00028	13	$140 \pm 40^{+138}_{-82}$	15	$96 \pm 26^{+58}_{-42}$
.375	.00070	16	$88 \pm 23^{+25}_{-38}$	52	$112 \pm 17^{+16}_{-44}$
.750	.00070	27	$67.4 \pm 13.6^{+38.9}_{-26.5}$	42	$46.7 \pm 7.6^{+13.0}_{-12.1}$
.175	.00176	14	$26.8 \pm 7.4^{+16.0}_{-13.8}$	35	$26.8 \pm 4.8^{+7.5}_{-10.0}$
.375	.00176	29	$50.3 \pm 10.0^{+6.2}_{-29.1}$	15	$34.0 \pm 5.4^{+7.0}_{-7.8}$
.750	.00176	24	$25.2 \pm 5.4^{+12.0}_{-8.9}$	51	$23.4 \pm 3.5^{+6.5}_{-5.5}$
.070	.00441	14	$10.1 \pm 2.8^{+1.6}_{-7.7}$	24	$7.3 \pm 1.6^{+1.5}_{-7.2}$
.175	.00441	16	$9.5 \pm 2.5^{+1.7}_{-5.0}$	33	$8.7 \pm 1.6^{+1.8}_{-1.9}$
.375	.00441	15	$10.1 \pm 2.7^{+2.6}_{-4.6}$	31	$11.7 \pm 2.2^{+3.2}_{-3.7}$
.750	.00441	15	$10.9 \pm 3.0^{+6.5}_{-2.5}$	26	$6.70 \pm 1.39^{+3.83}_{-0.57}$
.027	.01108	13	$2.88 \pm 0.82^{+1.55}_{-1.35}$	32	$3.49 \pm 0.63^{+0.84}_{-1.03}$
.070	.01108	16	$3.26 \pm 0.84^{+1.37}_{-1.62}$	33	$3.16 \pm 0.58^{+0.32}_{-0.69}$
.175	.01108	19	$5.12 \pm 1.24^{+1.27}_{-3.01}$	26	$3.26 \pm 0.67^{+0.65}_{-1.00}$
.375	.01108	6	$4.1 \pm 1.7^{+4.9}_{-1.7}$	8	$2.52 \pm 0.93^{+2.29}_{-0.62}$
.010	.02374	3		23	$1.98 \pm 0.44^{+0.47}_{-1.02}$
.027	.02374	17	$2.54 \pm 0.66^{+0.77}_{-2.30}$	31	$1.51 \pm 0.29^{+0.58}_{-0.39}$
.070	.02374	12	$1.82 \pm 0.55^{+0.95}_{-0.76}$	26	$1.75 \pm 0.37^{+0.46}_{-0.53}$
.175	.02374	9	$3.20 \pm 1.15^{+2.38}_{-1.95}$	13	$1.81 \pm 0.53^{+0.48}_{-0.32}$

Table 8.1: $F_2^{D(4)}$ Results for the 1994 and combined 1994 and 1994 data samples. All results are evaluated at $t = -0.16$ and $Q^2 = 8$.

Systematic Checks

A total of 51 systematic checks were used in this analysis, described below. Most of them had little effect on the measured cross sections, and are listed first:

- Doubling the inefficiency correction for low-energy electrons.
- Shifting the z vertex by ± 0.4 cm in MC only.
- Shifting reconstructed position of SRTD electrons by 0.2 cm in y in MC.
- Varying the $E - p_z$ cut to 32 or 38 GeV
- Adjusting $p_x \pm 3$ MeV and $p_y \pm 6$ MeV in data, due to imprecision of ρ^0 calibration.
- Adjusting the χ^2 cut to 5.
- Raising $E + p_x + 1640 \cdot x_L$ to 1680 to test halo background subtraction
- Increasing normalization of beam halo MC by 12%
- Reducing ρ^0 MC normalization by 50% to test unfolding procedure.
- Subtracting π^0 MC as a test of non-diffractive background. 5 events of background (1%) are observed in the kinematic region of this note.
- Subtracting EPSOFT MC, as a test of proton dissociative background.
- Adjusting the d_{pipe} cut to 0.1
- Adjusting x_L scale by -0.0003 or increasing smearing 30%
- Adjusting RAPGAP weights for b_0 from 0.5 to 7.5, α' from 0.25 to 0, α_p from 0 to 0.1
- Adjusting M_X multiplier by 5%
- Adjusting minimum electron energy cut to 8 GeV, or adjusting the electron energy scale by 1-2%

This leaves a number of systematic checks which did have a substantial effect on the cross sections. The largest effects come from hadronic reconstruction methods, although the Monte Carlo is also quite important.

- The source of hadronic information (ZUFOS, hybrid objects, or calorimeter cells) had a considerable influence on the cross section and fitted quantities. Large fluctuations were observed as reconstructed events shifted between bins. Using the Triple Angle formula had similarly large effects. Somewhat smaller effects were observed when the LPS was not used in reconstruction of x_p or β . Changing hadronic reconstruction also slightly changed fitted variables such as the x_p slope.
- Substituting the Σ DIS variable reconstruction technique [116] considerably changed the results and lowered the fitted x_p slope by 5%.

- Adjusting the M_X multiplier $\pm 5\%$ had a small effect on the cross section. This really is only a test of the unfolding, since the multiplier was changed in both data and Monte Carlo.
- The y_{JB} cut was varied to 0.02 and 0.04. Either change had a moderate effect, apparently due to poor the Monte Carlo description of low- y_{JB} region, changing cross sections by as much as 1σ .
- Adjusting the hadronic energy scale by 5% had a very small effect.
- Using a 12cm box cut instead of 13cm had a very small effect on the cross section.
- Requiring reconstructed vertex had a small effect.
- Adjusting the SINISTRA probability cut to 0.5 had a tiny effect
- Varying the LPS x_L scale $\pm 3 \cdot 10^{-4}$ had a tiny effect on the cross section.
- Reweighting RAPGAP generated b_0 to 0.5 changes the fitted slope by 0.2σ .
- Using NIKZAK for acceptance correction had a substantial effect, showing how dependent this measurement is on the Monte Carlo. Low-mass events migrated to larger masses, so the effect as a function of β is more pronounced. This systematic check dominates the lower error on a for either the 1994 alone or 1994+1995 data set; in [121], this was ameliorated by only fitting $\beta < 0.5$, removing the problematic low-mass region.
- Not using ρ MC for unfolding had a moderate effect

The normalization uncertainty, due to the poor simulation of the LPS, remains $\pm 35\%$ (determined in section 7.4).

8.4 Analysis of $F_2^{D(4)}$

8.4.1 Determination of α_P

An important result for the structure function is the x_T dependence of the structure function. However, the best method of obtaining this dependence is not clear. In particular, the assumptions which are made about the β dependence influence the result slightly. The first approach is to assume that each β bin has an independent x_T power dependence and an independent normalization. Results of fits to the five β bins are shown in figure 8.3, where Poisson minimization is used due to the low statistics available. In the figure, the shaded bands indicate the statistical and the statistical plus systematic errors from the fit where all slopes are constrained to be the same value.

These figures suggest that one universal x_T dependence will describe the structure function. However, there is still the question of how to make this fit while considering the β dependence. I consider four possibilities for the structure function's β dependence:

1. The normalization of each bin in β is a free parameter to be determined by a fit

β	Slope	N bins
.070	$0.85 \pm .17^{+.18}_{-.28}$	3
.175	$1.08 \pm .12^{+.15}_{-.18}$	4
.375	$1.30 \pm .11^{+.09}_{-.27}$	4
.750	$0.95 \pm .10^{+.13}_{-.28}$	4

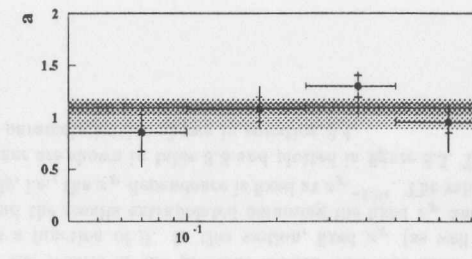


Figure 8.3: Fits to x_T dependence of structure function fit independently in each β bin.

2. The normalization of each bin in β is constant:

$$F_2^{D(4)} = n x_T^{-a} e^{bt} \quad (8.2)$$

3. The β dependence has the same form as was used in the 1993 analysis (equation 5.1 with c a free parameter), also known as the *hard+soft* structure function.

4. A *Hard* structure function is used

$$F_2^{D(4)} = n x_T^{-a} \beta (1 - \beta) e^{bt} \quad (8.3)$$

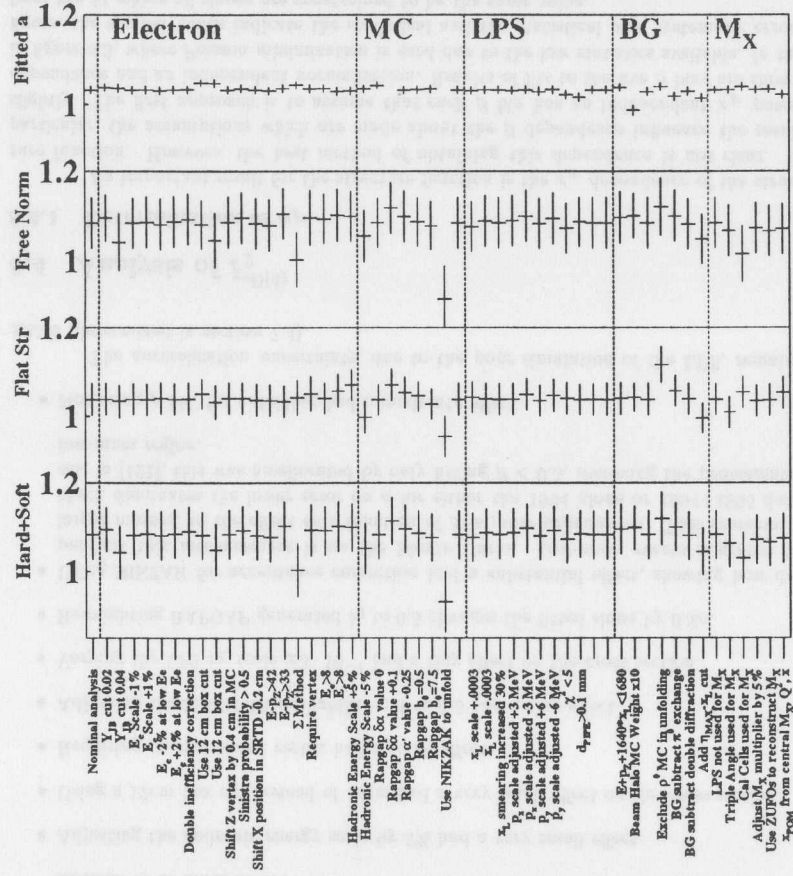
Furthermore, one can choose to use the more conventional χ^2 statistics to minimize for the fit, or the more appropriate Poisson statistic. Maximizing the Poisson probability will give better accuracy for this low statistic sample.

The results of the x_T power a are shown for these eight combinations in table 8.2, while fits independently for each β value appear in figure 8.3. The changes caused by the systematic check are shown in figure 8.4; clearly the NIKZAK Monte Carlo for unfolding dominates the uncertainty in the result for a , because of poor description of the low mass events.

The dominant systematic effect comes from the choice of hadronic information, either ZUFOS or calorimeter cells dominate the systematic errors quoted above. Using the electron method, unfolding with NIKZAK, and selecting a different y_{JB} cut have smaller consequences. Other systematic changes had less than 2% effect on a .

Clearly the hard structure function fails to describe the data, since the probability is less than .01%, confirming the conclusion reached from the 1993 data [53]. Allowing the structure function within each bin to vary freely has the disadvantage that the errors are somewhat larger.

The fit which determined the hard and soft components of the structure function

Figure 8.4: Systematic checks on x_P slope

β dependence	x_P slope		Minimum
Structure Function	Poisson statistics	χ^2 statistic	χ^2/DOF
Free in each bin	$1.084 \pm .06^{+0.07}_{-0.21}$	$1.096 \pm .06^{+0.08}_{-0.24}$	12.9/12=1.1
Constant	$1.04 \pm .035^{+0.10}_{-0.11}$	$1.00 \pm .04^{+0.13}_{-0.11}$	28.7/16=1.8
Hard+Soft	$1.083 \pm .06^{+0.07}_{-0.29}$	$1.08 \pm .05^{+0.09}_{-0.19}$	17.8/15=1.2
Hard	$0.69 \pm .04^{+0.11}_{-0.10}$	$0.89 \pm .05$	103/16=6.6
Monte Carlo Reweight	$1.03 \pm .03^{+0.08}_{-0.05}$		

Table 8.2: Methods of obtaining x_P dependence

β	$F_2^{D(4)}(\beta, Q^2 = 8 \text{ GeV}^2, x_P = 0.001, t = -0.16 \text{ GeV}^2)$
0.015	$61.1 \pm 14.4^{+14.5}_{-12.7}$
0.028	$46.9 \pm 7.0^{+6.5}_{-6.0}$
0.07	$43.4 \pm 3.9^{+2.7}_{-4.8}$
0.175	$46.6 \pm 4.9^{+4.6}_{-4.6}$
0.375	$62.4 \pm 4.8^{+4.0}_{-5.5}$
0.75	$34.2 \pm 5.7^{+3.2}_{-3.0}$

Table 8.3: $F_2^{D(4)}(\beta, x_P = 0.001, Q^2 = 8 \text{ GeV}^2, t = -0.16 \text{ GeV}^2)$ obtained assuming a universal functional dependence $x_P^{-1.084}$ and fitting to the $F_2^{D(4)}$ values presented earlier. This demonstrates the β dependence of the structure function.

shows that the structure function can parameterized as

$$F_2^{D(4)}(\beta, Q^2, x_P, t) = (539 \pm 45 \pm 190) \exp \left[\left(6.6 \pm 0.6^{+1.2}_{-0.6} \right) t \right] \left(\frac{x_P}{0.001} \right)^{-1.083 \pm .05^{+0.09}_{-0.19}} \left[\beta(1 - \beta) + \frac{0.49^{+0.13}_{-0.10} + 0.09}{2} (1 - \beta)^2 \right] \quad (8.4)$$

to within the sensitivity of the present measurement. There is substantial correlation between the overall normalization and the soft component value (88%), but less than 35% correlation between other values.

Regge-based diffractive models would interpret the x_P dependence of the structure function as a measure of α_P , with the relation $2\alpha_P(t = -0.16 \text{ GeV}^2) - 1 = a$. This value of α_P , $1.04 \pm .03^{+0.04}_{-0.10}$, strongly supports the soft Pomeron hypothesis for diffractive DIS.

8.5 Analyzing β dependence of $F_2^{D(4)}$

The method of plotting the results in the previous section does not allow for easy comparison of the results as a function of β . In this section, fixed x_P (as well as Q^2 and t) values will be chosen and the results extrapolated assuming the fixed x_P and t dependencies determined previously, i.e., the x_P dependence is fixed at $x_P^{-1.04}$. The values of $F_2^{D(4)}$ extrapolated in this manner are shown in table 8.3 and plotted in figure 8.5. The curve in this figure represents the parameterization shown in equation 8.4.

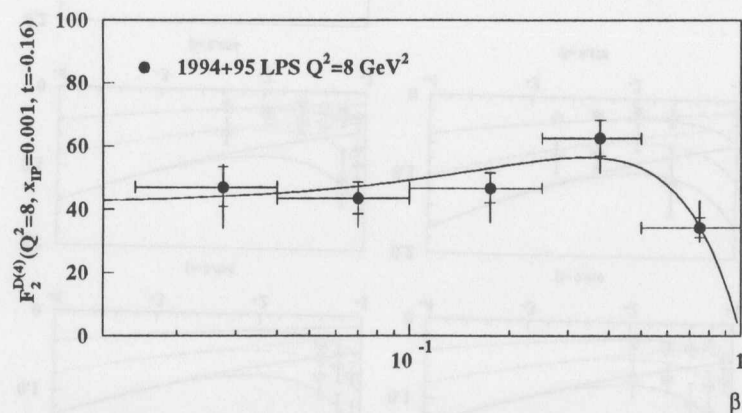


Figure 8.5: Plot of $F_2^{D(4)}(\beta, Q^2 = 8 \text{ GeV}^2, x_P = 0.001, t = -0.16 \text{ GeV}^2)$ assuming a universal functional dependence $x_P^{-1.084}$. Normalization error of $\pm 35\%$ not included.

8.6 Analysis of Reggeon Contribution

In recent analyses [68, 125], the effects of a reggeon contribution besides the Pomeron have been discussed. Since substantial changes in the physics conclusions have been attributed to Reggeon contributions, it would be inappropriate to ignore their effects in this analysis. The use of the π^0 Monte Carlo as a background subtraction in the previous section demonstrated that little change should be expected due to Reggeon exchange, but this section will attempt to verify that conclusion by making a Pomeron+Reggeon combined fit.

Data were selected as in previous sections, except that the x_L cut has been lowered to 0.9 to include more data suspected to be due to Reggeon contributions. Bins have been extended in x_P to 0.1, and the data were divided into 3 t bins. The β bins were also widened, for a total of 5 bins. Data were unfolded in the same manner as the previous section.

The resulting structure function was fitted to a two-component structure inspired by the analysis of III [125]. The structure function for the Reggeon contribution was assumed to be:

$$F_2^{R(4)} = N_R c^{B_R t} x_P^{-2\alpha_R(t)+1} \quad (8.5)$$

The Reggeon structure was assumed to be flat. The fit determined the normalization of the Reggeon contribution, with the fixed parameters $B_R = 2 \text{ GeV}^{-2}$ and $\alpha_R(t) = 0.55 + 0.9t$, as expected for the approximately degenerate ρ , ω , f , and a trajectories. This Reggeon structure was added to the hard+soft structure function to obtain new values for that fit. The x_P dependence for the Pomeron component had only a small change, to 1.15 ± 0.063 . The normalization N_R was 1.0 ± 0.15 (figure 8.6). This simple test supports the decision to ignore the Reggeon contributions besides the Pomeron in this analysis. Allowing α_R to be a free parameter did not yield stable results, however.

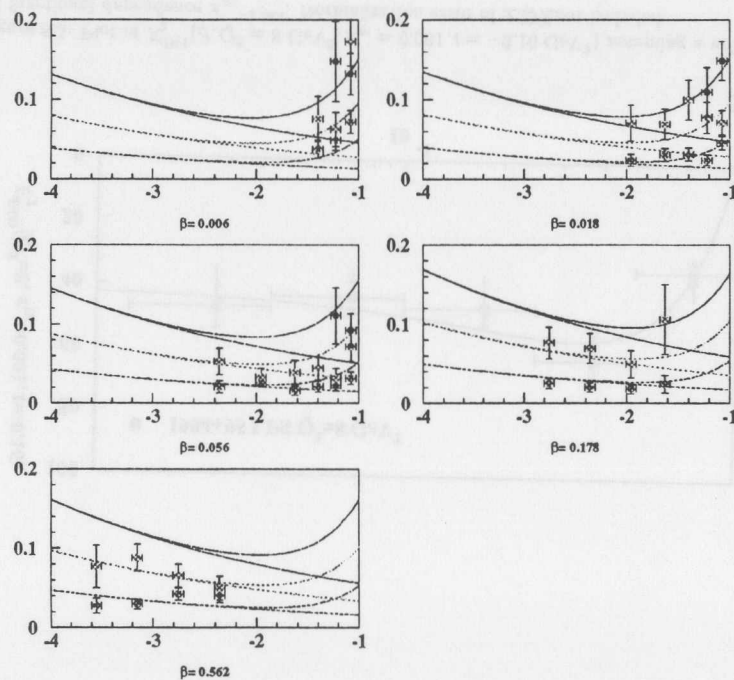


Figure 8.6: Fit of $F_2^{D(4)}$ over extended x_p range (horizontal axis). Each line indicates the fit described in the text at $t = -0.03$ (top), -0.1 , and -0.2 (bottom). For each t value, the split lines indicate the Pomeron-only contribution and the Pomeron plus Reggeon contributions.

Chapter 9

Event Shapes

Studies of high-energy collisions involving hadronic final states generally seek to understand the processes at very small scales, involving interactions between the fundamental (quark, lepton, and boson) objects. Hadronic interactions at short scales are clouded by the soft interactions involved in the process of fragmentation, during which quarks and gluons condense into showers of hadronic objects. The fragmentation process leads to loss of information over the initial parton-level states, but not all information is lost. Studying the *event shape*, the distribution of particle momenta within the hadronic final state, can reveal some of the details about the quark-level interactions [26, 27, 126].

Hadronic final states have numerous particles, and many experiments have used various techniques for summarizing the distributions of these particles. Analysis of hadronic final states led to an initial description involving *jets*, exploiting the characteristic of hadronic states to have large quantities of particles following the same momentum as the initial parton before fragmentation. In fact, an analysis of diffraction by studying jets has been shown in [127]. However, jet analysis in diffraction suffers from the low masses of the final states; this results in only a few percent of the events having features which can be identified as jets.

Additional variables have been invented to describe inclusively the event shape. The parameters which have had particular success in describing hadronic final state particle distributions at e^+e^- colliders include *thrust*, *oblateness*, *sphericity*, and *aplanarity*. Expected values for three shapes of events are shown in figure 9.1. The distributions shown are uniform, two-jet, and three-jet structures. Historically, the variables thrust and sphericity were used to establish that jet-like shapes existed in hadronic final states, and the variables oblateness and aplanarity verified the existence of the distinct class of three-jet events over the dominant two-jet events.

- **Thrust:** T is a parameter which measures how collimated the particles in an event appear. For a set of n final state particles with 3-momentum \mathbf{p}_i , $i = 1..n$, the thrust is defined using a normalized unit vector \mathbf{n} . This unit vector is varied to maximize the following formula:

$$T = \max_{\mathbf{v}_1, |\mathbf{v}_1|=1} \frac{\sum_i |\mathbf{v}_1 \cdot \mathbf{p}_i|}{\sum_i |\mathbf{p}_i|} \quad (9.1)$$

The unit vector which maximizes T is referred to as \mathbf{v}_1 . The resulting values of T have an allowed range $1/2 \leq T \leq 1$. Events with a pencil-like structure, where

all particles are nearly parallel to a common axis, have large thrust values $T \simeq 1$. Random distributions of particles have $T \simeq 1/2$.

The angle of the thrust axis, \mathbf{v}_1 , is also important.

- **Major, Minor Axis:** This parameter is calculated identically to the thrust value, except that the unit vector in this case, \mathbf{v}_2 , remains perpendicular to the thrust axis: $\mathbf{v}_2 \cdot \mathbf{v}_1 = 0$. The minor axis M_i corresponds to the unit vector \mathbf{v}_3 which satisfies $\mathbf{v}_3 \cdot \mathbf{v}_2 = \mathbf{v}_3 \cdot \mathbf{v}_1 = 0$. The parameters are defined as for thrust T :

$$M_a = \max_{\mathbf{v}_2, |\mathbf{v}_2|=1, \mathbf{v}_1 \cdot \mathbf{v}_2=0} \frac{\sum_i |\mathbf{v}_2 \cdot \mathbf{p}_i|}{\sum_i |\mathbf{p}_i|}; \quad M_i = \frac{\sum_i |\mathbf{v}_3 \cdot \mathbf{p}_i|}{\sum_i |\mathbf{p}_i|} \quad (9.2)$$

- **Oblateness:** For quantizing planar structure, oblateness has proven useful: $O \equiv M_a - M_i$. Events with $O \simeq 0$ are symmetrical about the thrust axis, and larger O values have a planar structure.

- **Sphericity:** The sphericity tensor is defined by:

$$S^{\alpha\beta} = \frac{\sum_i p_i^\alpha p_i^\beta}{\sum_i |\mathbf{p}_i|^2} \quad (9.3)$$

where $\alpha, \beta = 1, 2, 3$ correspond to the x, y , and z directions. Three eigenvectors for $S^{\alpha\beta}$ correspond to $\lambda_1 \geq \lambda_2 \geq \lambda_3$. Sphericity is given by:

$$S = \frac{3}{2}(\lambda_2 + \lambda_3) \quad (9.4)$$

This value essentially indicates the total p_1^2 with respect to the event axis. Collimated, pencil-like events have $S \simeq 0$ and isotropic events tend to have $S \simeq 1$.

- **Aplanarity:** Using the eigenvectors of the sphericity matrix, $A = \frac{3}{2}\lambda_3$. A planar event has $A \simeq 0$ and an isotropic event has $A \simeq \frac{1}{2}$.

These event shape variables, in addition to jet-finding algorithms, have been crucial for verifying predictions for gluon radiation in QCD and have been used to measure α_s . In this analysis, the hope is to be able to compare the diffractive final state with the observations of the $e^+e^- \rightarrow q\bar{q}$ reaction. Many Monte Carlo for diffractive DIS implement a simple partonic final state of two quarks, before fragmentation occurs, while various models expect a more complex final state before fragmentation. So two obvious questions can be addressed by the ZEUS data set:

1. Are the hadronic final states at a given M_X similar to e^+e^- data at $s = M_X^2$? The scale M_X is related to the scale \sqrt{s} since the both represent the invariant mass of the fragmenting system; in the e^+e^- case this system is known to be a $q\bar{q}$ state, while for diffraction the state could be something more complex.
2. Are events with different structure observed in different regions in phase space (Q^2, y, x_F, β) ?

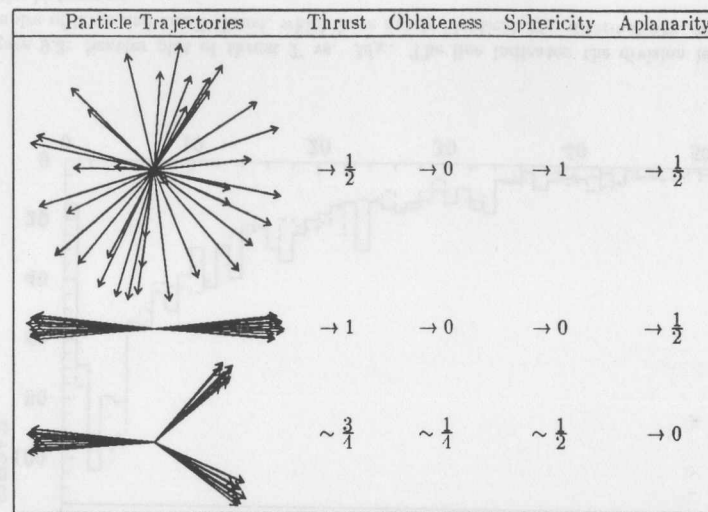


Figure 9.1: Values of event shape parameters for simple particle distributions.

In order to calculate the event shape variables for comparison with e^+e^- experiments, the center-of-mass (c.m.) frame of the hadronic final state must be used. This requires a boost of the observed particle momenta. Each observed track and calorimeter cluster is assumed to be an individual particle with mass equal to the pion mass, and the boost shifts the particles so that the sum of their momentum is zero. The photon direction, calculated from the electron position, follows the z axis after a final rotation. Figure 9.2 demonstrates this boost. The particles as observed in the laboratory frame, including the scattered electron but excluding the scattered proton, are shown for a high mass and high Q^2 event. After boost and rotation, the inclination of the thrust axis with respect to the $\gamma^* - IP$ axis, θ_{JET} can be seen.

Many experiments have relied on jet-finding methods to identify structure in final states, but this approach was avoided for this analysis because traditional jet definitions require several GeV of energy to be deposited in a small region of the calorimeter. Since the energy scales in diffractive DIS are small, only a few percent of the events can satisfy such criteria, typically events with large Q^2 and M_X . Such a selection precludes an inclusive study, and conclusions would be heavily dependent on the jet definition chosen.

9.1 Observed distributions

Monte Carlo studies indicated that reconstruction of thrust and oblateness was more accurate, on an event-by-event basis, than reconstruction of sphericity and aplanarity, so thrust and oblateness, together with the angle of the thrust axis θ_{JET} , remain the primary

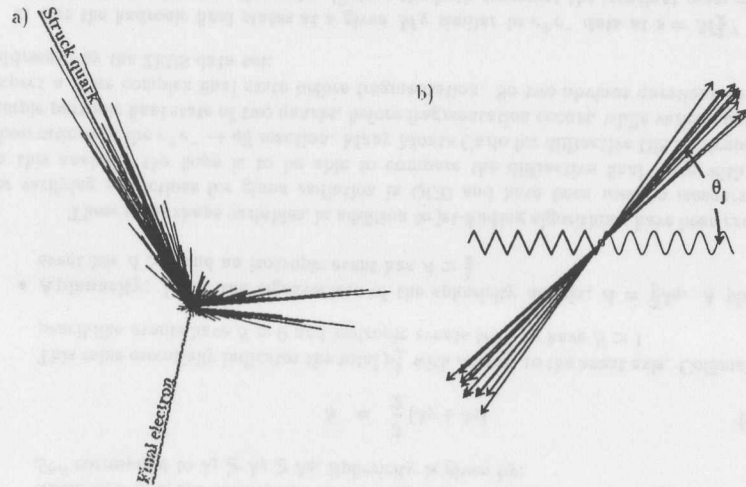


Figure 9.2: a) Example of a high- Q^2 diffractive event in ZEUS frame. b) Event after boost to $\gamma^* - IP$ c.m. frame, showing initial γ^* and IP , and final state particles with thrust axis rotated with respect to $\gamma^* - IP$ axis.

event shape variables.

To select events, the standard cuts are modified slightly, since the acceptance must not be as carefully controlled on the LPS side. The d_{pipc} cut is loosened to 0, and the box cut for 1995 data is reduced to 12×24 cm. The x_L cut was reduced to 0.95. Reconstructed thrust was required to be below 1, eliminating all 2-particle final states.

The most obvious characteristic of the event shape variables was the strong correlation with M_X , as shown in the scatter plot in figure 9.3. This characteristic leads to specific measurements in section 9.5, and was expected from the change in thrust in e^+e^- experiments. A preliminary analysis, before analyzing the mass behavior, was to search for other variables upon which the thrust depends. First, the data were divided into two samples, high-thrust and low-thrust, by making a M_X -dependent cut on the observed thrust. The line on figure 9.3 indicates this cut. The M_X distributions for the two samples were identical after this cut, which means that diffractive variables can be investigated without worrying that changes in thrust values occur only due to kinematic effects.

With the two data samples, the distributions of observable variables is presented in figure 9.4. Based on the Kolmogorov-Smirnov test, no statistically significant differences between the two data sets can be observed. One particularly interesting possibility would be that the events with large- β would be more likely to have larger thrust than smaller- β events, as suggested by Nikolaev-Zakharov (section 2.4.2). However, the small mass values available in the present data sample make thrust measurements unreliable,¹ and no

¹Multiplicity of low-mass systems are low enough that 2- and 3-particle final states are common; these

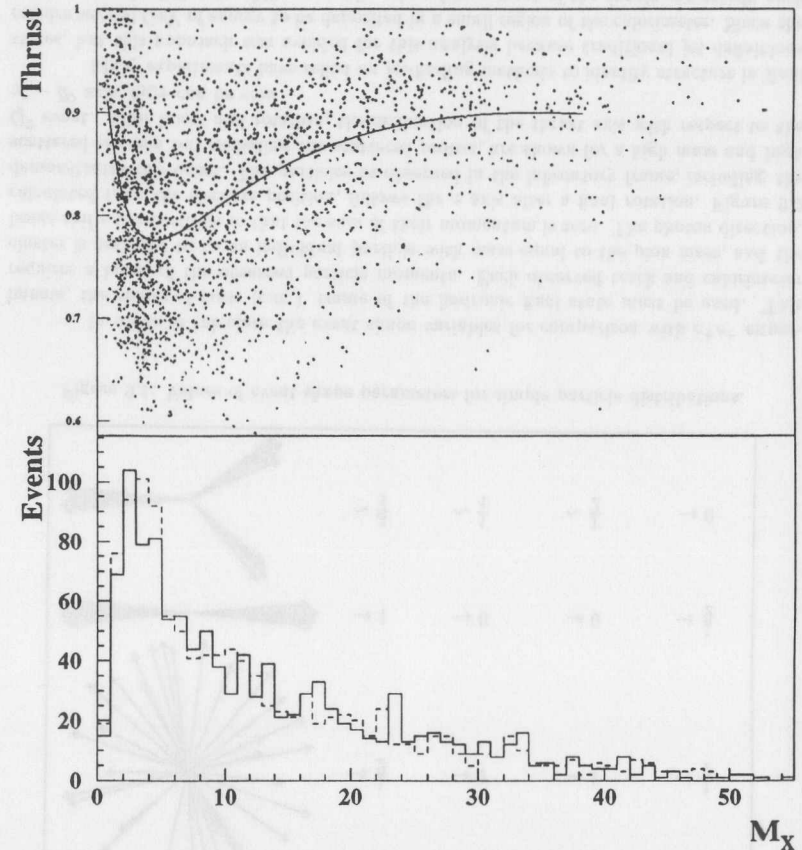


Figure 9.3: Scatter plot of thrust T vs. M_X . The line indicates the division into two samples of large and small thrust, which have nearly identical M_X distributions, as shown in the histograms.

significant difference is observed.

9.2 Fragmentation Monte Carlo

One requirement for making any measure of the final event shape is an accurate reconstruction. Since the reconstruction of thrust, oblateness, and θ_{JET} require accurate reconstruction of event variables and an accurate boost, good resolution is difficult. However, a comparison of Monte Carlo values shows that a fair amount of information from the generated thrust, oblateness, and θ_{JET} carries through to the reconstructed values, including the boost obtained from the hadronic system and final electron. Resolution appears to improve with increasing M_X , as shown in figure 9.5.

Three Monte Carlo sources have been examined to shed additional light on the final state fragmentation for the diffractive event sample. The standard RAPGAP sample fragments all final states as a $q\bar{q}$ state. A second RAPGAP sample has been used for this analysis, which has three substantial changes. First, the simulated structure function is different. This Pomeron structure function has been tuned to match the measurement of H1 [125]. Second, the final state for the $q\bar{q}$ has additional transverse momentum, which makes the generated thrust axis less aligned to the γ^*IP axis. Third, Boson-Gluon-Fusion events are simulated in this version, leading to a final state of the type $q\bar{q}g$. These events are more likely at higher- Q^2 due to evolution of the Pomeron structure function. At fixed Q^2 , however, the BGF events are distributed similarly to the expectations of Nikolaev and Zakharov, more likely at low β .

The third source of Monte Carlo actually represents three distinct processes using the VBYL model [128]. One distinct characteristic of this Monte Carlo is the distribution of θ_{JET} , which displays a nearly uniform distribution of the thrust axis. In contrast, both the Nikolaev-Zakharov model and any model describing the Pomeron-photon interaction as being like DIS, would predict that the thrust axis should be closely aligned to the Pomeron-photon axis in the Pomeron-photon c.m. frame. Three final states are considered, $q\bar{q}$ and a first-order correction, $q\bar{q}g$ with the gluon radiated from the quark. An additional interaction between the Pomeron and a gluon leads to a gg final state, which interacts with the photon via an intermediate quark. These three models can either be considered independently, or mixed according to weights determined in [129].

The LPS data are binned in M_X and Q^2 in order to investigate how the event shape variables appear in these two bins. First, the average thrust variables are compared with the average values obtained using the Monte Carlo samples. The averaged measurements for thrust, oblateness, and angle of the thrust axis are plotted in figure 9.6. From this comparison, the RAPGAP with BGF clearly describes the observed distributions better than any other Monte Carlo sample. This is verified using a χ^2 test between the data and Monte Carlo samples, shown in table 9.1.

One discrepancy can be clearly seen in the comparison with the generated thrust and oblateness distributions when compared with the e^+e^- data for thrust and oblateness, as shown in figure 9.7. Although the RAPGAP sample expects the fragmentation to proceed identically to a $q\bar{q}$ final state at a given M_X , the resulting event distributions clearly do not agree with the e^+e^- data. This suggests that the fragmentation Monte Carlo have not

states tend to have thrust near 1. Multiplicity requirements bias this distribution further.

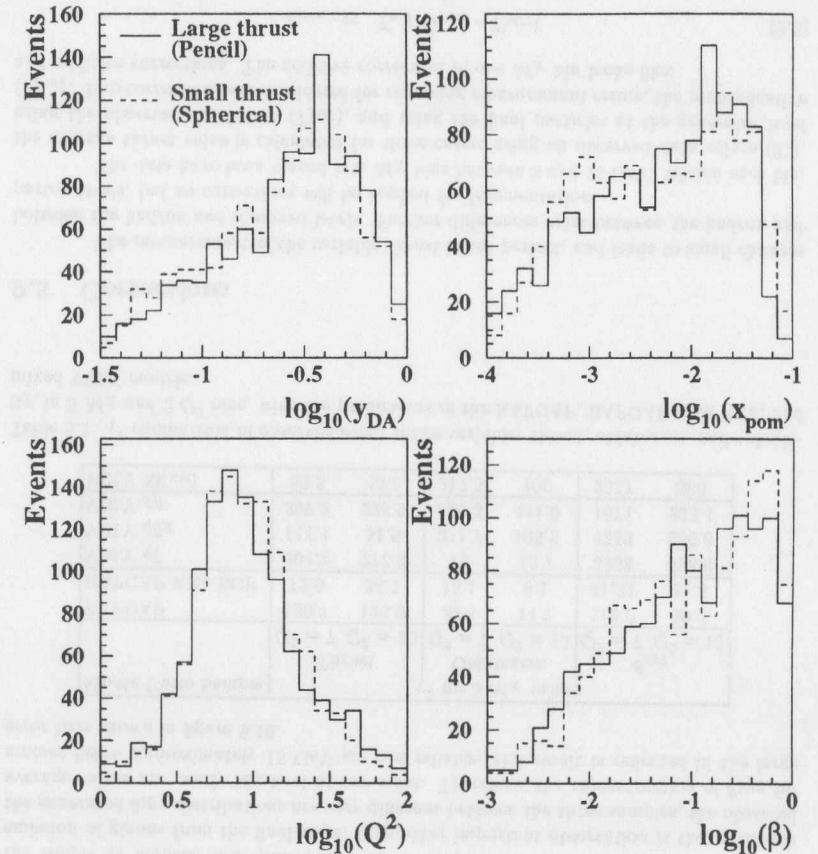


Figure 9.4: Uncorrected distributions of physics variables, for events selected as having large (solid line) and small (dashed line) thrust values.

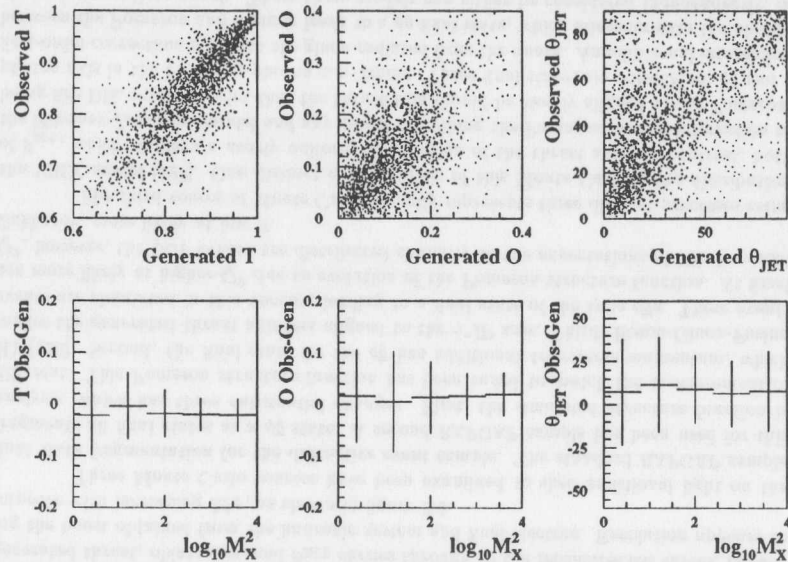


Figure 9.5: Resolution of event shape variable reconstruction. On top, scatter plots of generated vs. reconstructed thrust, oblateness, and θ_{JET} . The bottom row shows the RMS difference between the generated and reconstructed values as a function of the hadronic mass.

been tuned appropriately to simulate this process. Thus, although the fragmentation model with the extra gluon emission in the final state is clearly supported by the data better than the simple $q\bar{q}$ models, this cannot be used to support any conclusions about the actual emission of gluons from the final state. One other important observation is that although the generated θ_{JET} distributions are very different between the three samples, the observed average values are nearly identical at low mass. Therefore, the reconstruction of θ_{JET} for masses below approximately 15 GeV are not reliable; this result is reflected in the large error bars shown in figure 9.10.

Monte Carlo Sample	Thrust		χ^2 for 5 M_X values		θ_{JET}	
	$Q^2 = 7$	$Q^2 = 15$	$Q^2 = 7$	$Q^2 = 15$	$Q^2 = 7$	$Q^2 = 15$
RAPGAP	130.7	126.3	32.4	14.7	118.2	59.4
RAPGAP with BGF	72.9	35.7	15.1	8.1	41.31	21.5
VBLY $q\bar{q}$	264.9	277.6	12	15.7	3263	398.8
VBLY $q\bar{q}g$	144.4	51.9	371.7	193.8	4552	666.0
VBLY gg	397.2	228.9	559.3	444.0	1671	235.4
VBLY Mixed	89.8	43.8	217.5	109	2557	380

Table 9.1: χ^2 comparison of observed event shape variables thrust, oblateness, and sphericity, in 5 M_X and 2 Q^2 bins, with the predictions of the RAPGAP, RAPGAP with BGF, and mixed VBLY models.

9.3 Corrections

The measurement of the variable thrust is not perfect, and leads to small changes between the hadron and observed levels. Further differences exist between the hadron and parton levels, but no corrections will be applied for fragmentation.

The data have been binned into M_X bins between 3 and 25 GeV. Within each bin, the average thrust value is calculated for three cases: using all observed data values (T_o), using the observed simulation (T_{MC}), and using the final particles at the generator level (T_{gen}). Two corrections are considered for removing measurement errors, the multiplicative and additive corrections. The additive correction to one M_X bin looks like:

$$T_{corr} = T_o + (T_{gen} - T_{MC}) \quad (9.5)$$

while the multiplicative correction is:

$$T_{corr} = \frac{T_o T_{gen}}{T_{MC}} \quad (9.6)$$

Thrust and oblateness are corrected using the multiplicative correction, and the additive correction provides a systematic check. The jet angle data had lower systematic errors when the additive correction was used, so the multiplicative correction is used as a systematic check. The average observed values in data and Monte Carlo, as well as the average generated values, are shown for M_X bins bounded at 3.2, 10, 17.3, 25, and 50 GeV,

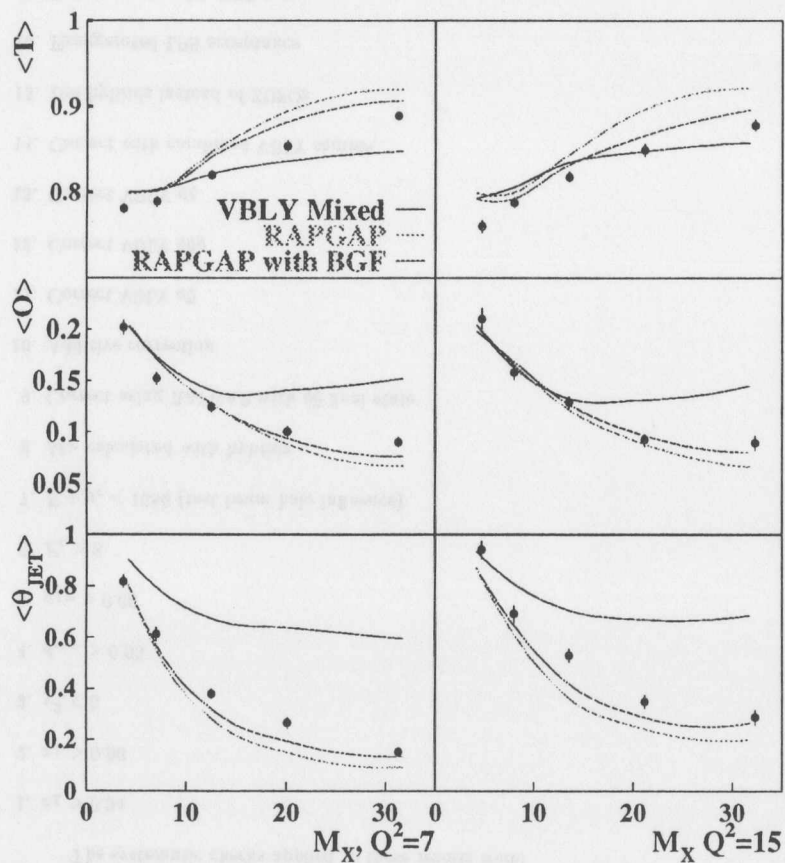


Figure 9.6: Comparison of average thrust values in bins of M_X and Q^2 with two RAPGAP and the VBLY predictions.

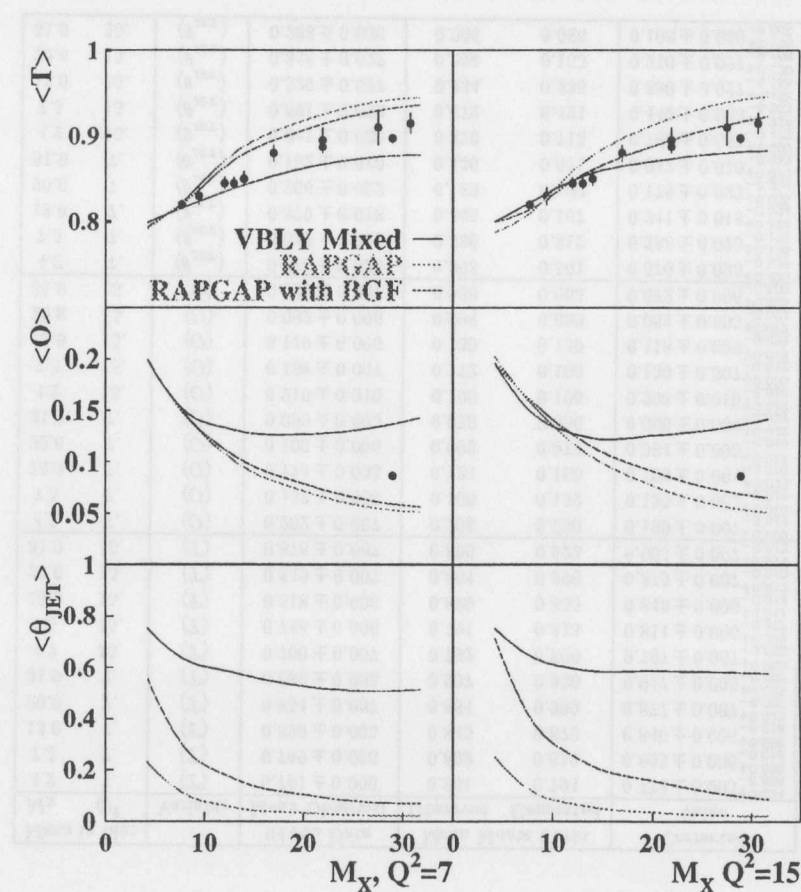


Figure 9.7: Comparison of generated event shape variables for the two RAPGAP samples and the VBLY mixed sample. All data points shown are analysis of e^+e^- [131].

and Q^2 bins from 3–10 and 10–40 GeV^2 . Observed values and corrections can be seen in table 9.2.

The systematic checks applied to these results were:

1. $x_L > 0.94$
2. $x_L > 0.96$
3. $\chi^2 < 6$
4. $d_{\text{pipe}} > 0.05$
5. $y_{JB} > 0.06$
6. $E_c > 8$
7. $E + p_z < 1680$ (test beam halo influence)
8. M_X calculated with hybrids
9. Correct using RAPGAP with $q\bar{q}$ final state
10. Additive correction
11. Correct VBLY $q\bar{q}$
12. Correct VBLY $q\bar{q}g$
13. Correct VBLY gg
14. Correct with combined VBLY sample
15. Use hybrids instead of ZUFOS
16. Exaggerated LPS acceptance
17. Reject events with PRT tag
18. Reject events with $x_T > 0.02$

The influences of these systematic checks on the 30 corrected values are shown in figure 9.8. For the variable θ_{JET} , the most significant systematic influence is the difference between the VBLY and RAPGAP MC, which assume substantially different angular distributions for the thrust axis. The differences between the Monte Carlo also dominate the systematic effects in the other variables. The differences in the VBLY Monte Carlo are the primary source of the large systematic error on the oblateness results.

Mean in bin:		Variable	94+95 Data	Mean Monte Carlo		Corrected
M_X	Q^2		Mean Observed	Observed	Generated	Value
4.2	7.	(T)	0.781 ± 0.006	0.801	0.794	$0.774 \pm 0.005^{+0.014}_{-0.008}$
7.5	7.	(T)	0.789 ± 0.006	0.803	0.819	$0.805 \pm 0.006^{+0.009}_{-0.019}$
13.0	7.	(T)	0.820 ± 0.005	0.845	0.872	$0.846 \pm 0.006^{+0.008}_{-0.018}$
20.6	7.	(T)	0.854 ± 0.007	0.884	0.909	$0.877 \pm 0.007^{+0.019}_{-0.007}$
31.9	7.	(T)	0.889 ± 0.005	0.907	0.936	$0.917 \pm 0.005^{+0.025}_{-0.007}$
4.2	15.	(T)	0.760 ± 0.007	0.792	0.800	$0.767 \pm 0.007^{+0.008}_{-0.023}$
7.5	15.	(T)	0.788 ± 0.006	0.791	0.813	$0.811 \pm 0.006^{+0.008}_{-0.027}$
13.0	15.	(T)	0.818 ± 0.006	0.829	0.855	$0.843 \pm 0.006^{+0.011}_{-0.014}$
20.6	15.	(T)	0.849 ± 0.007	0.864	0.890	$0.875 \pm 0.007^{+0.013}_{-0.010}$
31.9	15.	(T)	0.878 ± 0.007	0.896	0.923	$0.905 \pm 0.007^{+0.014}_{-0.013}$
4.2	7.	(O)	0.202 ± 0.007	0.203	0.200	$0.199 \pm 0.007^{+0.009}_{-0.010}$
7.5	7.	(O)	0.152 ± 0.006	0.166	0.152	$0.139 \pm 0.005^{+0.010}_{-0.010}$
13.0	7.	(O)	0.124 ± 0.005	0.124	0.106	$0.106 \pm 0.004^{+0.022}_{-0.009}$
20.6	7.	(O)	0.100 ± 0.006	0.092	0.077	$0.084 \pm 0.005^{+0.018}_{-0.019}$
31.9	7.	(O)	0.090 ± 0.005	0.076	0.056	$0.066 \pm 0.003^{+0.042}_{-0.024}$
4.2	15.	(O)	0.210 ± 0.010	0.198	0.196	$0.208 \pm 0.010^{+0.012}_{-0.016}$
7.5	15.	(O)	0.158 ± 0.007	0.172	0.163	$0.150 \pm 0.007^{+0.009}_{-0.018}$
13.0	15.	(O)	0.129 ± 0.006	0.130	0.120	$0.118 \pm 0.006^{+0.018}_{-0.022}$
20.6	15.	(O)	0.092 ± 0.006	0.098	0.089	$0.084 \pm 0.005^{+0.018}_{-0.024}$
31.9	15.	(O)	0.089 ± 0.007	0.080	0.065	$0.072 \pm 0.006^{+0.035}_{-0.030}$
4.2	7.	(θ_{JET})	0.818 ± 0.025	0.803	0.561	$0.576 \pm 0.025^{+0.221}_{-0.337}$
7.5	7.	(θ_{JET})	0.612 ± 0.025	0.536	0.312	$0.388 \pm 0.025^{+0.136}_{-0.176}$
13.0	7.	(θ_{JET})	0.379 ± 0.018	0.305	0.167	$0.241 \pm 0.018^{+0.126}_{-0.094}$
20.6	7.	(θ_{JET})	0.266 ± 0.022	0.189	0.102	$0.179 \pm 0.022^{+0.035}_{-0.034}$
31.9	7.	(θ_{JET})	0.152 ± 0.010	0.136	0.071	$0.087 \pm 0.010^{+0.019}_{-0.052}$
4.2	15.	(θ_{JET})	0.941 ± 0.035	0.870	0.715	$0.786 \pm 0.035^{+0.092}_{-0.473}$
7.5	15.	(θ_{JET})	0.691 ± 0.033	0.672	0.421	$0.440 \pm 0.033^{+0.216}_{-0.263}$
13.0	15.	(θ_{JET})	0.529 ± 0.027	0.434	0.235	$0.330 \pm 0.027^{+0.168}_{-0.155}$
20.6	15.	(θ_{JET})	0.348 ± 0.027	0.298	0.155	$0.210 \pm 0.027^{+0.130}_{-0.108}$
31.9	15.	(θ_{JET})	0.288 ± 0.030	0.266	0.086	$0.108 \pm 0.030^{+0.168}_{-0.065}$

Table 9.2: The results of event shape analysis for thrust, oblateness, and jet angle. Systematic errors are included on the corrected values. Units: M_X in GeV , Q^2 in GeV^2 , and θ_{JET} in radians.

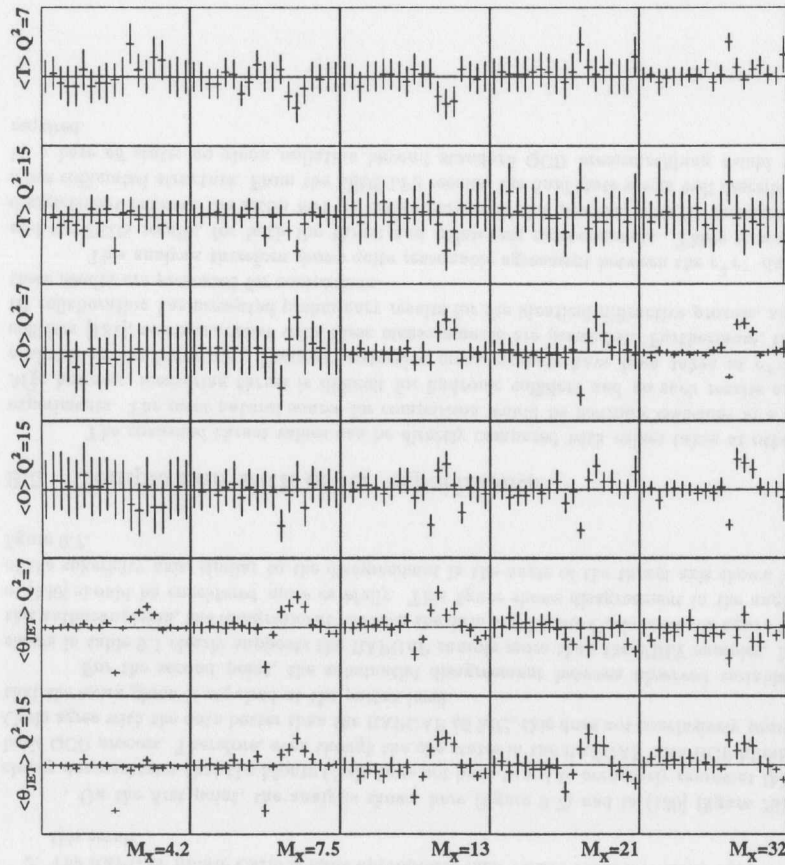


Figure 9.8: Results of systematic checks on corrected event shape variables. The first point in each histogram shows the nominal results; the remaining points are the systematic checks listed on page 133.

9.4 Discussion of ZEUS rapidity-gap results

A separate analysis [129] concluded that the events became planar with increasing M_X . However, such a conclusion seems to be at odds with the results in this thesis, since oblateness, a measure of planarity of the event, clearly is decreasing as M_X increases. This disagreement is discussed in this section.

When comparing the two results, one crucial difference should be considered. Since [129] requires the hadronic final state to have $\eta_{\max} < 1.8$, which clearly selects only a subset of the diffractive sample. The corrections are then made only by comparing with generated events with the same maximum rapidity. This method of correcting the data limits the systematic uncertainty caused by the unknown distribution of event shapes in events which were not selected with the rapidity gap requirement, and is quite sensible. However, these results cannot be directly compared to measurements taken without this rapidity gap requirement.

However, a comparison can be made using [130] (figure 76). Here, the data were corrected using RAPGAP, but including all η_{\max} values in the generated state. Substantial correction factors are required, but the results for sphericity, thrust, and $\langle p_T^2 \rangle$ clearly agree with the values from e^+e^- data. As shown in figure 9.9, the data also seem to follow the LPS results closely, compared with considerable disagreement observed with the rapidity gap requirement at the generator level.

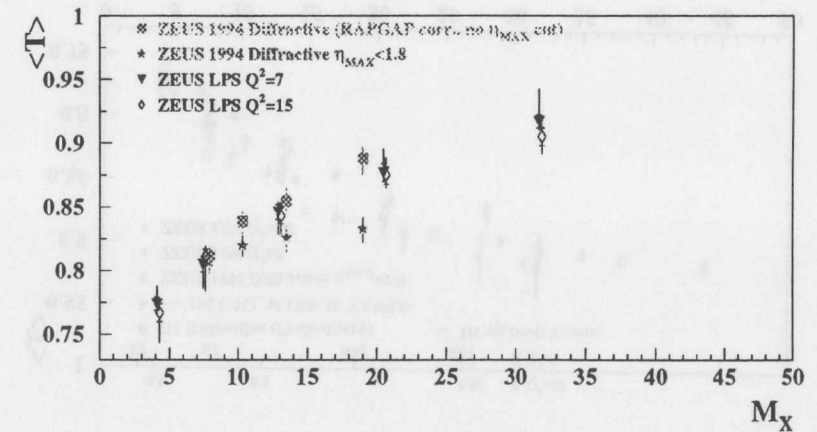


Figure 9.9: Corrected thrust distributions compared to measurements of the same process at ZEUS [129], with corrections either to the all events or only events with $\eta_{\max} < 1.8$.

Thus, the disagreement between e^+e^- and rapidity-gap results would be an incorrect conclusion if two conditions were true:

1. The RAPGAP Monte Carlo has not been tuned to the point where a $q\bar{q}$ state at mass s agrees with e^+e^- data for the event shape variables; this would seem apparent from

figure 9.7.

- The RAPGAP Monte Carlo is more appropriate than VBLY. Table 9.1 clearly supports this result.

On the first point, the analysis shown here (figure 9.7) and in [130] (figure 76), clearly demonstrates that the Monte Carlo have not been tuned to accurately represent this basic QCD process. Therefore, even though the $q\bar{q}g$ states in the RAPGAP with BGF Monte Carlo agree with the data better than the RAPGAP $q\bar{q}$ MC, this does not conclusively prove that the extra gluon is required at the parton level.

For the second point, the substantial disagreement between observed variables shown in table 9.1 clearly supports the RAPGAP sample more than the VBLY samples. In this authors opinion, the disagreement between the data and Monte Carlo shown in figure 43 of [130] should be considered more carefully. This figure shows disagreement in the angle of the sphericity axis, similar to the disagreement in the angle of the thrust axis shown in figure 9.7.

9.5 Comparison with other experiments

The corrected thrust values can be directly compared with values taken at other experiments. The most natural source for comparison would be hadronic collisions at $s = M_X^2$; however, measuring thrust is difficult for hadronic colliders and no such results are available in the literature. However, extensive measurements have been taken at e^+e^- colliders [131], so comparisons with these measurements are presented. Furthermore, the III collaboration has presented preliminary results for the identical diffractive process, and these results are presented for comparison.

This analysis therefore shows quite reasonable agreement between the e^+e^- data and the ZEUS results, for both the thrust and oblateness measurements. There is some disagreement between the ZEUS and III measurements of this process, with H1 measuring a less collimated structure. From the ZEUS LPS results, the final state seems well described by a bare $q\bar{q}$ state; no gluon radiation beyond standard QCD bremsstrahlung would be required.

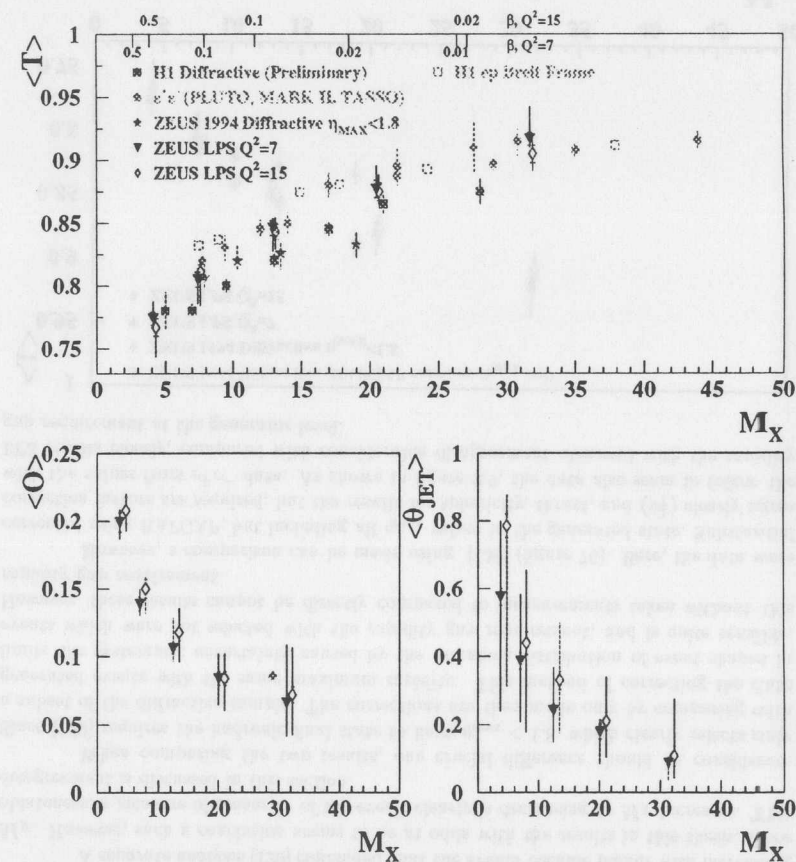


Figure 9.10: Corrected thrust distributions compared to measurements of the same process at H1 and from e^+e^- colliders [131].

Chapter 10

Conclusions

The ZEUS experiment has been able to collect a pure sample of diffractive events thanks to the presence of the Leading Proton Spectrometer (LPS). Careful simulation of the ZEUS experiment and the LPS indicate that the hardware performance is well understood, and physics variables can be reconstructed with sufficient accuracy.

Both 1994 and 1995 LPS data have been analyzed to obtain a diffractive DIS sample. The cross section, written in terms of the diffractive structure function $F_2^{D(4)}$, has been obtained from these data. This structure function appears factorizable; no correlations have been observed between t , x_p or β . The relatively large errors cannot rule out factorizable models [56]. A compact parameterization has been presented:

$$F_2^{D(4)}(\beta, Q^2, x_p, t) = N \exp(bt) \left(\frac{x_p}{0.001} \right)^{-a} \left[\beta(1-\beta) + \frac{c}{2}(1-\beta)^2 \right] \quad (10.1)$$

The systematic errors on the parameters include possible contributions due to LPS acceptance, beam halo backgrounds, reconstruction effects, and non-Pomeron exchange:

$$N = 539 \pm 45 \pm 190, \quad b = 6.6 \pm 0.6^{+1.2}_{-0.6}, \\ n = 0.052 \pm 0.004^{+0.013}_{-0.005}, \quad a = 1.08 \pm 0.06^{+0.08}_{-0.19} \quad (10.2)$$

In figure 10.1, this result is compared with the results from other experiments when measuring the same process. Clearly, a significant difference exists between the LPS results and those obtained without directly observing the final proton. This difference cannot be explained as contributions from Reggeon exchange. One possible culprit to this difference is in the background from fragmentation of nondiffractive events.

Final states in diffractive events bear a striking resemblance to those produced in e^+e^- collisions, although the results are in disagreement with Monte Carlo simulations which attempt to model the fragmentation of a $q\bar{q}$ final state. These results preclude substantial hard gluon radiation beyond that allowed in e^+e^- fragmentation from gluon bremsstrahlung. No correlation could be observed between the event shape variable thrust and other physics variables.

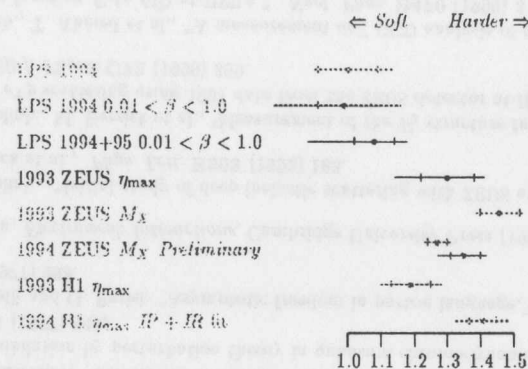


Figure 10.1: Exponent a of x_p dependence x_p^a measured from diffractive structure function with various analysis methods [121, 53, 51, 52, 54, 123].

Bibliography

- [1] H. Geiger and E. Marsden, "On a diffuse reflection of the α -particles," *Proc. R. Soc. London* **82** (1909) 495.
- [2] E. Rutherford, "The scattering of α and β particles by matter and the structure of the atom," *Philos. Mag.* **21** (1911) 669.
- [3] R. Hofstadter and R.W. McAllister, "Electron scattering from the proton," *Phys. Rev.* **98** (1955) 217.
- [4] M. Gell-Mann, "A schematic model of baryons and mesons," *Phys. Lett.* **8** (1964) 214.
- [5] J.J. Sakurai, "Theory of strong interactions," *Ann. Phys.* **11** (1960) 1.
- [6] R.P. Feynman, "Very high-energy collisions of hadrons," *Phys. Rev. Lett.* **23** (1969) 1415.
- [7] R.D. Field and R.P. Feynman, "A parameterization of the properties of quark jets," *Nucl. Phys.* **B136** (1978) 76.
- [8] A. Seiden, T.L. Shalk, and J.F. Martin, "Particle production in a quark-cascade model," *Phys. Rev.* **D18** (1978) 3990.
A. Seiden, "A simple model for the quark fragmentation functions seen in deep inelastic processes," *Phys. Lett.* **B68** (1977) 157.
- [9] K.G. Wilson, "Confinement of quarks," *Phys. Rev.* **D10** (1974) 2445.
- [10] R.M. Barnett, et al., "Review of Particle Physics," *Phys. Rev.* **D54** (1996) 1.
- [11] C. Geich-Gimbel, "Particle production at collider energies," *Int. Journal of Mod. Phys.* **A4**, 7 (1989) 1527.
- [12] R. Szwed, G. Wrochna and A.K. Wróblewski, "Genesis of the lognormal multiplicity distribution in the e^+e^- collisions and other stochastic processes," *Mod. Phys. Lett.* **A5** (1990) 1851.
- [13] Z. Koba, H.B. Nielsen and P. Olesen, "Scaling of multiplicity distributions in high energy hadron collisions," *Nucl. Phys.* **B40** (1972) 317.
- [14] R. Hagedorn, "Multiplicities, p_T distributions and the expected hadron \rightarrow quark-gluon phase transition," *Riv. Nuovo Cim.* **6**, 10 (1983) 1.
- [15] J.I. Friedman, H.W. Kendall, R.E. Taylor, "Nobel Lectures in Physics 1990," *Rev. Mod. Phys.* **63** (1991) 573.
- [16] CDF Collab., F. Abe, et al., "Observation of top quark production in $\bar{p}p$ collisions," *Phys. Rev. Lett.* **74** (1995) 2626;
D0 Collab., S. Abachi et al., "Observation of the top quark," *Phys. Rev. Lett.* **74** (1995) 2632.
- [17] V.N. Gribov and L.N. Lipatov, " e^+e^- pair annihilation and deep inelastic ep scattering in perturbation theory," *Sov. J. Nucl. Phys.* **15** (1972) 438,675;
L.N. Lipatov, "The parton model and perturbation theory," *Sov. J. Nucl. Phys.* **20** (1975) 95;
Yu.L. Dokshitzer, "Calculation of structure functions of deep-inelastic scattering and e^+e^- annihilation by perturbation theory in quantum chromodynamics," *Sov. Phys. JETP* **46** (1977) 641;
G. Altarelli and G. Parisi, "Asymptotic freedom in parton language," *Nucl. Phys.* **B126** (1977) 298.
- [18] P. Renton, *Electroweak Interactions*, Cambridge University Press (1990).
- [19] ZEUS Collab., "Initial study of deep inelastic scattering with ZEUS at HERA," M. Derrick et al., *Phys. Lett.* **B303** (1993) 183.
- [20] ZEUS Collab., M. Derrick et al., "Measurement of the F_2 structure function in deep inelastic e^+p scattering using 1994 data from the ZEUS detector at HERA," *Zeitschrift f. Physik* **C72** (1996) 399.
- [21] H1 Collab., T. Ahmed et al., "A measurement and QCD analysis of the proton structure function $F_2(x, Q^2)$ at HERA," *Nucl. Phys.* **B470** (1996) 3.
- [22] M. Glück, E. Reya and A. Vogt, "Parton structure of the photon beyond the leading order," *Phys. Rev.* **D45** (1992) 3986.
- [23] A.D. Martin, W.J. Stirling and R.G. Roberts, "Parton distributions: a study of the new HERA data, α_S , the gluon and p anti- p jet production," *Phys. Lett.* **B387** (1996) 419.
A.D. Martin, W.J. Stirling and R.G. Roberts, "Parton distributions updated," *Phys. Lett.* **B306** (1993) 145; Erratum-ibid. **B309** (1993) 492.
- [24] H.L. Lai, et al., "Global QCD analysis and the CTEQ parton distributions," *Phys. Rev.* **D51** (1995) 4763.
- [25] T. Regge, "Introduction to complex orbital momenta," *Nuovo Cim.* **14** (1959) 951.
- [26] P.D.B. Collins, A.D. Martin, *Hadron Interactions*, A. Hilger Ltd, Bristol (1984);
- [27] D.H. Perkins, *Introduction to High Energy Physics*, Addison-Wesley (1982).
- [28] K. Goulianos, "Diffractive interactions of hadrons at high energies," *Phys. Rep.* **101** (1983) 169, and *Nucl. Phys. B (Proc. Suppl.)* **12** (1990) 110.

- [29] A. Donnachie and P.V. Landshoff, "Elastic scattering and diffraction dissociation," *Nucl. Phys.* **B244** (1981) 322;
A. Donnachie and P.V. Landshoff, "Hard diffraction: Production of high p_T jets, W or Z , and Drell-Yan pairs," *Phys. Lett.* **B191** (1987) 309;
A. Donnachie and P.V. Landshoff, "Hard diffraction: production of high p_T jets, W or Z , and Drell-Yan pairs," *Nucl. Phys.* **B303** (1988) 634;
A. Donnachie and P.V. Landshoff, "Total Cross Sections," *Phys. Lett.* **B296** (1992) 227.
- [30] I.Y. Pomeranchuk, *Sov. Phys. JETP* **7** (1958) 499.
- [31] WA76 Collab., T. Armstrong et al., "Evidence for new states produced in the central region in the reaction $pp \rightarrow p_f(\pi^+\pi^-\pi^+\pi^-)p_s$ at 300 GeV/c," *Phys. Lett.* **B228** (1989) 536.
WA102 Collab., D. Barberis, et al., "A study of the centrally produced $\pi^+\pi^-\pi^+\pi^-$ channel in pp interactions at 450 GeV/c," hep-ex/9707021, submitted to *Phys. Lett.*
- [32] ZEUS Collab., M. Derrick et al., "Measurement of Total and Partial Photon Proton Cross Sections at 180 GeV Center of Mass Energy," *Zeitschrift f. Physik* **C63** (1994) 391.
- [33] III Collab., T. Ahmed et al., "Measurement of the total photon proton cross section and its decomposition at 200 GeV center-of-mass energy," DESY 95-162, *Zeitschrift f. Physik* **C69** (1995) 27.
- [34] Landolt-Börnstein, *Total Cross-Sections for Reactions of High Energy Particles*, New Series, Vol. 12b, H. Schopper, Ed. (1987).
- [35] H. Abramowicz, E.M. Levin, A. Levy and U. Maor, "Parametrization of parton distributions in the photon," *Phys. Lett.* **B269** (1991) 465.
- [36] SWT Collab., Y. Eisenberg et al., "Structure in the $\omega\pi\pi$ system at the a_2 mass region," *Phys. Rev.* **D5** (1972) 15;
J. Park et al., "The reaction $\gamma p \rightarrow \rho^0 p$ at 5.5 GeV to 18 GeV," *Nucl. Phys.* **B36** (1972) 404;
SBT Collab., J. Ballam et al., "Bubble chamber study of photoproduction by 2.8 GeV and 4.7 GeV polarized photons. 1. Cross-section determinations and production of ρ^0 and δ^{++} in the reaction $\gamma p \rightarrow p\pi^+\pi^-$," *Phys. Rev.* **D5** (1972) 545;
SBT Collab., J. Ballam et al., "Vector meson production by polarized photons at 2.8 GeV, 4.7 GeV, and 9.3 GeV," *Phys. Rev.* **D7** (1973) 3150;
W. Struczinski et al., "Study of photoproduction on hydrogen in a streamer chamber with tagged photons for $1.6 \text{ GeV} < E_\gamma < 6.3 \text{ GeV}$: topological and reaction cross-sections," *Nucl. Phys.* **B108** (1976) 45;
OMEGA Collab., D. Aston et al., *Nucl. Phys.* **B209** (1982) 56.
- [37] ZEUS Collab., M. Derrick et al., "Measurement of Elastic ρ^0 Photoproduction at IHERA," *Zeitschrift f. Physik* **C69** (1995) 39.
- [38] III Collab., S. Aid et al., "Elastic Photoproduction of ρ^0 mesons at IHERA," DESY 95-251 *Nucl. Phys.* **B463** (1996) 3.

- [39] G.A. Schuler and T. Sjöstrand, "The hadronic properties of the photon in γp interactions," *Phys. Lett.* **B300** (1993) 169;
G.A. Schuler and T. Sjöstrand, "Towards a complete description of high-energy photoproduction," *Nucl. Phys.* **B407** (1993) 539.
- [40] CDF Collab., F. Abe et al., "Measurement of small-angle antiproton-proton elastic scattering at $\sqrt{s} = 546$ and 1800 GeV," *Phys. Rev.* **D50**, 9 (1994) 5518.
- [41] E710 Collab., N.A. Amos et al., "A luminosity independent measurement of the $\bar{p}p$ total cross-section at $\sqrt{s} = 1.8 \text{ TeV}$," *Phys. Lett.* **B243** (1990) 158;
E710 Collab., N.A. Amos et al., "Diffraction dissociation in $\bar{p}p$ collisions at $\sqrt{s} = 1.8 \text{ TeV}$," *Phys. Lett.* **B301** (1993) 313.
- [42] CDF Collab., F. Abe et al., "Measurement of $\bar{p}p$ single diffraction dissociation at $\sqrt{s} = 546$ and 1800 GeV," *Phys. Rev.* **D50**, 9 (1994) 5535.
- [43] UA4 Collab., D. Bernard et al., "The cross section of diffraction dissociation at the CERN SPS Collider," *Phys. Lett.* **B186** (1987) 227.
- [44] UA4 Collab., D. Bernard et al., "Pseudorapidity distribution of charged particles in diffraction dissociation events at the CERN SPS collider," *Phys. Lett.* **B166** (1986) 459;
- [45] EHS/NA22 Collab., M. Begalli et al., "Multiplicity structure of inclusive diffraction in π^+p and k^+p interactions at 250 GeV/c," *Zeitschrift f. Physik* **C55** (1992) 531.
- [46] UA5 Collab., R.E. Ansorge et al., "Diffraction dissociation at the CERN pulsed $p\bar{p}$ collider at c.m. energies of 900 and 200 GeV," *Zeitschrift f. Physik* **C33** (1986) 175.
- [47] UA8 Collab., R. Bonino et al., "Evidence for transverse jets in high mass diffraction," *Phys. Lett.* **B211** (1988) 239;
UA8 Collab., A. Brandt et al., "Evidence for a superhard Pomeron structure," *Phys. Lett.* **B297** (1992) 417.
- [48] A.H. Müller, "O(2,1) analysis of single particle spectra at high energy," *Phys. Rev.* **D2** (1970) 2963; *ibid.* **D4** (1971) 150;
- [49] ZEUS Collab., M. Derrick et al., "Observation of Events with a Large Rapidity Gap in Deep Inelastic Scattering at IHERA," DESY 93-093, *Phys. Lett.* **B315** (1993) 481.
- [50] III Collab., T. Ahmed et al., "Deep inelastic scattering events with a large rapidity gap at IHERA," DESY 94-133, *Nucl. Phys.* **B429** (1994) 477.
- [51] ZEUS Collab., M. Derrick et al., "Measurement of the Diffractive Cross Section in Deep Inelastic Scattering," DESY 96-018, *Zeitschrift f. Physik* **C70** (1996) 391-412.
- [52] ZEUS Collab., "Measurements of the diffractive structure function at IHERA," *Int. Europhys. Conf. on High Energy Physics*, Jerusalem, 19-26 August 1997, N-638.
- [53] ZEUS Collab., M. Derrick et al., "Measurement of the Diffractive Structure Function in Deep Inelastic Scattering at IHERA," DESY 95-093, *Zeitschrift f. Physik* **C68** (1996) 569.

- [54] III Collab., T. Ahmed et al., "First measurement of the deep-inelastic structure of proton diffraction," DESY 95-036, *Phys. Lett. B* **348** (1995) 681.
- [55] L.N. Lipatov, "Reggeization of the vector meson and the vacuum singularity in nonabelian gauge theories," *Sov. J. Nucl. Phys.* **23** (1976) 338;
Y.Y. Balitsky and L.N. Lipatov, "The Pomernchuk singularity in Quantum Chromodynamics," *Sov. J. Nucl. Phys.* **28** (1978) 822;
E.A. Kuraev, L.N. Lipatov and V.S. Fadin, "The Pomernchuk singularity in nonabelian gauge theories," *Sov. Phys. JETP* **45** (1977) 199.
- [56] N.N. Nikolaev and B.G. Zakharov, "Pomeron structure function and diffraction dissociation of virtual photons in perturbative QCD," *Zeitschrift f. Physik C* **53** (1992) 331;
M. Genovese, N.N. Nikolaev and B.G. Zakharov, "Diffractive DIS from the generalized BFKL Pomeron. Predictions for IHERA," *JETP* **81** (1995) 625.
- [57] J.D. Bjorken, J. Kogut, "Correspondence arguments for high-energy collisions," *Phys. Rev. D* **8** (1973) 1341.
- [58] G. Ingelman and P. Schlein, "Jet structure in high-mass diffractive scattering," *Phys. Lett. B* **152** (1985) 256.
- [59] A. Capella, A. Kaidalov, C. Merino, D. Pertermann, J. Tran Thanh Van "Hard Diffraction at IHERA and the Gluonic Content of the Pomeron," *Phys. Rev. D* **53** (1996) 2309-2316
- [60] A. Capella et al., "Diffractive Dissociation in Deep Inelastic Scattering at IHERA," *Phys. Lett. B* **343** (1995) 403.
- [61] K. Goulianos, Rockefeller University preprint RU 95/E-06.
- [62] W. Buchmüller, "probing lumps of wee partons in deep inelastic scattering," *Phys. Lett. B* **335** (1994) 479.
W. Buchmüller and A. Hebecker, "A parton model for diffractive processes in deep inelastic scattering," *Phys. Lett. B* **355** (1995) 373.
- [63] H. Abramowicz, J. Bartels, L. Frankfurt, H. Jung, "Diffractive Hard Scattering Summary Report of the Working Group," *Future Physics at IHERA, Proc. of the Workshop 1995/96*, G. Ingelman, A. De Roeck, R. Klanner, eds, DESY (1996) 635.
- [64] M. Bishari, "Pion exchange and inclusive spectra," *Phys. Lett. B* **38** (1972) 510;
J. Pumplin, "Pion exchange in inclusive relations," *Phys. Rev. D* **8** (1973) 2249.
- [65] R.D. Field and G.C. Fox, "Triple Regge and finite mass sum rule analysis of the inclusive reaction $pp \rightarrow pX$," *Nucl. Phys. B* **80** (1974) 367.
- [66] K. Golec-Biernat, J. Kwieciński and A. Szczurek, "Reggeon and pion contributions in semi-exclusive diffractive processes at herA," *Phys. Rev. D* **56** (1997) 3955.
- [67] J.D. Sullivan, "One-pion exchange and deep-inelastic electron-nucleon scattering," *Phys. Rev. D* **5** (1972) 1732.

- [68] N.N. Nikolaev, W. Schäfer and B.G. Zakharov, "Diffractive DIS: back to triple Regge phenomenology?" preprint KFA-IKP(Th)-1996-06, hep-ph/9608338.
- [69] M. Glück, E. Reye and A. Vogt, "Parton distributions for high-energy collisions," *Zeitschrift f. Physik C* **53** (1992) 127.
- [70] G. Wolf, "IHERA: physics, machine and experiments," Lectures given at *Advanced Study Inst. on Techniques and Concepts of High Energy Physics*, St. Croix, Virgin Islands, Jun 19-30, 1986, DESY 86-089 (1986).
- [71] *The ZEUS Detector, Status Report*, DESY (1993).
- [72] ZEUS Collab., M. Derrick et al., "A measurement of $\sigma_{tot}(\gamma\text{-Proton})$ at $\sqrt{s} = 210$ GeV," *Phys. Lett. B* **293** (1992) 465.
- [73] K. Desler and U. Schneekoth, "The hardware of the Proton Remnant Tagger (PRT)," ZEUS Note 95-061 (1995).
- [74] S. Bhadra et al., "Test of a forward neutron calorimeter for the ZEUS experiment at IHERA," *Nucl. Instr. and Meth. A* **354** (1995) 479;
M.Brkić, "A study of leading neutrons in γp collisions at IHERA," Ph. D. thesis, University of Toronto, (1995), DESY F35D-95-10;
ZEUS Collab., M. Derrick et al., "Observation of events with an energetic forward neutron in deep inelastic scattering at IHERA," *Phys. Lett. B* **384** (1996) 388;
S. Bhadra et al., "The Design and test of a forward neutron calorimeter for the ZEUS Experiment" preprint hep-ex/9701015 (January 1997), to be published in *Nucl. Instr. and Meth.*
- [75] N. Harnew et al., *Nucl. Instr. and Meth. A* **279** (1989) 290;
C. B. Brooks et al., "Development of the ZEUS central tracking detector," *Nucl. Instr. and Meth. A* **283** (1989) 477;
B. Foster et al., "The performance of the ZEUS central tracking detector z-by-timing electronics in a transputer based data acquisition system," *Nucl. Phys. Proc. Suppl. B* **32** (1993) 181;
B. Foster et al., "The design and construction of the ZEUS central tracking detector," *Nucl. Instr. and Meth. A* **338** (1994) 254.
- [76] M. Derrick et al., "Design and construction of the ZEUS barrel calorimeter," *Nucl. Instr. and Meth. A* **309** (1991) 77;
A. Andresen et al., "Construction and beam test of the ZEUS forward and rear calorimeter," *Nucl. Instr. and Meth. A* **309** (1991) 101;
A. Bernstein et al., "Beam tests of the ZEUS barrel calorimeter," *Nucl. Instr. and Meth. A* **336** (1993) 23.
- [77] ZEUS Collab., M. Derrick et al., "Measurement of the proton structure function F_2 at low x and low Q^2 at IHERA," DESY 95-193, *Zeitschrift f. Physik C* **69** (1996) 607.
- [78] D. Kisieleska et al., DESY-IHERA report 85-25 (1985);
J. Andruszkow et al., "First measurement of IHERA luminosity by ZEUS lumi monitor," Ge DESY 92-066 (1992).

- [79] K. Piotrkowski, M. Zachara, "Determination of the ZEUS Luminosity in '93," ZEUS Note 94-167.
- [80] K. Piotrkowski, M. Zachara, "Determination of the ZEUS Luminosity in 1994," ZEUS Note 95-138.
- [81] S. Silverstein, et al., "The ZEUS calorimeter first level trigger," *Nucl. Instr. and Meth.* **A360** (1995) 322;
ZEUS TLT Group, D. Bandhopadhyay et al., "Online selection of physics events in the ZEUS third level trigger," DESY 93-091F, July 1993;
H. Boterenbrood, et al., "The ZEUS first and second level trigger," Presented at IEEE Nucl. Sci. Symp., Orlando, FL, Oct 26-31, 1992.
- [82] U. Behrens et al., "The eventbuilder of the ZEUS experiment," *Nucl. Instr. and Meth.* **A332** (1993) 253.
- [83] L.A.T. Bauerdick et al., "The physics analysis environment of the ZEUS experiment," DESY 95-236 (1995).
- [84] UA1 Collab., C. Albajar et al., "A study of the general characteristics of proton-antiproton collisions at $\sqrt{s} = 0.2$ to 0.9 TeV," *Nucl. Phys.* **B335** (1990) 261.
- [85] E. Barberis et al., "Design, testing, and performance of the frontend electronics for the LPS silicon microstrip detectors," *Nucl. Instr. and Meth.* **A364** (1995) 507-515; *erratum, ibid.*, **A386** (1997) 535.
- [86] T. Pulliam, "Noise studies on silicon microstrip detectors," Senior Thesis 1995, UC Santa Cruz, SCIPP 95-28 (unpublished).
- [87] D.E. Dorfan, "Bipolar frontend amplifier for use with silicon strip detectors," *Nucl. Instr. and Meth.* **A342** (1994) 143;
E. Barberis et al., "A low-power bipolar amplifier integrated circuit for the ZEUS silicon strip system," *Nucl. Phys. Proc. Suppl.* **B 32** (1993)
- [88] J. Rahn, et al., "Testing the Yield of an Amplifier-Discriminator Chip Fabricated in Tektronix SHPi," presented at *IEEE Nucl. Sci. Symposium*, San Francisco, CA, Nov. 2-6, 1993.
- [89] J. DeWitt, "The time slice system," *Nucl. Instr. and Meth.* **A288** (1990) 209;
"The digital time slice chip," Senior Thesis 1989, UC Santa Cruz, SCIPP 89-24.
- [90] K. O'Shaughnessy et al., "Testing and installation of ZEUS leading proton spectrometer detector planes," *Nucl. Instr. and Meth.* **A342** (1994) 260.
- [91] W. Press et al., *Numerical Recipes*, Cambridge University Press (1989).
- [92] A. Aimar, "ADAMO Welcome," <http://www1.cern.ch/Adamo>;
H. Kowalski et al., "Investigation of ADAMO performance in the ZEUS calorimeter reconstruction program," *Comput. Phys. Comm.* **57** (1989).

- [93] T. Massam et al., "The Leading Proton Spectrometer: High Precision Momentum Calibration," ZEUS Note 94-075, Jun 15, 1994.
- [94] ZEUS Collab., "The ZEUS Leading Proton Spectrometer and its use in the measurement of elastic photoproduction at IHERA," M. Derrick et al., *Zeitschrift f. Physik C73* (1997) 253.
- [95] R. Brun et al., "GEANT3," CERN DD/EE/84-1 (1987).
- [96] By J. del Peso, S. Nickel, E. Ros, "Fast Monte Carlo simulation of electromagnetic and hadronic showers in the ZEUS calorimeter," In *Amsterdam 1991, Proceedings, MC 91: Detector and event simulation in high energy physics* 361-374; *ibid.*, 342-360;
Y. Iga and St. Schlenstedt, "Status and Improvements of the ZEUS Calorimeter simulation," ZEUS-Note-97-019;
Y. Iga, "Simulation of the ZEUS calorimeter," DESY 95-005 (1995).
- [97] S. Maselli and A. Solano, "The LPS simulation in MOZART," ZEUS-Note-91-112.
- [98] S. Maselli and R. Sacchi, "LPS acceptance calculation and update of the LPS simulation," ZEUS-Note-92-43.
- [99] E. Barberis et al., "LPSWEIGHT.CAR: a reweighting routine for 1994 LPS data analysis" ZEUS Note 95-105 28/08/95
- [100] E. Barberis, "Measurement of the cross section and t distribution in diffractive deep inelastic scattering at IHERA," Ph. D. Thesis, University of California, Santa Cruz, 1996.
- [101] H. Jung, "Hard diffractive scattering in high energy ep collisions and the Monte Carlo generator RAPGAP," DESY 93-182.
- [102] K.H. Streng, "Hard QCD Scatterings in diffractive reactions at IHERA," in Proc. of the Workshop "Physics at IHERA", p. 365, ed. R.D. Peccei (Hamburg 1987).
- [103] K. Kwiatkowski, H. Spiesberger and H.-J. Möhring, "IHERACLES. An event generator for ep interactions at IHERA including radiative processes," Proceedings of the Workshop "Physics at IHERA", vol. 3, DESY (1992), 1294.
- [104] L. Lönnblad, "ARIADNE version 4: a program for simulation of QCD cascades implementing the color dipole model," *Comp. Phys. Comm.* **71** (1992) 15;
L. Lönnblad, "Rapidity gaps and other final state properties in the colour dipole model for deep inelastic scattering," *Zeitschrift f. Physik C65* (1995) 285.
- [105] T. Sjöstrand and M. Bengtsson, "The LUND Monte Carlo for jet fragmentation and e^+e^- physics — JETSET version 6.3 — an update," *Comp. Phys. Comm.* **43** (1987) 367.
- [106] B. Andersson, G. Gustafson, G. Ingelman and T. Sjöstrand, "Parton Fragmentation and String Dynamics," *Phys. Rep.* **97** (1983) 31.

- [107] T. Sjöstrand, "How to discriminate between high- p_T physics Monte Carlos," *Zeitschrift f. Physik C42* (1989) 301;
H-U.Bengtsson and T.Sjöstrand, "The Lund Monte Carlo for hadronic processes — PYTHIA version 4.8," *Comp. Phys. Commun.* **46** (1987) 43;
T.Sjöstrand, CERN-TH 6488/92 (1992).
- [108] P. Bruni et al., "Diffractively produced hadronic final states and the Pomeron structure," Proceedings of the Workshop "Physics at IIERA", vol. 1, DESY (1992), 363; A. Solano, Ph. D. Thesis (University of Torino), 1993.
- [109] G. Marchesini, et. al., "IIERWIG version 5.9," hep-ph/9607393 (July 1996).
- [110] ZEUS Collab., M. Derrick et al. "Exclusive ρ^0 Production in Deep Inelastic Electron-Proton Scattering at IIERA," DESY 95-133, *Phys. Lett.* **B356** (1995) 601-616
- [111] M. Kasprzak, "Inclusive properties of diffractive and nondiffractive photoproduction at IIERA," Ph. D. thesis, Warsaw University (1996), DESY F35D-96-16.
- [112] R. Sinkus and H. Abramowicz, "Electron identification with neural networks at ZEUS," ZEUS-Note 93-11, November 1993.
- [113] R. Sinkus and T. Voss, "Particle identification with neural networks using a rotational invariant moment representation," DESY 96-264, *Nucl. Instr. and Meth.* **A391** (1997) 360.
- [114] S. Bentvelsen, J. Engelen and P. Kooijman, "Reconstruction of (x, Q^2) and extraction of structure functions in neutral current scattering at IIERA, Proceedings of the Workshop "Physics at IIERA", vol. 1, DESY (1992), 23.
- [115] F. Jacquet and A. Blondel, Proceedings of "The study of an ep facility for Europe", DESY 79/48 (1979) 391.
- [116] U. Bassler and G. Bernardi, "On the kinematic reconstruction of deep inelastic scattering at IIERA: the Σ method," *Nucl. Instr. and Meth.* **A361** (1995) 197.
- [117] III Collab., C. Adloff et al., "Diffraction dissociation in photoproduction at IIERA," *Zeitschrift f. Physik C74* (1997) 221.
- [118] ZEUS Collab.; J. Breitweg et al., "Study of photon dissociation in diffractive photoproduction at IIERA," DESY 97-060 (March 1997) *Zeitschrift f. Physik C75* (1997) 215.
- [119] N. Cartiglia, for the ZEUS Collab., "ZEUS leading baryons at low x_L in DIS and photoproduction," presented at *DIS97*, Chicago (April 1997).
- [120] T. Gehrman, W.J. Stirling, "Deep Inelastic Electron-Pomeron Scattering at IIERA," *Zeitschrift f. Physik C70* (1996) 89-102.
- [121] ZEUS Collab.; J. Breitweg et al., "Measurement of the diffractive structure function $F_2^{D(4)}$ at IIERA," DESY 97-184 (September 1997) accepted by *Zeitschrift f. Physik*

- [122] UA1 Collab., G. Arnison, et al., "Charged particle multiplicity distributions in proton-antiproton collisions at 540 GeV centre of mass energy," *Phys. Lett.* **B123** (1983) 108.
- [123] J. Rahn, "A Monte Carlo test of the $\ln M_X$ background subtraction method in DIS, for one (M_X, Q^2) bin," ZEUS note.
- [124] A. Breakstone et al., "Charged multiplicity distributions in pp interactions at CERN ISR energies," *Phys. Rev.* **D30** (1984) 528.
- [125] III Collab., C. Adloff, et al., "Inclusive Measurement of Diffractive Deep-Inelastic ep Scattering," DESY 97-158, to be published in *Zeitschrift f. Physik*
- [126] Yu.L. Dokshitzer, V.A. Khoze, A.H. Mueller, S.I. Troyan, *Basics of perturbative QCD*, Frontieres (1991).
- [127] ZEUS Collab., M. Derrick et al., "Observation of Jet Production in Deep Inelastic Scattering with a Large Rapidity Gap at IIERA," DESY 94-063, *Phys. Lett.* **B332** (1994) 228.
- [128] J. Vermaseren, F. Barreiro, L. Labarga and F.J. Ynduráin, "Pomerons and jet events at IIERA," hep-ph/9611444, DESY 97-031, submitted to *Phys. Lett.*
- [129] ZEUS Collab., M. Derrick et al., "Event shape analysis of deep inelastic scattering events with a large rapidity gap at IIERA," in preparation.
- [130] J.M. Hernández, F. Barreiro and L. Labarga, "Event shape analysis of multihadronic final states in deep inelastic rapidity gap events," ZEUS Note (1997).
- [131] TASSO Collab., W. Braunschweig et al., "Global jet properties at 14-44 GeV center-of-mass energy in e^+e^- annihilation," *Zeitschrift f. Physik C47* (1990) 187;
MARK II Collab., A. Peterson et al., "Multihadronic events at $E_{c.m.} = 29$ GeV and predictions of QCD models from $E_{c.m.} = 29$ GeV to $E_{c.m.} = 93$ GeV," *Phys. Rev.* **D37** (1988) 1;
PLUTO Collab., Ch. Berger et al., "Energy dependence of jet measures in e^+e^- annihilation," *Zeitschrift f. Physik C12* (1982) 297.
- [132] LPS Group, "LPS Alignment, Calibration and Reconstruction for 1994 Data, and First Results on dN/dt in ρ^0 Photoproduction and Diffractive DIS." ZEUS 96-059, April 1996.
- [133] M. Grothe, "Measurement of the diffractive proton structure function $F_2^{D(3)}$ using the Leading-Proton-Spectrometer," draft ZEUS Note, March 10, 1997.
- [134] N. Cartiglia, "Diffraction at IIERA," talk given at the SLAC summer school 1996.
- [135] F.E. Close and J.R. Forshaw, "Are diffractive events at IIERA due to a gluemeron or a quarkball?" Rutherford Appleton Laboratory Note RAL-TR-95-046, hep-ph/9509247